NANOSCALE CELL MEMBRANE ORGANIZATION A NEAR-FIELD OPTICAL VIEW

Promotiecommissie:

prof. dr. Alfred Bliek	University of Twente
prof. dr. Niek van Hulst	University of Twente
prof. dr. Maria García-Parajó	University of Twente
prof. dr. Carl Figdor	Nijmegen Center for Molecular Life Sciences
dr. Gerhard Schütz	Johannes Kepler University Linz
dr. David Klenerman	Cambridge University
prof. dr. Vinod Subramaniam	University of Twente
prof. dr. Wiebe Kruijer	University of Twente
dr. Alessandra Cambi	Nijmegen Center for Molecular Life Sciences

The work described in this thesis has been financially supported by the 'Stichting voor Fundamenteel Onderzoek der Materie (FOM)', which is financially supported by the 'Nederlandse organisatie voor Wetenschappelijk Onderzoek (NWO)'.

The research was carried out in the group
Applied Optics, Faculty of Science & Technology
MESA$^+$ Institute for Nanotechnology
University of Twente
P.O. Box 217, 7500AE Enschede
the Netherlands.

Cover design: Veek Studio

ISBN: 90-365-2325-7
Printed by: Febodruk BV, Enschede, the Netherlands.

NANOSCALE CELL MEMBRANE ORGANIZATION A NEAR-FIELD OPTICAL VIEW

PROEFSCHRIFT

ter verkrijging van
de graad van doctor aan de Universiteit Twente,
op gezag van de rector magnificus,
prof. dr. W.H.M. Zijm,
volgens besluit van het College voor Promoties
in het openbaar te verdedigen
op vrijdag 21 april 2006 om 15.00 uur

door

Marjolein Koopman

geboren op 3 mei 1977
te Hoogeveen

Dit proefschrift is goedgekeurd door:
prof. dr. N.F. van Hulst (promotor)
prof. dr. C.G. Figdor (promotor)
prof. dr. M.F. García-Parajó (assistent promotor)

Contents

Chapter 1

Introduction

The cell plasma membrane of eukaryotic cells is a lipid bi-layer that separates the cell cytosol from the extracellular environment. The composition and organization of proteins and lipids within this bi-layer have a direct impact on many cellular processes, since they form the senses of the cell. Technological advances, like high resolution microscopy together with the possibility to address different membrane components via specific labeling now allows researchers to investigate cell membrane organization in detail.

1.1 The cell membrane: more mosaic than fluid

The plasma membrane defines the cell boundary and maintains different environments between cytosol and extracellular environment. An important step in the study of cell membranes was taken with the development by Singer and Nicholson in 1972 [1] of the 'fluid mosaic model'. This model describes the plasma membrane as a lipid bi-layer, forming a two dimensional liquid in which molecules are randomly distributed. However, the number of experiments that contradict the Singer-Nicholson model is rapidly extending. In fact, there is increasing evidence that the plasma membrane is far from homogeneous, but is rather a mosaic composed of different nano- and microdomains. The heterogeneity of the plasma membrane is evidenced by the spatial and temporal confinement of proteins and lipids in defined nanometric-scale areas of the membrane [2, 3]. Dynamic events like change in mobility or temporal association between lipids and proteins within these microdomains can have a direct impact on the biological function of these molecules and therefore on cellular processes like cell activation, antigen presentation and cell-cell interactions. The size of these membrane domains is estimated to range from a few nanometers to several hundreds of nanometers. These small dimensions make investigation with conventional microscopy difficult, if not impossible. Several microscopy techniques can be used to circumvent this problem and will be presented in Section 1.3. We now briefly describe the different domains that have been identified in the cell plasma membrane, as schematically represented in Figure 1.1. One should not be misled by this static picture since, in fact, large stable domains have not been found in living cells [4]. Several studies suggest that membrane microdomains are indeed small and highly dynamic, constantly changing in size and composition [5, 6].

One of the first structures found in the plasma membrane of eukaryotic cells were caveolae. These small ($\sim$ 60 nm) flask-shaped membrane invaginations consist mainly of the caveolin protein, which binds cholesterol. Caveolae have been implicated in a range of cellular functions, such as cholesterol transport, endocytosis and signal transduction [7].

A second class of domains is characterized by the presence of tetraspanins, a family of proteins with four transmembrane regions. These proteins can interact with each other, thereby forming membrane microdomains, often referred to as the 'tetraspanin web' [8]. Through the organization of cell surface receptors in active complexes these microdomains provide a scaffold for the transmission of external stimuli to intracellular-signaling components [9] and therefore mediate processes such as adhesion, migration, co-stimulation and signal transduction.

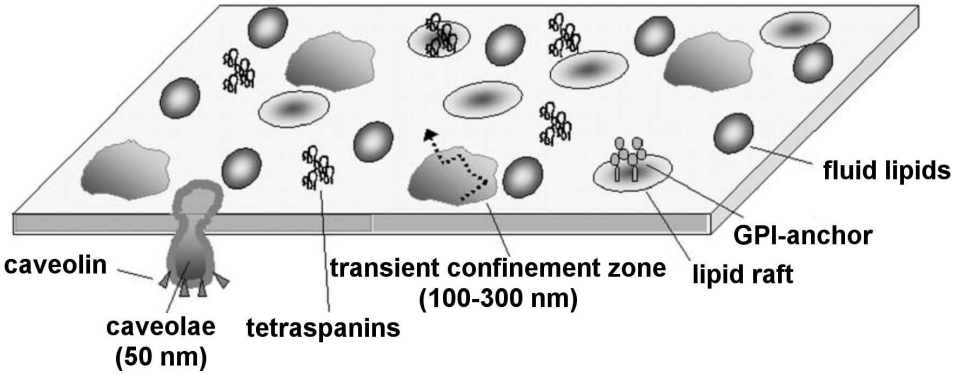

Figure 1.1: Schematic and static representation of the various types of microdomains present in the cell membrane.

The third type of organization discovered in membranes are so called transient confinement zones which are formed by a membrane-associated actin mesh network [10]. In fact, various transmembrane proteins that are anchored to the actin mesh underneath the cell membrane act as 'rows of pickets' that define the compartments [11]. The long-range control of diffusion appears to be carried out by the actin-based membrane skeleton and its associated transmembrane-protein pickets, through their partitioning (corralling) and tethering effects, which are enhanced upon molecular complex formation by diffusing membrane molecules [12].

Lipid rafts are a fourth class of membrane inhomogeneities. They are enriched in cholesterol and lipids with saturated acyl chains, such as sphingolipids. Lipid raft sizes measured in vivo range from several tens of nanometers to almost a micrometer [2, 3, 13–15]. In the next section we will discuss lipid rafts in further detail.

1.2 Lipid rafts

The cell plasma membrane is composed of a lipid mixture. The main components include phospholipids, glycerolipids, sphingolipids and cholesterol. Together with membrane-bound proteins, which can occupy up to 70 % of the membrane surface, the cell membrane is an enormously complex entity. Each cell type has its own specific lipid composition (that is, percentage ratio of each particular lipid) [16]. Lipid compositions can also change as a cell grows and develops.

Evidence for the occurrence of lipid rafts within cell membranes started from

the observation of formation of liquid ordered phases (l_o) and fluid phases (l_d) in model membranes caused by the action of cholesterol on phospholipids [17]. In fact, cholesterol orders the acyl chains of the disordered phase and hence reduces permeability [18], favoring the formation of a l_o phase [19]. The formation of this ordered phase is especially promoted by those lipids that contain linear saturated acyl chains, which can pack more easily with cholesterol. Spingholipids, present in high amounts in the cell plasma membrane, are prevalently saturated and in fact they have been shown to favor l_o phases, also thanks to their ability to form intermolecular hydrogen bonds [20, 21]. Numerous experiments demonstrating the coexistence of l_o and l_d phases have been performed on model membranes [22] and the notion that similar phase separations might occur in the cell plasma membrane has provided the basis for the 'raft hypothesis' [23].

Currently lipid rafts are defined as membrane microdomains enriched in glycosphingolipids and cholesterol that act as platforms where specific membrane proteins can segregate. Lipid rafts have been shown to be involved in signal transduction [24], endo- [25, 26] or exo-cytosis [27], and membrane trafficking [28]. The lipid raft field however, is full of controversies [29], caused by the different methods and operational definitions to describe lipid rafts. Most raft functions were derived from experiments using one of the following, nowadays controversial, techniques [29, 30]. The first operational criterion to define raft-association relies on resistance of lipid rafts to solubilization by detergents, like Triton X-100, at 4^o C, and association to so called detergent-resistant membranes (DRMs) [23, 31, 32]. DRMs can be separated from the rest of the cell lysate by ultracentrifugation on a sucrose gradient. However, recent biochemical studies have shown that DRMs extracted by different detergents can vary in their specificity for raft markers [33]. Another method is based on the enriched presence of cholesterol in lipid rafts. It relies on the use of specific molecules that are able to disrupt lipid rafts integrity by extracting cholesterol from the membrane with methyl-β-cyclodextrin. Effects on cell function are directly related to lipid rafts, however it should be noted that this drug may affect more cell functions than just lipid raft disruption [34]. A third well established procedure to assess the localization of a given protein with lipid rafts is antibody induced co-patching of the protein with the raft associated glycosphingolipid GM1 [35]. Essentially co-patching relies on the formation of aggregates of membrane components, using secondary antibodies [36], that can be labeled and are large enough to be visible with fluorescence microscopy. However, lipid rafts might be induced or stabilized by cross-linking [35].

Novel microscopy techniques have recently been applied, hoping to elucidate the size, content and dynamics of plasma membrane microdomains and lipid rafts in particular in living cells. Nevertheless, the results still remain inconclu-

sive [37]. The most recent example of the controversies surrounding the raft field is a study by Douglass and Vale that challenges the current lipid raft hypothesis and the role of lipid rafts in T-cell signaling [38]. The authors have used total internal reflection fluorescence (TIRF) microscopy to track the movement of single fluorescently tagged signaling molecules at the plasma membrane [38]. They conclusively showed that the biochemical property of detergent insolubility does not predict whether proteins reside within microdomains at the cell surface, but rather protein-protein interactions are responsible for the regulation of plasma-membrane microdomains. Their results are compatible with a model in which lipid rafts are either extremely small and highly dynamic or constitute a significant proportion of the plasma membrane. Results from other workers [5, 6] also support this model. At present, probably the best approach towards understanding membrane microdomains is to compare and contrast results obtained with different experimental methods. In the next section we will briefly describe some novel microscopy techniques that have been used to study membrane microdomains and lipid rafts in particular.

1.3 Probing cell membrane organization

Microdomain composition, size, and lifetime are still unanswered questions. However, currently no single technique can be expected to solve these questions simultaneously, especially since high resolution (to probe small domains) and fast image acquisition (to probe fast dynamics) are not yet available in one instrument. The variety of methods used so far have been excellently reviewed by Lagerholm et al. [39] and here the most relevant findings are only briefly described.

The dynamic nature of membrane domains can be investigated via the translational mobility of fluorescent molecules in the cell membrane using fluorescence recovery after photobleaching (FRAP) [5] or more locally via fluorescence correlation spectroscopy (FCS) [40]. In general these studies revealed that association with lipid rafts is not the dominant factor governing lateral mobility, indicated by the absence of correlation between diffusion speed and characterization as either raft or non-raft marker. In single particle tracking (SPT) mobility has been investigated by tracking the movement of labels specifically bound to membrane components [41]. As a result of SPT experiments, membrane compartmentalization has been widely recognized through the observation of transient confinement zones (TCZs), regions in the membrane where a protein or lipid is confined much longer than would be expected by simple Brownian motion [2]. TCZs as described in literature are typically 100-300 nm in size and have lifetimes of hundreds of milliseconds to seconds, depending on the experimental sampling rate [10, 12].

Aside from the dynamic nature of membrane domains, revealing the true size and composition requires high resolution microscopy techniques, since most putative components are abundantly present in the cell membrane. In principle fluorescence resonance energy transfer (FRET) is capable to detect proximities below the optical resolution (∼wavelength/2), since FRET efficiency depends directly on donor-acceptor distances, typically 1-10 nm [42]. The basis for data interpretation is that clustering stabilizes inter particle distances. FRET efficiencies that are independent of the fluorophore density have been interpreted as indicative for the existence of clusters [43, 44]. However the results obtained using FRET are often difficult to interpret, since FRET efficiency depends also on donor-acceptor properties like relative orientation, rotational mobility and spectroscopic properties. In addition FRET experiments provide no information on distances beyond 10 nm.

The increased spatial resolution of electron microscopy (0.1-10 nm) has been used to directly visualize raft size and composition. Antibody gold-particles of different sizes can be targeted to membrane components revealing their surface distribution. The most intriguing observation has been the absence of co-clustering between two putative raft markers (a GPI-anchored protein and GM1 lipids) [45] together with microdomains up to 500 nm in diameter. Unfortunately, since electron microscopy requires extensive sample preparation it can not be extended towards live cell imaging.

1.3.1 High resolution fluorescence imaging

In this thesis we focus on high resolution fluorescence microscopy, since it is compatible with the imaging of living cells, provides excellent spectral contrast and in combination with sensitive detectors allows for the detection of individual molecules. To overcome the diffraction limit of light and providing the high resolution necessary to investigate membrane organization we use high resolution near-field scanning optical microscopy (NSOM). So far this is the only technique that combines surface sensitivity, single molecule detection and nanometric (∼ 80-100 nm) optical resolution together with simultaneous topographic information [46]. Therefore NSOM is an ideal technique to study the organization of the plasma membrane in detail [47–49], while taking full advantage of all available fluorescence labeling methods.

NSOM is based on scanning a small sub-wavelength aperture in close proximity to the sample surface. The probe illuminates the sample with a field that is strongly localized at the vicinity of the aperture and decreases very rapidly away from the probe's end face [50]. In Figure 1.2 the differences between con-

focal fluorescence microscopy and NSOM are schematically illustrated. While the lateral resolution is diffraction limited for confocal microscopy ($\sim$ 300 nm) in NSOM the lateral resolution is determined by the probe size ($\sim$80-100 nm). In combination with the superior axial resolution of NSOM, resulting from the exponentially decaying character of the illumination field, the excitation volume is small (1000 times smaller than for confocal microscopy) thus reducing the cytoplasm background fluorescence. This enables single molecule detection on the cell membrane with a high signal-to-background ratio and therefore allows quantitative fluorescence analysis.

The most critical part in NSOM operation is the reliable and reproducible control of the probe-sample distance especially when imaging soft cells in liquid. Several approaches to image soft biological samples in liquid have been reported based on either optical shear force detection [51], home-built piezo feedback mechanisms [52] or tuning fork feedback [53–55]. In all these cases, immersion in liquid results in a decreased sensitivity of the feedback mechanism due to the liquid viscosity and drag. In this thesis we present a diving bell concept in which the tuning fork is vibrating in air, while the tip is immersed in liquid. NSOM now allows imaging of cells in liquid with a resolution better than 100 nm, thereby bridging the gap between FRET and confocal microscopy.

1.3.2 Markers for labeling membrane components

A common feature in fluorescence microscopy is the need for specific markers to label the membrane components of interest. In the context of lipid rafts, two types of markers are commonly used. On the one hand there are a number of lipids and proteins that partition into lipid rafts, the so called raft markers. On the other hand, there are also lipids and proteins that are excluded from a lipid raft environment and are referred to as non-raft markers. In this thesis we investigated two different raft markers and two non-raft markers. In Table 1.1 these markers are introduced, together with references to the methods that have been used to characterize their organization within the cell membrane. Glycosylphosphatidylinositol-(GPI)-anchored proteins and GM1 lipids are widely used as lipid raft markers, while the transferrin receptor (CD71) as well as membrane co-factor protein (CD46) are often excluded from lipid rafts. To visualize the markers, proteins can be labeled via specific fluorescent antibodies, requiring sample fixation to prevent unwanted signaling or protein aggregation. The lipid GM1 can be directly labeled via the non-toxic β-subunit of the cholera toxin (CTxB). We note that although this probe is pentavalent, currently there are no suitable alternatives, since direct lipid labeling has been shown to influence probe

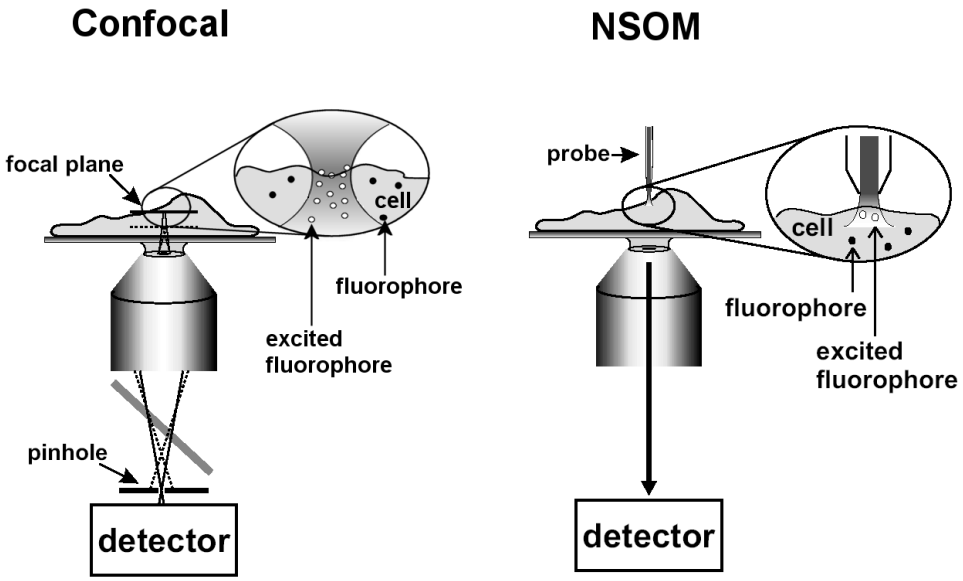

Figure 1.2: Schematic comparison between confocal and near-field scanning optical microscopy. Confocal microscopy (left image): excitation light is collimated, reflected by a dichroic mirror and focused on to the sample (path not shown). Fluorescence is collected by the same objective, filtered and detected. The pinhole prevents detection of fluorescence from outside the focal volume. Near field scanning optical microscopy (right image): the probe illuminates the sample in the near field, while the sample is scanned underneath the probe. Fluorescence is collected in the far field by a high-NA objective, filtered and sent to the detector.

partitioning [56]. For instance, Bodipy-GM1 has been shown to be excluded from lipid rafts in model membranes [57].

Marker	Description	References
CD55	GPI (lipid anchored protein), raft marker	[5, 6, 58–61]
GM1	glycosphingomyelin, raft marker	[10, 45, 62, 63]
CD71	transferrin receptor, non-raft marker	[63, 64]
CD46	membrane co-factor protein, non-raft marker	[59]

Table 1.1: Raft and non-raft markers used to probe partitioning in this thesis.

1.4 Cells in the immune system

In this thesis we have focussed on the organization of lipids and proteins in the membrane of cells in the immune system. This sophisticated defense system works through the finely orchestrated interactions among different cell types, which belong either to the innate or to the adaptive immune system. Important cells in the innate immune system are: macrophages, natural killer cells, granulocytes and monocytes all of which interact with pathogens locally and in a non-specific manner. The adaptive immune system is uses T and B lymphocytes that specifically recognize a certain pathogenic antigen. After an initial contact an immunological memory is build up, which will provide a faster and enhanced reaction upon encounter with such a 'known' antigen.

Dendritic cells (DCs) form the interface between the innate and adaptive immune system. DCs are specialized for the uptake, processing, transport and presentation of antigens to T cells [65]. At a stage called immature, DCs reside in the peripheral tissues. Upon activation by tissue damage or microbial products, DCs start migrating to the lymph node. Upon migration, DCs become mature, process the captured antigen and present the antigen derived peptides on their surface via the major histocompatibility complex (MHC). Meanwhile, DCs up-regulate the co-stimulatory molecules required for effective interaction with T cells.

Monocytes are large phagocytic cells that derive from bone marrow precursors. Monocytes remain in the blood for a short time and then exit the blood stream to enter body tissues. Interestingly, monocytes can differentiate into dendritic cells. This process, together with the different function of immature and mature DCs indicates that the plasma membrane of monocytes and DCs display a specific set of cell surface molecules. Their organization and presence must change dynamically to allow specific alterations occurring in the development from monocyte to immature DC and subsequently to mature DC. We focussed to investigate the organization of membrane proteins and lipids on both immature DC as well as cell line closely resembling monocytes, the so called THP1 cells.

1.4.1 DC-SIGN and LFA-1

In this thesis we describe our investigation of the nanometer scale spatial organization DC-SIGN on immature dendritic cells (DCs) and LFA-1 on THP1 cells. The biological role of these proteins is briefly introduced in this section.

DC-SIGN is a C-type lectin specifically expressed by DCs (not expressed by monocytes) and has a dual function both as adhesion and pathogen receptor. As an adhesion receptor, DC-SIGN supports initial DC-T-cell interaction by binding

to ICAM-3 [66], and mediates tethering and rolling of DC on the endothelium by interacting with ICAM-2 [67]. It has been recently shown that the surface organization of DC-SIGN is directly related to its function as pathogen receptor. A clustered distribution is essential to enhance the interaction as well as the internalization efficiency of DC-SIGN/pathogen complexes [59].

Integrins are transmembrane α/β heterodimers that regulate cell-cell and cell extracellular matrix interactions. The lymphocyte function associated antigen-1 (LFA-1) is a leukocyte specific integrin that mediates leukocyte migration across the endothelium both during normal lymphocyte recirculation and in response to inflammatory signals, migration within tissues, and formation of immunological synapse [68–72]. Integrins are expressed both in monocytes and in DCs. It has been proposed that the activity of this integrin can be regulated via two mechanisms. One is a conformational change which results in an increased affinity [73]. The second mechanism to regulate activation is a dynamic reorganization of LFA-1 receptors into clusters at the cell membrane that locally increases the binding valency and strengthens the interaction with the ligand (avidity regulation) [74]. However, most of the experimental evidence, so far, for the formation of LFA-1 clusters on activated cells has been rather qualitative and based on micron sized patches on the plasma membrane of polarized cells [75]. Recently it has been demonstrated that LFA-1 mediated binding to ICAM-1 is completely lost during development of monocyte derived immature DCs. The lack of binding coincides with the exclusion of LFA-1 molecules from microdomains [76].

It is evident that spatial organization of both DC-SIGN and LFA-1 can have a direct impact on cell function. It is therefore of crucial importance to get further insight in the organization of both DC-SIGN and LFA-1 using high resolution microscopy and imaging on cells in liquid conditions.

1.5 Thesis overview

This thesis is the result of extensive high resolution NSOM imaging in order to investigate and quantify the organization of proteins and lipids in the plasma membrane of two cells of the immune system: Immature dendritic cells (imDCs) and THP1 cells, a cell line closely related to human monocytes. During my PhD research, I developed a unique diving bell concept that allowed the first reproducible operation of NSOM under liquid conditions. This enabled the direct visualization and quantification of lipid rafts and protein domains, which together with quantitative co-localization experiments reveals exciting information on protein-lipid associations.

First we describe (**Chapter 2**) how the performance of NSOM can be ex-

tended to measurements in liquid environments using a diving bell concept. As a proof-of-principle individual fluorescent molecules on the membrane of cells in solution are imaged with a spatial resolution of 100 nm. Then we apply NSOM to directly visualize and quantify lipid rafts, enriched in glycosphyngomyelin (GM1), via fluorescently labeled cholera toxin (CTxB) in imDC and THP1 cells under liquid conditions (**Chapter 3**). As a result of the high GM1 content in THP1 membranes we anticipate to observe a significant contribution of random clustering. This effect is mainly due to the still finite imaging resolution of NSOM in combination with the high packing density of GM1. The degree of true clustering is then assessed by comparing the experimentally obtained fluorescence images to simulated images of randomly distributed particles at densities related to experimental conditions (**Chapter 4**). Furthermore we demonstrate in **Chapter 5** that classification of a protein as lipid raft associated does not predict its surface arrangement, i.e. lipid raft partitioning does not automatically imply clustering and clustering is not necessarily maintained by lipid rafts. We also map the organization of the C-type lectin DC-SIGN on imDC and the integrin LFA-1 on THP1 cells both in liquid, revealing clustering of these proteins at the nanometer scale. To simultaneously investigate the possible association of lipids and proteins we perform dual color experiments using NSOM in liquid (**Chapter 6**). The extent of co-localization between lipid rafts and proteins is quantified using Pearson's correlation coefficient and results are compared to confocal co-patching experiments. Finally **Chapter 7** contains an outlook on further NSOM research and the implications of the research presented in this thesis on the current understanding of membrane microdomains .

Chapter 2

Near-field scanning optical microscopy in liquid conditions

Clustering of cell surface receptors into micro-domains in the plasma membrane is an important mechanism for regulating cellular functions. Unfortunately, these domains are often too small to be resolved with conventional optical microscopy. Near-field scanning optical microscopy (NSOM) is a relatively new technique that combines ultra high optical resolution, down to 70 nm, with single molecule detection sensitivity. As such, the technique holds great potential for direct visualization of domains at the cell surface. Yet, NSOM operation under liquid condition is far from trivial. In this chapter we show that the performance of NSOM can be extended to measurements in liquid environments. We present a reliable and easy-to-use system, with a perfect analogy to a diving bell, to perform tuning fork based near field scanning optical microscopy on soft cells in liquid. The principle of the diving bell system is to allow vibration of the tuning fork in air, while the NSOM probe is immersed in solution. In this way Q factors of 200 and higher in liquid are routinely obtained. The force feedback is reliable and stable over hours requiring minimum adjustment of the set-point during imaging. With this system, tip-sample interaction forces are kept below 350 pN enabling imaging of soft cells in buffer solution. For the first time, individual fluorescent molecules on the membrane of cells in solution are imaged with a spatial resolution of 100 nm. As such, liquid-NSOM is capable to reveal cell membrane organization in detail, while working in conditions that allow live cell imaging.

2.1 Introduction

The organization of proteins into micro- or nanodomains in the cell membrane plays an important role in cellular function [15]. Resolving the exact size, structure and composition of these domains is important in order to understand their specific function. The combination of a high spatial resolution technique to resolve individual domains, together with single molecule detection sensitivity to determine the composition of each individual domain is therefore highly desirable. Immuno gold labeling in combination with transmission electron microscopy has the potential to offer both high resolution and insight into domain composition [45, 59, 77, 78], however only very thin parts of a dried sample can be imaged. Furthermore, dehydrating cells results in compaction of the cell membrane, increasing the possibility to artificially induce protein aggregation, a clearly unwanted artifact when studying membrane domain organization.

To date, fluorescence microscopy remains as the most widely used technique for live cell imaging. Membrane components can be directly visualized via specific antibodies or direct fusion with a Green Fluorescent Protein (GFP) family member [79]. Similarly, already single molecule detection on cell membranes has been demonstrated using confocal, widefield epifluorescence and total internal reflection microscopy [80]. In particular, the last two techniques have allowed the monitoring of protein dynamics revealing differences in the lateral diffusion of membrane proteins and strongly supporting the hypothesis of compartmentalization within the cell membrane [81]. Unfortunately, these techniques are diffraction limited, with a resolution > 300 nm for the visible regime, excluding direct visualization of domains smaller than this value. Furthermore, the concentration of fluorescent molecules has to be reduced artificially in order to observe individuals.

There are two possible routes to break the diffraction limit. One way concerns the use of point spread function engineering [82], where stimulated emission depletion microscopy has already shown single molecule detection sensitivity [83]. This technique has been demonstrated on cells [84], although measurements on cells at the single molecule level and over the full visible spectrum are still awaiting. The second approach is near field scanning optical microscopy (NSOM), where a subwavelength aperture probe is scanned in close proximity to the sample. So far this is the only technique that combines surface sensitivity, single molecule detection, nanometric ($\sim$ 80-100 nm) optical resolution together with simultaneous topographic information [46]. Therefore NSOM is an ideal technique to study the organization of the plasma membrane in detail [47], while taking full advantage of all available fluorescence labeling methods, including the use of GFPs.

The most relevant cell membrane studies using NSOM include localization

of host and malarial proteins on fixed mouse fibroblasts [85], the imaging of membrane lipids and proteins on fibroblast [86], the distribution of major histocompatibility complexes I and II [87], visualization of individual GFP fused to integrins on fibroblasts [48], visualization of nuclear pore complexes in nuclear envelopes [88] and a study on ion channel clusters in cardiac myocyte membranes [89, 90]. More recently, single molecule studies on complete cells using NSOM have been performed [91]. However, most of these studies were performed on fixed and critical point dried samples mainly because of the difficulties in reliably regulating the distance between tip and the soft cell surface while operating in physiological buffers. Although important biological information can be extracted from NSOM on dry biological samples, these results are always subject to potential drying artifacts [92].

As mentioned above, the critical part in NSOM operation is the reliable and reproducible control of the probe-sample distance. The use of shear force detection based on tuning fork feedback has proven to be an easy, cheap, sensitive and reliable method [93]. However, despite the wide application for operation in air, the imaging of soft biological samples in liquid such as living cells, has witnessed a low success rate.

Live cell imaging requires the scanning system to be kept in force feedback with small interaction forces under liquid conditions. Several approaches to image soft biological samples in liquid have been reported either based on optical shear force detection [51], home-built piezo feedback mechanisms [52] or tuning fork feedback [53–55]. In all these cases, immersion in liquid results in a decrease in sensitivity of the feedback mechanism due to the liquid viscosity and drag. Recently, our group demonstrated a recovery of the Q-factor up to 60 (higher Q provides more sensitivity) after full immersion of the tuning fork prongs, which allowed stable imaging on hard samples [53]. However in this case the tip sample interaction force still exceeded 4 nN a force too large to perform cell imaging. Moreover the tuning fork has to be coated to prevent electrical short-cut in buffer solution. Lee et al. [54] reported Q-factors of 400 by immersing only the fiber tip, but in this case the liquid level is extremely critical, demanding an elaborate and impractical sample holder design.

In this chapter we present a concept in which the tuning fork is encapsulated and thus vibrating in air, in perfect analogy to a diving bell. Thus, while the tip is in liquid and in contact with the sample the tuning fork force sensor is working in air. We apply this system to image the topography of dendritic cells immersed in buffer solution and compare the results to tapping mode atomic force microscopy (AFM) at similar conditions. Furthermore, we incorporated the diving bell in an existing NSOM setup and here we show for the first time detection of individual

fluorescent molecules on a cell membrane in solution and with nanometric spatial resolution.

2.2 Materials and Methods

2.2.1 The tuning fork diving bell

The basic model for tuning fork dynamics has been introduced by Karrai and Grober [93]. If the tip-sample distance is regulated to achieve a constant preset phase shift between the drive and the oscillator, the interaction force is given by [94]

$$F_{interaction} = \frac{kx_{res}}{Q}\Delta\varphi, \tag{2.1}$$

where $\Delta\varphi$ is the phase shift caused by force interaction, k the spring constant of the tuning fork, x_{res} the tip amplitude at resonance and Q the quality factor of the system. Clearly, the higher the Q, the lower the interaction force between tip and sample. Using a 32 kHz tuning fork in air we routinely operate at $Q = 700$ and x_{res}=0.1 nm. The exact value of the Q factor is determined by the amount of glue used to attach the tip to the tuning fork prong. Q can vary between 50 (too much glue) and 2000 (very little glue) and in practice we selected tips with a Q factor of 700 in air. The tuning fork in combination with our phase feedback circuit has a bandwidth of 300 Hz [95]. The minimal phase set-point we can achieve with our electronics corresponds to the detection of 0.017 radians phase shift, which together with a spring constant of 40 kNm^{-1} results in estimated maximum interaction forces of 100 pN. We work with large area scanners (range in z of 26 μm), therefore the main contribution to the vertical vibration noise in our measurements is the electronic noise in the z-scanner which corresponds to a height difference of 6.4 nm.

The diving bell consists of a small glass tube, carefully glued in to an aluminum holder as shown in Figure 2.1. Through the airtight sealing of the aluminum holder the glass tube will act as a diving bell for the tuning fork, maintaining the air-liquid interface at a fixed level, at the bottom of the glass tube and independent of the amount of liquid used. The aluminum holder with the glass tube encapsulates the 32 kHz tuning fork, which is attached via a magnet to a dither piezo to excite it mechanically at its resonance frequency. We have chosen 32 kHz tuning forks instead of the 100 kHz reported in our previous work [53] because of their larger physical dimensions which enable easier handling. A pulled glass fiber (diameter 125 μm) is attached to one of the prongs of the tuning fork

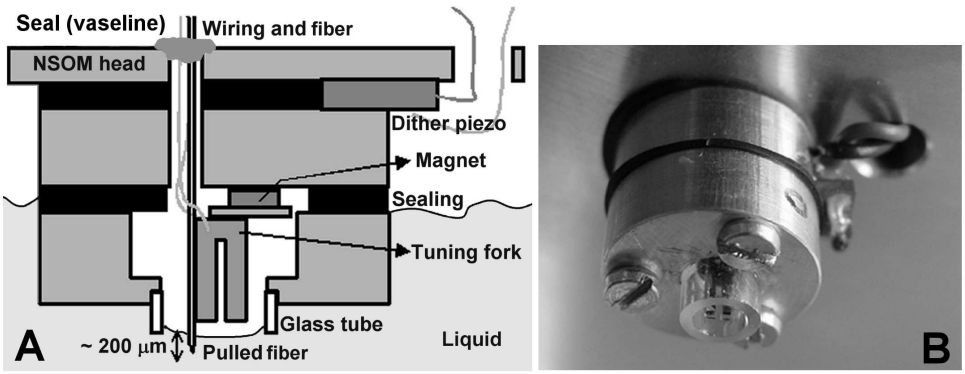

Figure 2.1: The tuning fork diving bell. The schematic diagram of the design of the tuning fork diving bell is shown in (**A**). On top of the NSOM head a vaseline seal is used to provide the necessary airtight sealing. A photograph of the real diving bell is shown in (**B**). The diameter of the small glass tube is ~ 5 mm.

using an epoxy resin (Araldite) while leaving the tip end protruding ~ 500 μm from the prongs end. In this way the free end of the fiber can still be considered stiff with respect to the tuning fork. We checked the oscillation mode of the tuning fork and found that the two prongs move towards and away from each other as expected at resonance [53]. The tuning fork, together with the glass tube holder is connected to the NSOM head, which is used to position the tip in close proximity to the sample scanning stage. The wiring of the tuning fork and the NSOM fiber are fed through a tiny hole in the head. The hole is sealed on top using vaseline. By inserting small silicone discs between the different diving bell components we ensure an airtight sealing of the system. The length of the glass tube is chosen such that a fiber length of ~ 200 μm is sticking outside the aperture plane of the glass tube. Because of the airtight sealing, once this system is immersed into the liquid, the surface of the liquid remains in the plane of the aperture. Lambelet and coworkers have proposed a similar scheme to control the immersion depth of a fiber tip in an optical shear force feedback system [51]. Essentially, there are no restrictions on the amount of solution to be used. Furthermore, buffer exchange is easily possible even with the tip in close proximity to the sample. Using the diving bell concept it is possible to image in any liquid without further adaptations to the scanning system or the tuning fork while maintaining a high Q factor.

2.2.2 Experimental set-up of the liquid-NSOM

The core of a NSOM is the fiber probe which is raster scanned over the sample surface. The obtainable lateral optical resolution is determined by the size of the aluminum coated aperture (typically $\sim$ 80-100 nm) used to excite the sample. To obtain this resolution the probe is kept in close proximity ($<$ 10 nm) to the sample surface using a piezo-electric force sensing element (tuning fork), oscillated at 32 kHz [93]. Height feedback is performed by keeping the phase difference between the driving excitation and the tuning fork signal constant [95, 96]. In this way optical and topographic maps of the surface are created simultaneously.

To operate the NSOM in liquid conditions we use the diving bell concept which ensures that the tuning fork is vibrating in air, while the tip is immersed in liquid. Our home built combined confocal/NSOM microscope equipped with the tuning fork diving bell is schematically shown in Figure 2.2. The proteins of interest are fluorescently labeled with Alexa-647 (see Sample preparation) and excited using the 647 nm line of an Argon/Krypton-ion laser (CW, Spectra-Physics). In confocal mode, circularly polarized excitation light is reflected by a dichroic mirror (650 DRLP Omega Optical) and focused onto the sample using an oil immersion objective (100x, 1.3 NA). In NSOM mode the sample is excited via the fiber probe (aperture $\sim$ 90 nm). The emitted fluorescence is collected and spectrally separated from the excitation light using a 665 nm long pass filter. A polarizing beam splitter is used to split the signal into two perpendicular polarization components. Both signals are sent to photon counting avalanche photodiodes (APDs). The fluorescence images generated in this way reflect the in-plane orientation of each single fluorescent molecule.

2.2.3 Sample preparation

Immature dendritic cells (imDCs) were cultured from healthy human blood monocytes in presence of interleukin-4 and GM-CSF (500 and 800 units/ml respectively) for six days to obtain imDCs [66]. The DCs were stretched on a poly-l-lysine coated coverslip for 1 hour at 37^{o}C, rinsed three times with phosphate buffered saline (PBS) and fixed with 1% paraformaldehyde in PBS for 15 minutes at room temperature. The specimens were washed three times in PBA (PBS, containing 0.5% bovine serum albumin and 0.01% sodium azide). The cells were then incubated with primary monoclonal antibodies against DC-SIGN in PBA (10 μg/ml) for 60 minutes at room temperature. After three washing steps with PBS, a second incubation was performed for 60 minutes at room temperature, with an Alexa647 labeled goat antimouse IgG antibody ($G\alpha$M-Alexa647) in PBA (10 μg/ml), allowing fluorescent detection of the anti-DC-SIGN antibody. La-

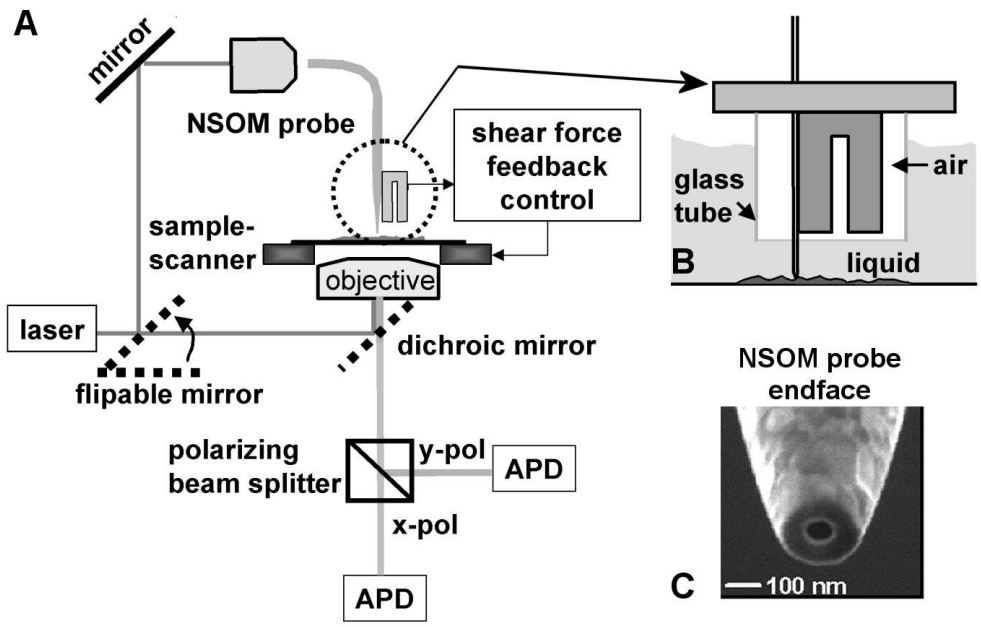

Figure 2.2: (**A**) Schematic diagram of the combined confocal/NSOM setup. The flipable mirror enables easy switching between the NSOM and confocal mode of operation. With the diving bell (**B**) only the tip is immersed in liquid, while the tuning fork sensor is vibrating in air. (**C**) Electron microscopy image of a typical NSOM probe used in our experiments.

beled samples were washed three times in PBS and post fixed in 1% paraformaldehyde. The wet samples were stored in PBS containing 1% paraformaldehyde. As a reference, critical point dried samples were also prepared, as described by Cambi et al. [59].

2.3 Results

2.3.1 Performance of the diving bell system

To verify the performance of the tuning fork diving bell we measured the frequency response of the system by driving the fork with the dither piezo and recording the piezoelectric response of the fork. In Figure 2.3 the response curve of a 32.768 kHz tuning fork both in air and phosphate buffered saline (PBS) is shown. In air the resonance frequency f_0 is shifted to 33.595 kHz due to the stiffening effect of the glass fiber on the tuning fork prong [53]. The Q factor

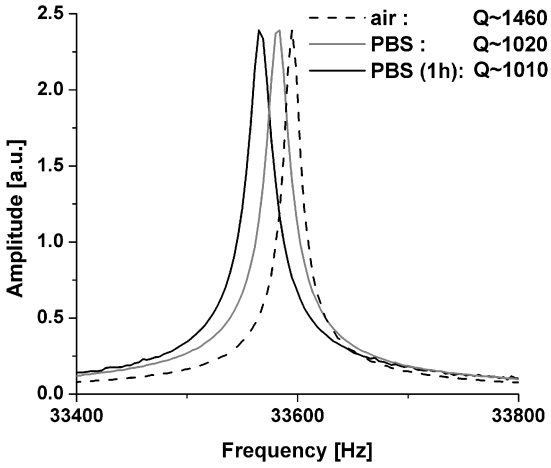

Figure 2.3: Frequency response of a 32.768 kHz tuning fork in PBS and in air. The tuning fork has a pulled glass fiber attached to one of its prongs. The first response curve in PBS is obtained directly after immersion of the diving bell while the second response curve is obtained after a time interval of 1 hour. As a reference, the response of the tuning fork vibrating in air is also included.

(calculated as f_0/FWHM) in air is 1460. Then the system is immersed in liquid using the diving bell and the frequency response is recorded, directly after immersion and after one hour. As can be seen from Figure 2.3 after immersion the resonance frequency has slightly shifted and the Q factor is reduced to 1020, which to our knowledge is the largest reported Q factor for a tuning fork feedback system in liquid without the use of electronic Q enhancement [97]. We also observed an extra damping in the recorded tip amplitude probably due to an effective reduction of the amplitude driving of the fork. Because part of the energy is dissipated into the liquid surrounding the glass tube, a similar driving amplitude as used in air will result in a less efficient excitation of the fork and smaller tip amplitude. This can be easily corrected by increasing the excitation amplitude. After one hour the resonance frequency has slightly shifted and the Q factor is still as high as 1010.

We verified the performance of several tip-tuning fork sets and in each case immersion of the system only resulted in a slight Q factor reduction as expected when only the tip of the fiber is being immersed. Using the tuning fork diving bell concept we routinely obtain Q factors of at least 200 resulting in a maximal tip-sample interaction force of 350 pN. We have noticed that although the reduction

of Q is small, the system is not yet fully stable and over a period of hours the resonance frequency shifts at a pace of $\sim$ 50 Hz/hour typically together with a small decrease in Q. This drift results in a very slow change in the phase difference which is an input for the feedback system. Therefore, it is easy to correct for these small shifts by carefully re-adjusting the phase set-point of the feedback during imaging.

To test whether the interaction forces are low enough to image soft biological material, a sample containing imDCs was prepared. In Figure 2.4 the topography at the edge of a dendritic cell is shown. The tip used had a Q of 210 and the image was done with a scanning speed of 8 μm/s. The edges of the cell are flat, elevated 200 nm above the glass substrate. The small dendrites are clearly visible on the right side of the image. The shear force image is comparable to an image obtained using tapping mode AFM in liquid with a silicon nitride cantilever with a spring constant of 0.10 N/m and a resonance frequency of 38 kHz at similar scanning speed. In both cases the interaction forces with the sample are similarly low, preserving the smooth membrane structure. Clearly, the interaction forces between the tip and sample are small preventing sample damage.

2.3.2 NSOM versus confocal microscopy on dried imDCs

To demonstrate the advantage of NSOM over confocal microscopy we first examined the distribution of DC-SIGN on the membrane of a critical point dried imDC in air. DC-SIGN is a C-type lectin exclusively expressed on DCs which plays important and distinct roles during the immune response [66, 98]. Typical images on the same cell area are shown in Figure 2.5. We select individual cells using a CCD camera and bright field illumination (Figure 2.5 **A**). The selected imDCs have been imaged in confocal mode with a scan size of 20 x 20 micrometers. A region of interest showing fluorescence contrast has been selected for further confocal (Figure 2.5 **B**) and near-field investigation (Figure 2.5 **D**). Simultaneously with the near-field optical information we obtain topographic information as shown in Figure 2.5 **C**.

The fluorescence intensity in the confocal image is high, due to both high expression levels and close packing of DC-SIGN on the membrane. The resolvable fluorescent 'spots' all have a similar diffraction-limited size of $\sim$ 300 nm. Comparing the NSOM fluorescence image of the same area, it is clear that the high resolution enables the identification of individual 'spots' in areas apparently fully packed upon confocal investigation. Furthermore, while the 'spots' resolved in the confocal image vary only in intensity, the NSOM optical image reveals 'spots'

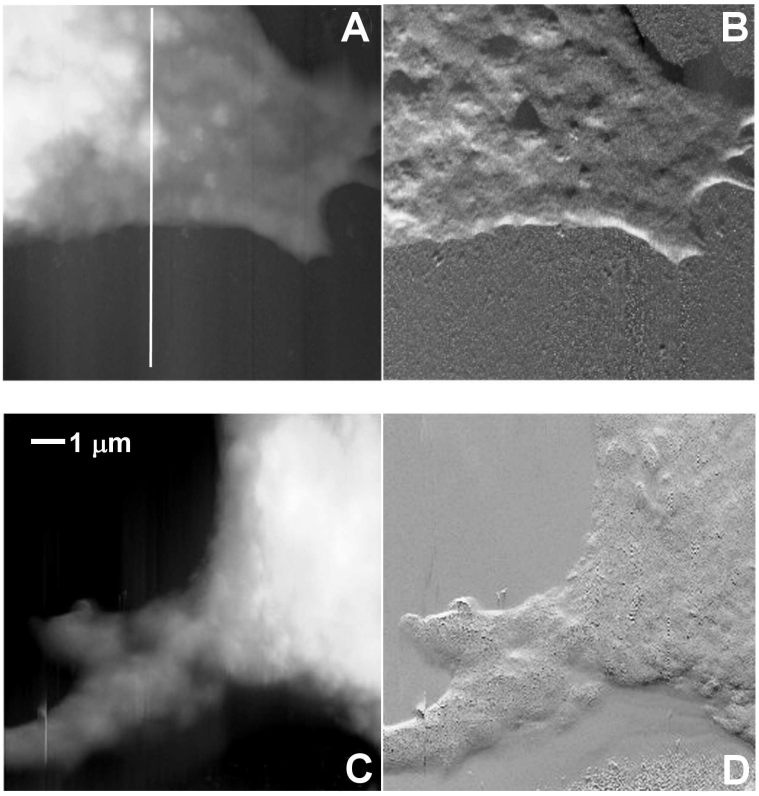

Figure 2.4: Comparison between AFM and NSOM topography images. (**A**) and (**B**) show, respectively, the topography and the feedback error signal image of an imDC in PBS obtained with tuning fork shear force feedback. The bottom images (**C**) and (**D**) show respectively the topography and the error signal image of the same cell type in water with tapping mode AFM.

differing both in size and intensity. This indicates that the number of DC-SIGN molecules per domain varies and that DC-SIGN domains occupy a membrane area that is well below the diffraction limit of confocal microscopy (smaller than $\sim$ 300 nm in diameter) but slightly larger than the NSOM tip with a diameter of 100 nm. This observation is consistent with the work of Cambi et al. [59] and a detailed study using NSOM in air [91], both working with critical point dried imDCs.

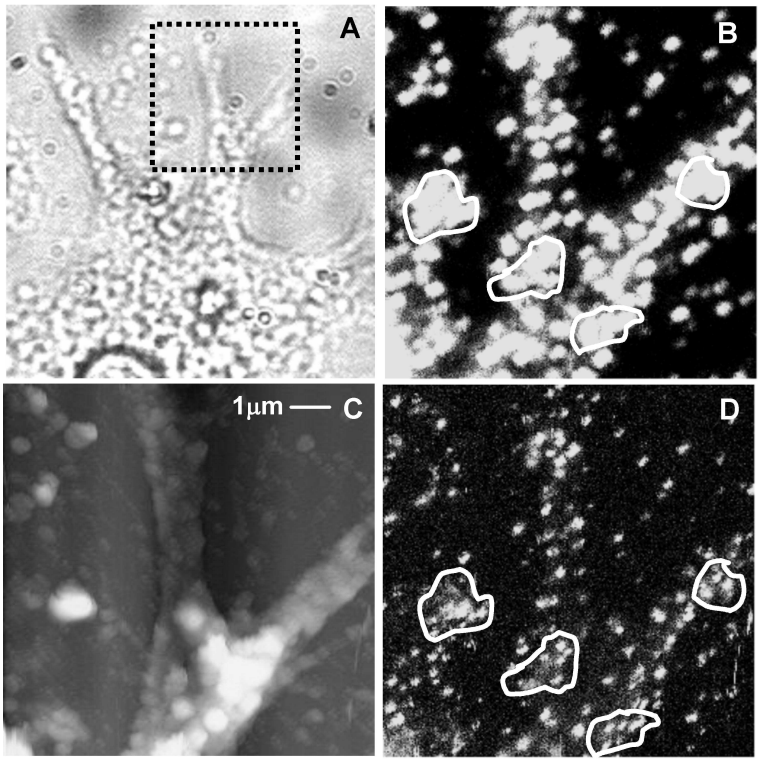

Figure 2.5: A selected area of the dendritic cell of interest, (**A**), is imaged in confocal mode, (**B**). The same area is imaged with NSOM resulting in a topographic image, (**C**), with a corresponding high resolution optical image, (**D**). In the high resolution image individual 'spots' can be resolved in the highlighted areas, whereas the same areas appear fully packed upon confocal investigation.

2.3.3 NSOM on imDCs in liquid

To investigate the organization of DC-SIGN on imDCs in solution we have used the NSOM equipped with the diving bell for liquid operation. Prior to imaging microscope slides containing the cells were washed with PBS, mounted in a liquid cell and covered with $\sim$ 1 ml of PBS solution. In Figure 2.6 **A** the resulting topography is shown. The line trace in Figure 2.6 **B** demonstrates that the feedback is reliable and stable, with the tip following the contours of the cell. Fine dendrites, with a height of $\sim$ 100 nm are apparent in the topographic image at the cell edges, while the central part of the cell, where the nucleus resides, can reach several microns in height. This is consistent with measurements using tapping mode

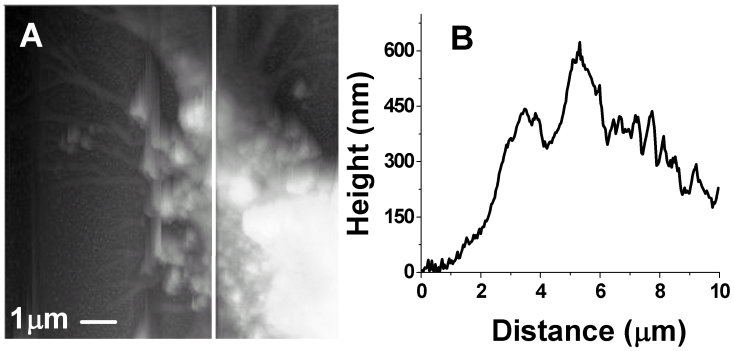

Figure 2.6: Topography image (**A**) of an imDC in PBS obtained with tuning fork shear force feedback. The white line in (**A**) indicates the position of the line trace in shown in(**B**).

atomic force microscopy on living DCs (A. Cambi, unpublished observations). The appearance of the small dendrites in the topography also demonstrates the gentle imaging capabilities of the technique. Throughout this thesis the topographic images were used to exclude artifacts in the fluorescence images due to the structure of the membrane, such as steep cell edges and membrane folding or ruffling.

After selecting a region of interest with confocal microscopy, a high resolution image of the same area is performed with NSOM. Figure 2.7 shows the fluorescence image in confocal (2.7 **A**) and NSOM (2.7 **B**) modes. The color in the optical images reflect the in-plane orientation of the emission dipole of the excited fluorophores. The color scale ranges from red to green, reflecting a 90 degree change in in-plane orientation. A yellow color corresponds to an equal amount of photons on both APDs reflecting either the presence of multiple emitters in the excited volume, or a single emitter with 45 degrees in-plane or an out of plane orientation.

Comparing the confocal image in Figure 2.7 **A** with the NSOM optical image in Figure 2.7 **B** the difference in lateral resolution is striking. In the confocal image the dendritic cell appears to be completely covered with proteins. Individual molecules are only visible outside the cell region, due to unspecific binding of labeled antibodies to the substrate. In contrast, using near-field excitation we can not only resolve individual 'spots' but also individual molecules on the cell surface. The presence of a well-defined polarized emission (color of most spots is green or red) is indicative for unique dipole emission and thus single molecule

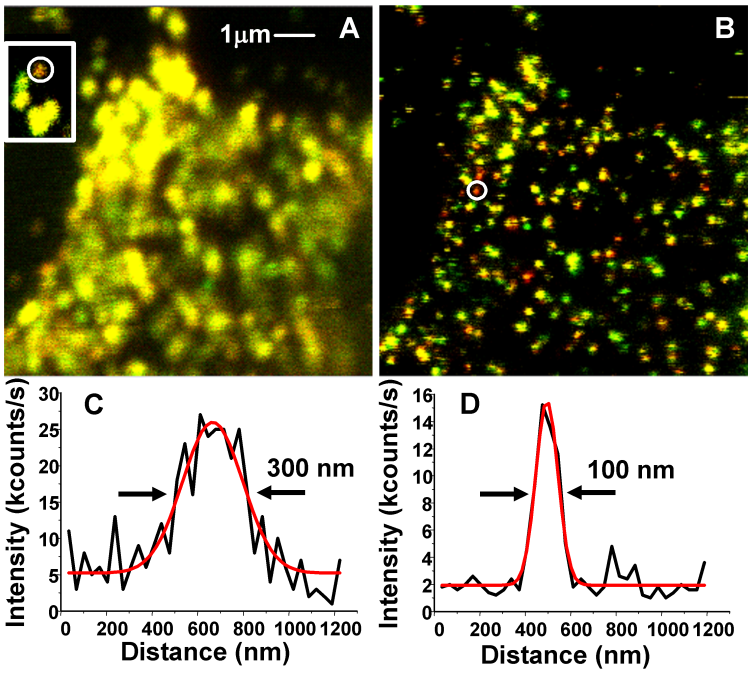

Figure 2.7: Fluorescence image of a dendritic cell in buffer solution collected in confocal (**A**) and NSOM (**B**) modes. The white circles indicate the position of the linetraces through single molecules (recognized by their unique dipole emission, red or green color) in (**C**) and (**D**). These linetraces demonstrate the superior resolution of NSOM (100 nm) in (**D**) as compared to the diffraction limited confocal resolution (300 nm) in (**C**). The intensity scale is locally changed in the confocal image (indicated by the white box in (**A**)) in order to visualize the individual molecule.

detection. It is also important to note that, due to the smaller excitation volume of NSOM the contribution of the fluorescence background from the cytosol is approximately ten times lower as compared with confocal illumination. Therefore we have more sensitivity with NSOM and are able to recognize individual molecules.

The line traces through individual molecules in Figure 2.7 **C** (on the glass substrate) and Figure 2.7 **D** (on the cell membrane) demonstrate the superior resolution of NSOM (100 nm) with respect to the diffraction limited resolution of confocal microscopy. In both cases the resolution is measured as the full width at half maximum of a Gaussian fit to the fluorescence profile. To our knowledge these images show for the first time single molecule detection on a cell membrane in solution with nanometric resolution.

2.4 Conclusions

In this chapter we have demonstrated the reliable use of 32 kHz tuning forks as feedback sensors in buffer solutions. The tuning fork diving bell keeps the tuning fork vibrating in air while only the fiber tip is immersed in liquid. We reproducibly obtain Q factors of at least 200, resulting in a maximum tip-sample interaction force of 350 pN. These forces are low enough to image soft dendritic cells in PBS. Furthermore, we have demonstrated that individual molecules can be detected on the membrane of cells in solution with nanometric optical resolution using NSOM.

The application of NSOM in solution will open the way to high resolution live cell imaging. As a scanning probe technique, NSOM is less suitable for monitoring fast lateral diffusion of membrane complexes, however its superb resolution in the z-direction should allow monitoring of exo- and endo-cytosis processes with high speed and sensitivity. In the rest of this thesis we use the diving bell NSOM described in this chapter to investigate lipid and protein organization in fixed whole cell membranes in solution.

Chapter 3

Unraveling lipid organization using NSOM

The cell plasma membrane of eukaryotic cells is a lipid bilayer which forms the link between cell cytosol and the extracellular environment. The composition and organization of proteins and lipids within this bilayer has a direct impact on many cellular processes like cell-cell interaction or cell activation. Lipid rafts (domains within the membrane enriched in cholesterol and glycosphingolipids) [23] are believed to play a key role in many membrane related processes like immune cell signaling [99] and viral entry [25]. Their existence is however rather controversial, since evidence for the presence of lipid rafts in native cell membranes can only be obtained via indirect methods [29]. Here we demonstrate the ability of near-field scanning optical microscopy (NSOM) to directly visualize lipid rafts, enriched in glycosphyngomyelin (GM1), via fluorescently labeled cholera toxin (CTxB) both in immature dendritic cells (imDC) and human monocytes (THP1) under liquid conditions. Remarkably, on both cell types GM1 nano-domains appear to be smaller than 100 nm in size. Furthermore, exploiting single molecule detection we have quantified the GM1 content of each individual domain. On both cell types, most domains only bind 1 to 6 CTxB molecules, while on THP1 cells, up to 25 CTxB molecules per domain have been identified. These results are consistent with the most recent picture of functional raft pre-cursors as nanoscale entities containing only a few molecules [44].

3.1 Introduction

Our current view of the membrane of eukaryotic cells is one in which lateral heterogeneities formed by patches and domains of membrane components are present. Moreover, lipid rafts, domains enriched in cholesterol and glycosphingolipid, are thought to play an important and active role in the organization and ordering of these membrane domains [23].

The lipid raft hypothesis is supported by the observation of a distinct lipid phase (liquid-ordered, l_o) in model membranes [100]. This l_o phase is insoluble in a non-ionic detergent (Triton X-100) at low temperatures, 4^oC. Applied on cells this leads to observation of detergent-resistant membranes (DRMs) [101], which has become a 'definition' of membrane rafts. Analysis of the DRMs is therefore widely used to study raft composition [29, 44]. However, "detergent resistant membranes should not be assumed to resemble biological rafts in size, structure, composition or even existence" [102], since temperature changes and changes in detergent concentration significantly alter phase behavior and therefore DRM composition [33]. As such, this method is clearly not suited to obtain information on the actual size, shape and dynamics of these domains in living cells. In addition, cholesterol depletion has been also used to investigate the functional dependence of raft partitioning for a wide variety of proteins [35]. Since cholesterol depletion leads to raft dissociation, a loss of protein function upon depletion is attributed to a loss of protein-raft association. However, cholesterol depletion is likely to affect also the cytoskeleton [30] and thus, it is controversial whether a loss in function upon depletion of cholesterol can be directly related to raft association [29]. It is clear that more direct evidence of lipid rafts and their composition in cell membranes of intact cells is needed.

Fluorescence microscopy in living cells has so far failed to directly reveal rafts. When searching for rafts most of the cell surface seems to be uniformly covered with the raft marker, suggesting that any potential rafts are too close to each other to be resolved using fluorescence microscopy [35]. Novel microscopy techniques, have been developed to obtain information on domain size by probing mobility characteristics of individual lipid raft markers [103]. In single particle tracking (SPT), a gold bead is attached to a membrane protein of interest. The position of the gold bead is monitored in time, offering an extremely high temporal resolution (tens of microseconds) and localization accuracy (7-40nm). This technique has revealed membrane compartments for unsaturated lipids (non raft markers) of 230 nm in fibroblasts [104]. Others have studied the compartmentalization of the raft markers Thy1 (a GPI-anchored protein) and GM1 (a glycosphingolipid) and revealed membrane compartments of 260-330nm in fibroblasts [105]. To prevent aggregation of membrane components via antibody coated beads several groups

have exploited the recent availability of sensitive CCD cameras to track individual fluorescent molecules in living cells. Using saturated lipids as raftmarkers in human muscle cells, lipid raft domains ranging from 200-2000nm were observed, whereas non raft markers in the form of unsaturated lipids did not show confined diffusion [81]. On the other hand H-Ras domains of 200 nm on the inner leaflet of both kidney cells and fibroblasts were observed, but these domains were not sensitive to cholesterol extraction [106]. In contrast to the rather large domains observed using single particle tracking, fluorescence resonance energy transfer (FRET), which probes proximity between raft markers, has demonstrated the formation of 'domains' with a diameter of 4-5 nm containing a maximum of 4 (GPI)-anchored proteins [6]. Furthermore an elegant combination of conventional fluorescence microscopy and single particle tracking recently revealed that the mobility of several receptors did not correlate with their traditional classification as raft or non-raft marker [38]. All together the use of different techniques and different raft markers has not brought much consensus on either size or content of lipid rafts and even the very existence of lipid rafts is still under debate [29]. It is highly desirable to use direct optical viewing with spatial resolution beyond the diffraction limit of light, thereby bridging the gap between single particle tracking, FRET and conventional fluorescence microscopy, to investigate lipid organization in a direct way on intact cell membranes.

As described in the previous chapter, near-field scanning optical microscopy (NSOM) breaks the diffraction limit of light, potentially allowing the direct observation of nanometer sized protein domains and lipid rafts. In combination with the tuning fork diving bell [107] NSOM can be used in liquid conditions thereby preventing the potential drying or membrane rupture artifacts prone to occur when using electron microscopy [78, 92]. Here, we use NSOM to investigate the nano-scale organization of lipids in the cell membrane at the single molecule level. Since we are interested in lipid organization we have chosen the ganglioside GM1 as a raft marker, instead of focusing on proteins associated to lipid rafts (like GPIs). GM1 has been postulated to be a major lipid component in rafts [36, 63]. Furthermore, fluorescent markers for this glycosphingolipid are readily available. We studied the spatial organization of GM1 in the membrane of imDCs and cells from a human monocytic cell line (THP1) in buffer solution. Our results demonstrate that with sufficient optical resolution lipid domains can be directly resolved and that these domains contain only a low amount of GM1 lipids. This finding is consistent with the most recent picture of functional raft pre-cursors consisting of only a few molecules [44].

3.2 Materials and Methods

3.2.1 Experimental setup and image analysis

For the experiments described in this chapter we used a home built confocal/NSOM microscope optimized for single molecule detection sensitivity. All experiments were performed in liquid using the diving bell concept described in Chapter 2. For experiments on imDC as well as THP1, the GM1 lipids were visualized via Alexa647 fluorophores attached to cholera toxin beta subunit (CTxB) [108, 109]. ImDCs were investigated using the 647 nm line of an argon/krypton-ion laser (CW, Spectra-Physics), while THP1 cells were investigated using the 632 nm line of a HeNe laser. In confocal mode, circularly polarized excitation light is reflected by a dichroic mirror (Omega Optical Inc.) and focused onto the sample using an oil immersion objective (60x, 1.4 NA or 100x, 1.3 NA). In the NSOM mode, the sample is excited via the fiber probe. The emitted fluorescence is collected and passed through a 510 nm longpass filter to reduce autofluorescence from the NSOM fiber. For the imDC experiments the fluorescence was collected via a dichroic mirror and spectrally separated from the excitation light using a 680 nm longpass filter (Omega Optical Inc.) and detected on a single photon counting avalanche photodiode (APD, SPMC-100,EG&G, Quebec). For the THP1 experiments a polarizing beamsplitter was positioned in the detection path, to facilitate single molecule discrimination based on polarization contrast or dipolar orientation.

To quantitatively analyze the fluorescence intensity images we use a custom written LabView analysis program. In this program a fluorescent spot is defined using a circle with radius r, where r is chosen such that the circle area encloses all pixels with an intensity larger than 15% of the maximum intensity. Moreover the average background signal detected on the bare glass is subtracted for each pixel. By adding all pixel intensities and dividing by the total number of pixels in the spot we obtain an average intensity per pixel. Dividing by the pixel dwell time gives the average spot intensity.

3.2.2 Sample preparation

The THP1 cells were cultured in RPMI 1640 Dutch modification medium supplemented with 10% Fetal Calf Serum and antibiotic-antimycotic from Gibco. For NSOM/confocal fluorescence microscopy labeling, cells were stretched on poly-l-lysine coated coverslips for 45 minutes at 37^oC. After blocking on ice with PBS (containing 3%BSA and 20mM Glycine) for 30 minutes at 4^oC, the cells were labeled with 10μg/ml Alexa647-CTxB (Molecular Probes C-22844) also at 4^oC

to minimize internalization of CTxB and crosslinking of lipid rafts [110]. After washing three times with PBS the cells were fixed using 1% PFA in PBS for 20 minutes at room temperature, followed by two PBS washing steps and again blocking for 1 hour. Wet samples were stored in PBS containing 1% PFA until use. ImDCs were obtained as reported elsewhere [66]. In brief we first obtained monocytes from buffy coats (fraction of a centrifugated blood sample that contains most of the white blood cells) of healthy individuals, which were purified using Ficoll density centrifugation. DCs were cultured from monocytes in presence of IL-4 and GM-CSF (500 and 800 U/ml, respectively) for six days to obtain imDCs. Fluorescence labeling has been performed using the same protocol as for THP1 cells.

3.3 Results

3.3.1 Measuring lipid rafts on imDC and THP1 cells

Samples containing imDCs labeled with CTxB-Alexa647 were mounted in a liquid cell covering the sample with ∼1ml of PBS solution. We have selected individual, well stretched cells, using a CCD camera and bright-field illumination. The selected DC is then imaged in confocal mode and a region of interest is selected for detailed confocal and near-field investigation. A representative confocal fluorescence image of a selected part of the cell is shown in Figure 3.1 **A**. A homogeneous distribution of fluorescence is observed, consistent with the view of lipid rafts as small but abundantly present structures on the membrane. The same cell area is also inspected with NSOM, where topographic information is shown in Figure 3.1 **B** and the simultaneously obtained near-field fluorescence image is shown in Figure 3.1 **C**. The brighter areas in **B** correspond to higher parts of the cell, up to a few microns in height, while to the edges small dendrites of only 100 nm in height are clearly visible. In Figure 3.1 **C**, which has the same spatial scale as the confocal image, one starts to distinguish inhomogeneities and individual fluorescent spots on the cell membrane, which become strikingly evident in the detailed image shown in Figure 3.1 **D**. In the cell area, identified by means of the topographic information, a non-uniform fluorescence distribution and in particular, individual fluorescent spots are clearly observed, indicating the presence of lipid domains. The domains appear to be slightly elongated along the vertical direction, as a result of weak tip-sample interactions which result in a reproducible displacement of the soft cell membrane.

Using confocal fluorescence microscopy we observed that the GM1 content in the membrane of imDCs is significantly lowered with respect to its monocyte

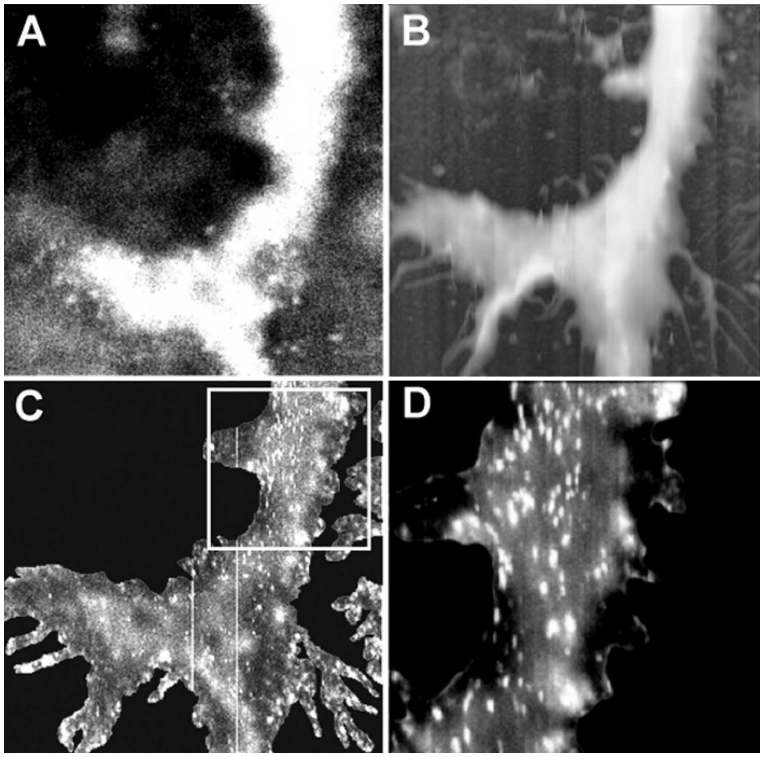

Figure 3.1: Spatial distribution of GM1 in the membrane of an imDC. GM1 is fluorescently labeled via CTxB-Alexa647. Confocal fluorescence image of a region of interest 15x15μm (**A**); NSOM images of the same area (**B** and **C**). Here (**B**) is cell topography and (**C**) is the simultaneously obtained near-field fluorescence image. The topographic information is used to exactly define the cell borders. (**D**) Zoom-in NSOM fluorescence image (7x7 μm) in the region indicated by the white box in **C**.

precursor (B. Joosten, personal communication). Therefore we decided to also investigate the distribution of GM1 in the membrane of THP1 cells, a cell line closely related to human monocytes. For high resolution imaging, we followed a similar procedure as used for imDCs. A representative confocal image of a THP1 cell is shown in Figure 3.2 **A** together with an enlarged image shown in Figure 3.2 **B**. The same area has been also investigated with the NSOM and the resultant image is shown in Figure 3.2 **C**. Spatially separated fluorescent spots and patches are clearly resolvable in the NSOM image despite the higher content of GM1 in this cell type as compared to imDC. The lateral resolution in Figure 3.2 **B** is 350 nm, close to the diffraction limit of light, while the lateral resolution

in the NSOM image shown in Figure 3.2 **C** is 100 nm. To our knowledge, this is the first time that GM1 organization is directly visualized by optical means on intact cells in solution at such high spatial resolution.

3.3.2 Determining the fluorescence intensity of individual CTxB molecules

The number of CTxB molecules contained in each domain is directly related to the domain fluorescent intensity. However, in order to quantify its intensity it is necessary to determine first the intensity of individual Alexa647-labeled CTxB molecules. In addition to the fluorescence emission arising from raft domains on the cell surface also weaker fluorescent features are observed in Figure 3.2 **C**, most likely corresponding to individual CTxB molecules unspecifically bound to the glass surface. To quantify the fluorescence arising from these spots and to determine the number of Alexa647 molecules attached to the CTxB, we have measured fluorescence time trajectories for individual CTxB molecules bound to the glass surface. To that end, the confocal excitation light was placed directly above an isolated CTxB spot and the fluorescence emission was monitored in time. A typical time trace from an individual CTxB molecule is shown in Figure 3.3. The time trace exhibits different intensity levels, consistent with the presence of multiple Alexa647 fluorophores per CTxB. The last intensity step corresponds to the intensity of an individual fluorophore. Over 35 traces, normalized to an excitation intensity of 1 kW/cm^2, we find an average intensity of 1.8±0.1 kC/s (with FWHM of 1 kC/s) for this last step, i.e., the photon emission of a single Alexa dye. We then relate the average intensity of this last step to the average intensity of 37 individual CTxB spots under similar excitation conditions. Here we find an average intensity of 16±1 kC/s (with FWHM of 14 kC/s). This indicates that each CTxB molecule is labeled with 9 Alexa647 molecules, with a standard deviation of ∼9 fluorophores per CTxB, in good agreement with the manufacturer specification (Molecular Probes) of 5-10 fluorophores per CTxB. Differences in labeling efficiency in combination with a stochastic binding process can explain this variability in chromophores actually labeling the CTxB molecule. These results also indicate that we can safely use the fluorescence intensity from individual Alexa-647 labeled CTxB molecules on the glass as a reference value to accurately determine the fluorescence intensity and thus the content of the lipid domains on the cell membrane.

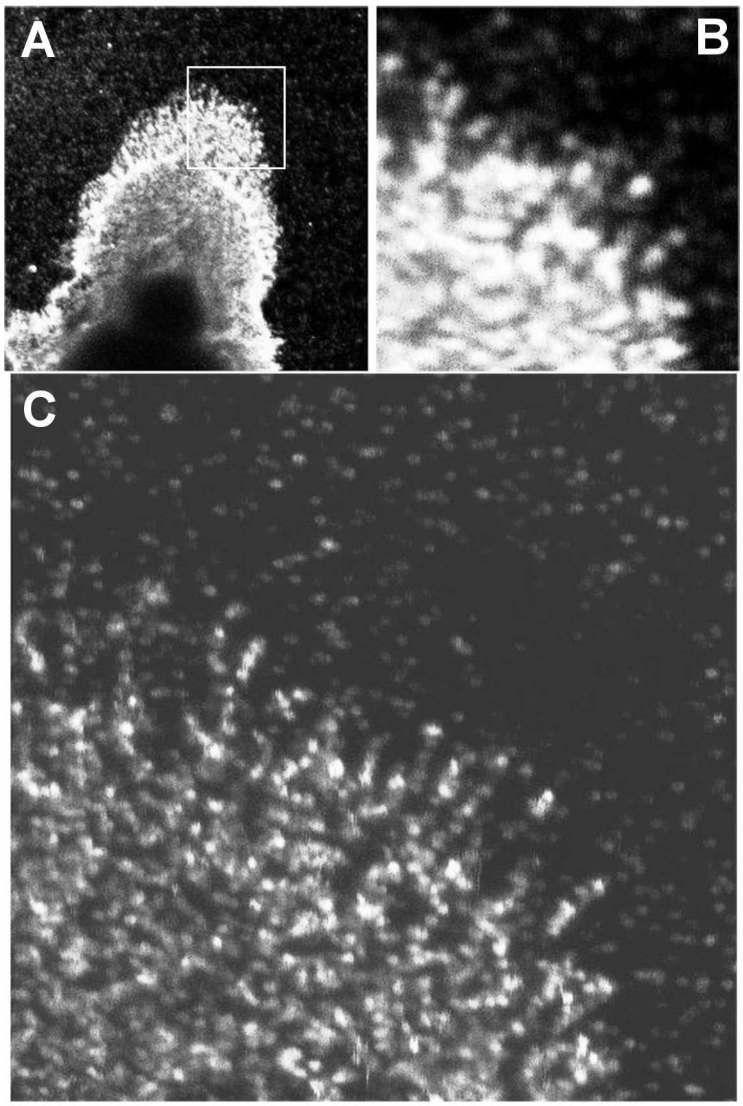

Figure 3.2: Near-field scanning optical microscopy maps lipid raft organization on THP1 cells in liquid. A large area (40x40 μm) of a THP1 cell is first imaged in confocal mode (**A**). A region of interest (white box in **A**, 10x10 μm) is then imaged in confocal (**B**) and NSOM (**C**) modes.

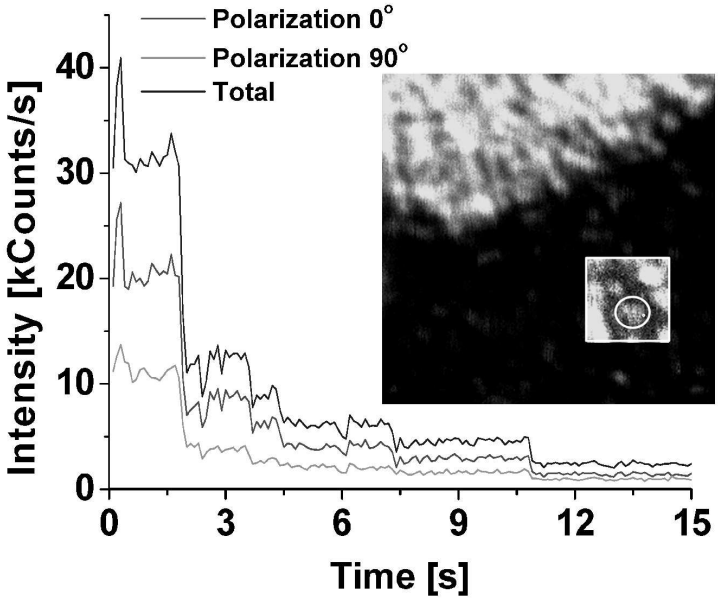

Figure 3.3: Single molecule fluorescent trajectories allow determination of the number of fluorophores contained in each CTxB molecule. The inset shows a confocal image of individual Alexa647 labeled CTxB molecules on a glass coverslip next to a THP1 cell. The intensity scaling has been locally changed (indicated by the white box) so that individual CTxB spots are visible on the glass surface. Scan size 10x10 μm^2 (256x256) pixels and an excitation intensity of $\sim$1kW/cm^2. The fluorescence emission as a function of time for the bright encircled fluorescent spot is shown in the time trajectory. Fluorescence signal was collected at 1 ms acquisition time (binning 100ms).

3.3.3 Lipid rafts quantified on THP1 and imDC

Having identified that the spots on the glass indeed correspond to individual CTxB molecules we then related the fluorescence intensity of those spots (obtained by confocal) to those obtained using NSOM. From 7 independent NSOM images we identified 677 spots on the glass coverslip. Since we used different NSOM tips (90-110 nm) resulting in slightly different excitation intensities, all images are normalized with respect to the glass background intensity. The intensity distribution for CTxB spots on glass is displayed in Figure 3.4 **A**. The size of these spots is determined using the full width at half maximum (FWHM) of a two dimensional Gaussian fit to the intensity profile. The FWHM is calculated as the average of the FWHM in the x and y direction. The resulting size distribution is given in Figure 3.4 **B**. The intensity distribution peaks at $\sim$9 kCounts/s and

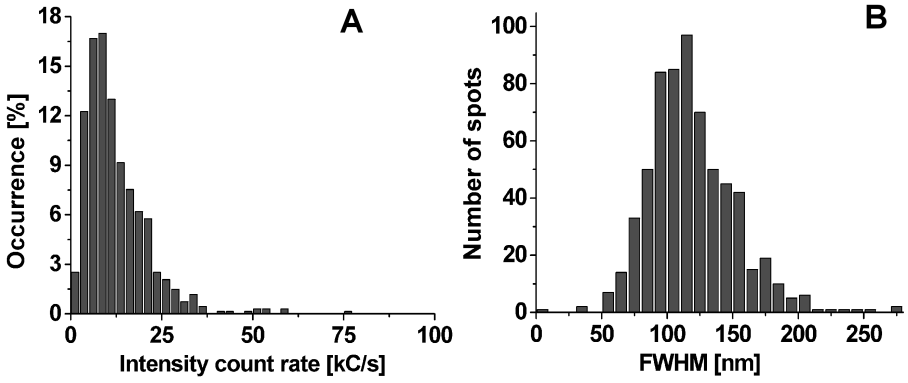

Figure 3.4: The intensity distribution (**A**) and size distribution (**B**) of isolated fluorescent CTxB spots on the glass coverslip obtained from 677 spots collected from 7 NSOM images. Tip aperture diameter: 90-110 nm.

the size of the spots is centered around 110 nm. The tips used in this experiment were 90-110 nm in diameter, indicating that the measured spot sizes result from tip convolution. The very small features are probably caused by abrupt changes in fluorescence intensity related to topography spikes or dips in combination with single molecular photodynamics, such as blinking and bleaching.

In a similar fashion we obtain the intensity distribution for the lipid raft domains on the THP1 cells. Only fluorescent spots showing clear contours were included in the analysis, since we attribute the weaker, less intense patches to fluorescence of internalized CTxB. The resulting intensity distribution for 485 spots from 4 different cells is shown in Figure 3.5 **A**. On THP1 the distribution peaks at 50 kC/s, i.e. 5-6 CTxB while the distribution is extended to domains that host up to 25 CTxB molecules. The domain size distribution is shown in Figure 3.5 **B**. The distribution is centered around 120nm and only slightly shifted towards larger values with respect to the size of individual CTxB, indicating that the actual distance between multiple CTxB in a domain is far below 100 nm for the large majority of the lipid domains. The slight shift towards larger values might result from the fact that on the cell the CTxB spots appear slightly elongated. Since the FWHM is the average of the FWHM in both directions, a slight elongation results in a small bias towards larger FWHM values.

To quantify the content of the lipid domains on imDC, we again compare the fluorescence intensity of each domain to the fluorescence intensity of individual CTxB molecules on the glass substrate. In these experiments there was considerable unspecific binding of CTxB to the glass substrate and therefore we

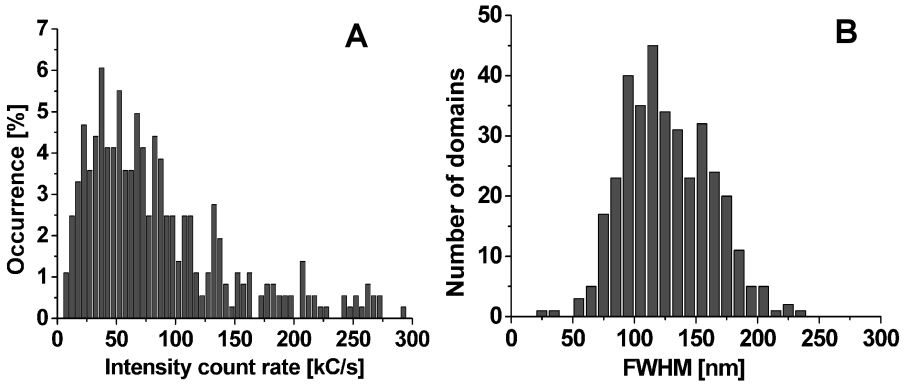

Figure 3.5: Intensity distribution (**A**) and size distribution (**B**) obtained from 485 fluorescent CTxB spots on the membrane of 4 THP1 cells. Tip aperture diameter: 90-110 nm.

selected CTxB domains located on the cell by using the topography as a mask, thus identifying the exact position of the cell. A typical domain intensity distribution as obtained from the image in Figure 3.1 **D**, is shown in Figure 3.6 **A**. The fluorescence intensity of single CTxB molecules on the glass substrate is also included (*white bars*) in the same histogram. In this particular example, the ratio in intensity is roughly a factor of 2, as is obvious by comparing the peak value of both histograms. However, the CTxB distribution on the cell also shows a tail towards higher brightness, indicating different domain packing. For 8 cells investigated we find average ratios ranging from 1 to 4 indicating 1 to 4 CTxB molecules per domain. Moreover, all distributions have an extended tail to the higher count rate values consistent with the binding of multiple CTxB molecules. The apparent size of the lipid rafts on imDC domains has been obtained using the same analysis as for the THP1 cells. The FWHM distribution is shown in Figure 3.6 **B**. This distribution again peaks around 100 nm indicating that the distance between the few CTxB molecules binding to a lipid raft on imDC is also far below 100 nm.

We further investigated the surface distribution of the lipid rafts by calculating the minimum distance between domains (nearest neighbor distance (nnd) analysis). The position of the rafts in the x-y plane has been determined using the center of mass for each fluorescent spot after fitting to a 2D Gaussian. These positions are used to determine the distance between each particle and its nearest neighbor. The resultant nnd distributions for THP1 and imDC are shown in Figure 3.7. In Figure 3.7 **A** the peak of the distribution lies at 250nm for lipid

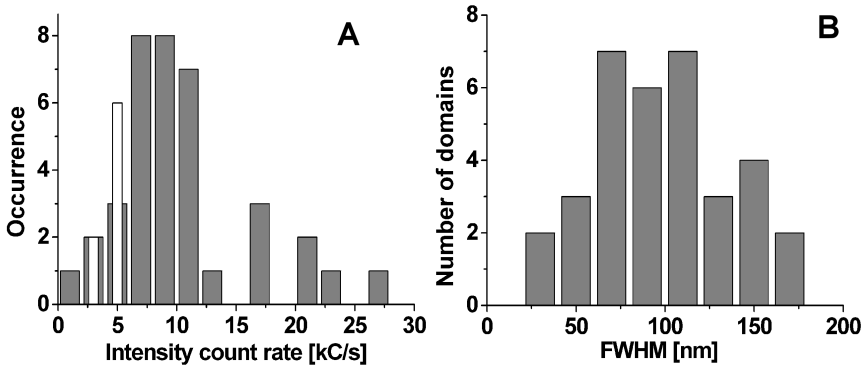

Figure 3.6: Intensity (**A**) and size distribution (**B**) obtained for 35 fluorescent CTxB spots on the membrane of the imDC in Figure 3.1 **C**. This distribution is compared to the intensity of some individual CTxB molecules on the glass substrate (*white bars*).

domains in THP1 cells, while on imDCs the distances are slightly larger peaking around 350 nm (Figure 3.7 **B**). Since we can not separately observe domains with distances smaller than 100 nm, due to our probe size, the real nnd will be slightly lower especially for the more crowded THP1 cells.

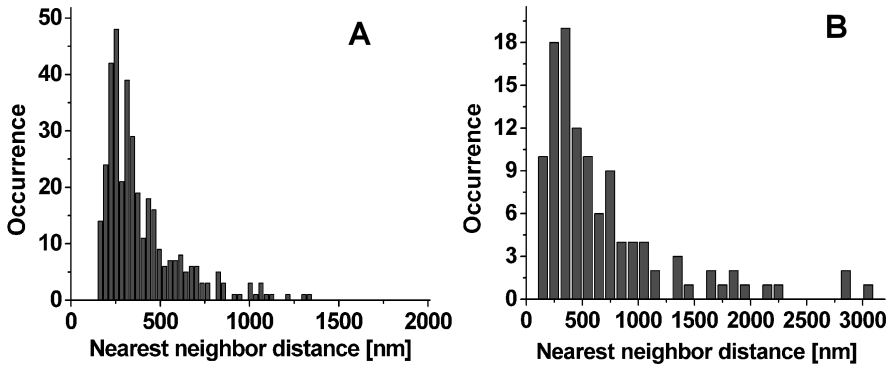

Figure 3.7: Distribution of inter-CTxB domain distance obtained by nnd analysis of all measured fluorescent spots. The distribution in A is obtained for CTxB spots on THP1 (n=360), while the distribution in B is obtained for imDC (n=113).

3.4 Discussion

In this chapter we have demonstrated that with sufficient optical resolution ultra small domains can be directly resolved in the membranes of imDCs and THP1 cells. We associated these domains to lipid rafts as we visualized the distribution of the raft lipid GM1 using fluorescently labeled CTxB. Although we have been able to quantify the number of CTxB molecules per domain for both THP1 and imDC we still need to relate these values to the number of GM1 lipids involved in these domains. If we assume a perfect packing of the lipid bilayer without any proteins and consider the pentavalent nature and size of the CTxB molecule [111, 112], then the maximum number of GM1 lipids present underneath one CTxB molecule can be estimated. One CTxB molecule binds specifically to 5 GM1 lipids, but due to its size it can cover up to 30 GM1 molecules as illustrated in Figure 3.8. In a real cell membrane this maximum number will probably be lower, due to the presence of proteins, different lipid species and the non-perfect packing of the lipids. From our experiments on imDC we have observed on average the binding of 1 to 4 CTxB molecules suggesting the presence of at least 5 to 20 GM1 lipids within a lipid raft. These small CTxB clusters are consistent with recent experiments using TEM on dried membrane sheets of a rat mast cell tumor line [45], where gold conjugated CTxB was observed to be primarily distributed as single entities. For THP1 cells domains are slightly denser containing on average 5-6 CTxB molecules but the distribution extends towards 25 CTxB molecules per domain. This suggest an underlying GM1 distribution of 25-30 to a maximum of 125 GM1 lipids.

Interestingly the increased GM1 content in THP1 cells results both in domains binding more CTxB (5-6 CTxB on THP1 in contrast to 1-4 on imDC) as well as smaller inter domain distances (250 nm on THP1 and 350 nm on imDC). This suggests that an increased GM1 content results in more lipid rafts, that are slightly enriched in GM1 lipids. In fact these results are a mixture of the classical raft picture (raft size increases with density) and the alternative model recently proposed by Plowman and co-workers [113] suggesting that rafts have an upper size limit and the number of small raft domains increases upon increased GM1 content.

A further issue that remains to be investigated is whether the apparent clustering observed is real or simply the result of a random ordering of individual CTxB molecules present at a high density on the cell membrane. Despite the superior resolution provided by NSOM, the final resolution is still limited by the probe size, which might result in multiple CTxB molecules present underneath the NSOM probe. On the other hand, most domains appear tip convoluted in size indicating that the distance between individual CTxB molecules is at maxi-

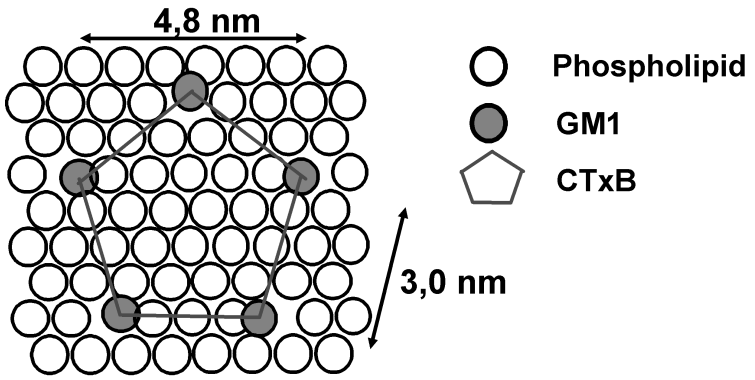

Figure 3.8: Cartoon illustrating the binding of a CTxB to a lipid layer. The surface area of an individual phospholipid is 0.4 nm^2. Due to its physical dimension one CTxB molecule can cover a maximum of 30 lipids upon binding.

mum 40 nm, suggesting that the small domains result from real associations. To clarify this issue it is crucial to compare the experimentally obtained distribution with simulations for random distributions at similar packing densities, which is the main subject of the next chapter.

The measured spot sizes result from a convolution between the probe aperture (90-110 nm) and the real size of the spot. Thus, the peak in the measured size distribution around 100 nm indicates that the real domain sizes are well below 100 nm. Both, the small size and the low GM1 content of the raft domains are consistent with the most recent picture of functional raft pre-cursors consisting of only a few molecules [44]. We have also tried to correlate spot size with intensity but did not find any clear correlation between both quantities implying that the larger spots do not necessarily appear to be the brightest. In fact, we even found one spot of 110 nm containing 25 CTxB molecules. Since the smallest surface area that 25 CTxB molecules can occupy has a dimension of 25x25 nm, which is well below the size of our NSOM probe, the resulting spot will indeed have a size comparable to the probe aperture.

If we compare the peak in the nnd distribution for imDCs with the resolution of our diffraction limited confocal microscope ($\sim 0.5\lambda$) we would have expected to also resolve some CTxB domains with confocal microscopy on imDCs, which has not been the case in our experiments. Most probably background fluorescence from internalized CTxB does prevent this observation. Illumination with the NSOM probe is restricted to the first 150 nm and therefore less sensitive to the contribution of internalized CTxB. On the other hand, we have checked the

extent of internalization on THP1 cells using anti-CTxB antibodies labeled with secondary fluorescent antibodies. Since both markers heavily co-localize we conclude that labeling at 4^oC prevented most CTxB from internalization. Still some fainter larger patches could be observed in our NSOM images, an indication that internalization was not fully prevented.

It is important to mention that although CTxB has been primarily used to identify the GM1 rich lipids rafts [40, 63, 110], binding of the CTxB pentamer brings together 5 GM1 molecules. This might induce GM1 redistribution, which can in turn result in unwanted cell signaling [45]. Nevertheless, we performed labeling at 4^oC which in principle should minimize cross-linking and cell signaling. Of course, the use of alternative probes to label GM1 or other raft lipids in a one-to-one ratio is highly desirable and might alleviate this problem. However, one should be aware that direct labeling of lipids changes the lipid structure inducing phase separation in model membranes [114] and thus direct labeling is likely to influence raft partitioning in cell membranes.

In this chapter we have focussed on the distribution of GM1, since it is commonly accepted as a lipid raft component and fluorescent markers are readily available. Several groups have studied rafts via GPI-anchored proteins [6, 63], but studying protein distribution does not necessarily reveals the underlying lipid distribution. For instance, TEM studies using immunogold labeling have already demonstrated that the GPI-anchored protein Thy-1 only rarely co-clusters with GM1 in mast cells [45]. Since most proteins are identified as raft markers, based on biochemical experiments it is crucial to investigate if this association really reflects the distribution in the cell membrane. This issue will be further addressed in Chapter 6 where we investigate the distribution of both lipids and proteins using NSOM for high resolution co-localization studies.

NSOM is a scanning technique, which is inherently slow and non-capable to capture the fast dynamics associated to raft formation. Fixation is prerequisite to obtain a still image, i.e. all membrane components are fixed and the image represents a snap-shot of the membrane that maps at a given moment the entire process of formation or existence of domains, rendering information on all possible situations. Here we only observe very small lipid rafts consistent with the most recent picture of functional raft pre-cursors consisting of only a few molecules [44]. It would be interesting to investigate if we can stimulate these cells and induce larger functional rafts. If the current hypothesis of tiny raft-precursors is true and the formation of larger functional rafts is a diffusion assisted process, NSOM snap-shots should reveal evidence for 'lipid raft nucleation and coalescence'.

3.5 Conclusion

In this chapter we have shown that NSOM, as a high resolution optical technique, is ideally suited to investigate the organization of the plasma membrane of cells in liquid. For the first time we have directly resolved nanometer scale lipid heterogeneities by optical means. Lipid domains with sizes well below the diffraction limit have been visualized on both THP1 cells and imDCs. Furthermore, their content has been estimated based on domain brightness and using single molecule sensitivity for brightness calibration. The intensity distribution on THP1 cells peaks at 5-6 CTxB, but the distribution extends towards 25 CTxB molecules per domain. On imDC spots contain on average 1-4 CTxB molecules. The distance between raft domains in THP1 cells is shorter than for imDCs, due to differences in GM1 membrane content. The small lipid domains observed here using NSOM are in perfect agreement with the recent concept of lipid raft precursors. However, is the apparent organization in nanoscale domains real or could these domains also result from a random ordering of individual CTxB molecules at a high density? The next chapter will further clarify this issue.

Chapter 4

Clustering vs. random distribution: experiment and simulations

Clustering of cell plasma membrane components is accepted as an important mechanism to regulate cell function. While the formation of large signaling complexes is easily visualized via imaging using fluorescence microscopy, imaging small nanometer sized clusters using similar techniques is often impossible due to a combination of limited optical resolution and high expression levels of the labeled membrane component. In fact, at high packing densities, two or more particles that have no association can coincide within the same excitation volume resulting in brighter fluorescent spots and apparent clustering. The higher the density and the lower the imaging resolution, the more apparent clustering will result. Although near-field scanning optical microscopy (NSOM) provides superior spatial resolution, individual fluorophores within a nanometer-sized domain cannot be directly resolved. As a consequence, domain content still needs to be quantified based on fluorescence intensity. Here we demonstrate that experimentally obtained fluorescence images can be compared to simulated images of randomly distributed particles at densities related to experimental conditions in order to assess the degree of true clustering. We have used these simulations to investigate the degree of true clustering of the lipid raft marker GM1 labeled with CTxB on the membrane of THP1 cells in solution. The combination of high resolution optical microscopy and computer simulations has allowed us to unequivocally demonstrate nano-scale clustering of GM1, providing evidence that nanometer sized lipid domains (lipid raft pre-cursors) indeed exist in the cell plasma membrane.

4.1 Introduction

The organization of proteins and lipids into domains on the plasma membrane can be directly related to cell function [115, 116]. This non-random spatial organization deviates from the original picture of the cell plasma membrane as a random mixture of protein and lipids [1]. As long as aggregates contain a large number of proteins they are easily visualized by conventional diffraction limited microscopy as is the case for large signaling structures such as the immunological synapse [117] or adhesive structures like podosomes [118]. More complicated and therefore more challenging to study is the formation of small scale aggregates, with sizes below the diffraction limit of light and accommodating only a handful of proteins and lipids. Electron microscopy (EM) in combination with immunogold labeling has been used by several groups to reveal protein domains not accessible with light microscopy [45, 59, 77, 78, 113]. Generally a point pattern image reflecting the gold particles and thus the underlying protein distribution is obtained. The point pattern images are analyzed using statistical algorithms (Poisson distribution, nearest neighbor distance (nnd) analysis and Ripley's K analysis [119]) to quantitatively discriminate between random surface organization and clustering. Briefly, the Poisson distribution gives the frequency distribution of the number of gold particles within boxes of a given size spaced uniformly across the image area. Deviation from this distribution, i.e. more particles in a box than expected, is indicative for clustering. Similarly a nnd frequency distribution with smaller distances as compared to the nnd frequency distribution for complete spatial randomness (CSR) is again indicative for clustering. The Ripley's K function on the other hand, evaluates all interparticle distances over the studied area and compares the observed distribution with that expected for CSR. If the number of neighbors within a set distance is larger than expected for CSR, then the particles are clustered. Although very interesting information on aggregation at the nanometer scale is readily obtained using electron microscopy, the technique requires extensive sample preparation. Samples have to be fixed and dehydrated, most likely influencing the observed spatial distribution. Moreover, experiments have to be performed under vacuum conditions and as such electron microscopy is clearly not suited for live cell imaging.

Fluorescence microscopy is compatible with live cell imaging, but lacks the spatial resolution to create point pattern images in crowded samples. Insight into aggregation can be obtained via different experimental configurations, mostly relying on differences in fluorescent brightness between clusters and individual molecules. For instance, based on the fluorescence brightness of dimers vs dimers of dimers, single particle fluorescence imaging [120] revealed the formation of dimers of dimers for a leukocyte antigen on the membrane of living fibrob-

lasts [121]. A similar study based on the brightness of individual DiI-labeled LDL particles demonstrated receptor clustering in fibroblasts [122, 123]. Another quantitative approach is image correlation spectroscopy (ICS) [124] an imaging technique analogous to fluorescence correlation spectroscopy. ICS has revealed changes in receptor distribution in human fibroblasts [125, 126]. Essentially the technique is based on calculating the autocorrelation function of a whole image. The zero value of the autocorrelation function is inversely proportional to the average number of independent fluorescent entities in the observation volume, i.e. average number of clusters, while the total image intensity relates to the total number of fluorescent molecules in the image [127]. Together these numbers yield an estimate on the number of fluorophores per cluster. However, for this approach the cluster size is assumed to be homogeneous, withholding information on heterogeneity amongst the clusters and ignoring the presence of both monomers and clusters together. Alternatively, fluorescence resonance energy transfer (FRET) is an exquisite technique sensitive to the association between receptors in living cells, although information on the extent and/or stoichiometry of such associations is hard to obtain [42, 128].

Single molecule microscopy has become in recent years a powerful technique for quantitative determination of local stoichiometries [129]. The technique works excellent for low receptor density, or when the clusters are sufficiently separated in space. Yet, the exact quantification of fluorophores per cluster is influenced by photon statistics and therefore its accuracy drops with increasing cluster size. Fluorescence fluctuation spectroscopy is another single molecule-based technique, that has been also used to provide information about protein interactions in the intercellular environment based on statistical analysis of the fluorescence fluctuations caused by fluorophores passing the illumination volume. Here the molecular brightness of fluorescent proteins is determined from the fluctuations by analyzing the photon counting histogram (PCH) [130, 131]. Changes in the brightness are then related to the oligomerization state of proteins, although no information on spatial organization can be obtained [132].

Recently our group demonstrated the application of single molecule sensitive near-field scanning optical microscopy (NSOM) to quantify receptor clustering in crowded cell membranes [91]. These studies revealed an enormous heterogeneity in cluster size and content, information not accessible with any of the other fluorescence based techniques. We have also demonstrated that NSOM is capable of imaging cells in liquid revealing the existence of small lipid domains with sizes well below the diffraction limit of light. Nevertheless, although NSOM provides superior spatial resolution as compared to confocal microscopy, it is still not possible to identify individual fluorescent particles at fluorophore densities

exceeding 100 particles/ μm^2. A point pattern analysis as used for EM images is therefore not applicable to fluorescent images. In principle, domain intensity analysis can be directly related to the number of particles in the domain, but especially for small clusters, this information should be critically examined in the context of optical resolution. Indeed, in highly packed samples multiple particles might be present within the excitation volume, without real association between them.

In this chapter we demonstrate how we can discriminate clustering from random distribution in experiments with high particle densities but small cluster sizes. We have performed computer simulations of randomly distributed particles at different packing densities and have generated simulated images using different resolution settings. Spot intensity distributions resulting from the simulations are then compared with intensity distributions obtained from NSOM experiments. Simulated random particle distributions reveal that domain-like fluorescent patterns can indeed be the result of imaging a random particle distribution with insufficient optical resolution, misleadingly indicating receptor clustering. We have also applied this methodology to analyze NSOM images of CTxB-Alexa647 labeling GM1 domains on THP1 cells in solution. Our analysis indicates that the CTxB fluorescent spot intensity distribution cannot be described using a random particle distribution. Thus, true GM1 aggregation is observed, providing evidence that nanometer sized lipid domains do indeed exist in the plasma membrane of cells.

4.2 Simulating random surface organization

4.2.1 Image simulation

To generate 'random fluorescence distribution images' we have developed a dedicated LabView program. The simulation places particles at random positions in a 2D area similar in size to the typically obtained optical image. Furthermore, the program uses resolution settings to display apparent particle sizes. For convenience in the rest of this chapter we refer to this 2D area as 'simulated image'. The adjustable parameters in the program are: image area in μm^2 (A), pixels per line (P_l), particle density (D) in particles/μm^2, particle brightness (I) in counts, particle intensity standard deviation (I_d) in counts and imaging resolution (R) in nm. During the simulation, A and D are used to calculate the total number of particles that will be distributed in A. The (x, y) coordinates of each individual particle are obtained from a random number generator. In this way particles with the size of a single pixel are randomly distributed in the simulated image area.

To include the effect of a limited optical resolution these pixels are convoluted with a 2D Gauss with a full width at half maximum (FWHM) that is equal to the resolution settings (R).

In addition to simulations for a random particle organization, we simulated real clustering. In this case, one defines the percentage (x %) of particles distributed as monomers, while 100-x % of the particles are organized in clusters. To this end the cluster parameter C is introduced as an input parameter, where C is the average number of particles per cluster and C_d is the standard deviation. Both clusters and individual particles are positioned randomly on the surface.

Some simulated images of individual particles at different particle densities and imaging resolution are shown in Figure 4.1. If the particle density is low (1 particle/μm^2), individual particles are easily discriminated both in high resolution Figures 4.1 **A** and **C**. However, when the resolution is comparable to that of confocal microscopy, some brighter features are already visible at this low packing density, as shown in Figure 4.1 **E**, indicating multiple particles present within the 'illumination area'. For the higher particle density (20 particles/μm^2), the same apparent 'clustering' effect already occurs at 100 nm resolution while the image with 350 nm resolution (**F**) shows large intensity fluctuations. These simulations demonstrate that depending on resolution and particle density even a random particle distribution can result in images with large intensity fluctuations, at first sight indicative for receptor clustering, but being in fact the consequence of the limited optical resolution in combination with high packing density.

4.2.2 Image analysis

As a test of randomness for the simulated images, we have performed Poisson analysis, i.e. the frequency distribution of the number of particles within boxes of a given size spaced uniformly across the image area. The Poisson distribution is defined as:

$$P(N, \lambda) = \frac{e^{-\lambda}\lambda^N}{N!}, \tag{4.1}$$

where λ is the expectation value, i.e., the average particle density per box, and N is the number of particles in a box. This probability distribution can be converted into a frequency distribution by multiplying with the total number of boxes in the image. Since Poisson is defined for point processes, the box size should be larger than the particle size. In Figure 4.2 **A** we obtain the particle per box distribution for a 5x5 μm^2 selection from the simulated image in Figure 4.1 **B** using 100 boxes with dimensions of 25 x 25 pixels, large enough to expect multiple particles per box. N is obtained dividing the integrated intensity by the intensity

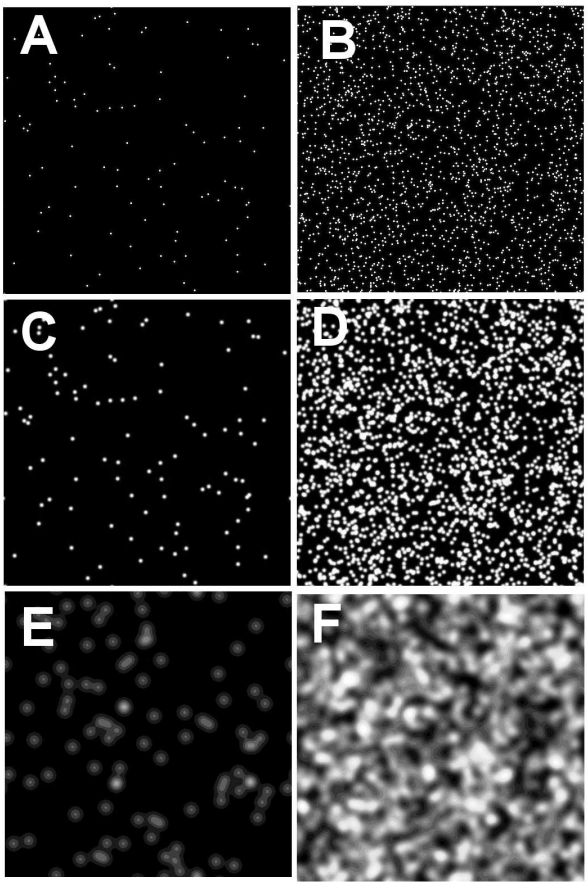

Figure 4.1: Simulated fluorescence intensity images obtained from a distribution of random particles for two different particle densities and three different imaging resolutions. The simulation settings for these images are A = 10x10 μm^2, P_l = 512 pixels, I =1000 counts and I_d = 0 counts. Simulations are performed for two different particle densities: D = 1 particle/μm^2 in (**A**,**C** and **E**); and D = 20 particles/μm^2 for (**B**,**D** and **F**). Each particle density simulation is imaged with three different resolution settings: R = 20 nm for (**A** and **B**), R = 100 nm for (**C** and **D**) and R = 350 nm for (**E** and **F**).

of an individual particle (I =1000 counts, for this particular image). The expected Poisson frequency distribution is calculated using $\lambda = 4.77$, taking into account the particle density of 20 particles/μm^2 and box size of 480 nm^2. The difference between the particle per box distribution and the calculated Poisson distribution can be expressed using the mean square error between these distributions (χ^2), resulting in a χ^2 of 2.38 and indicating that indeed the simulated image is well described by a Poisson distribution. However, for a finite imaging resolution where the particle size approaches the box size the particle per box distribution starts to deviate from the expected Poisson distribution. This is illustrated in Figure 4.2 **B**, where the box size was 480 nm and the particle size 350 nm. In this case χ^2 is 47. Furthermore, to demonstrate the effect of real clustering, Figure 4.2 **C** shows the particle per box distribution as obtained for a simulated clustered image, together with the calculated Poisson distribution. To obtain the simulated image we used similar basis settings as for Figure 4.1 **B**, that is D = 20 particles/μm^2 and R = 20 nm, but we assigned 70 % of the particles to clusters containing 4 $\pm$ 2 particles. The clustered particle distribution clearly deviates from a Poisson distribution ($\chi^2 = 45$). While the Poisson distribution peaks at around 4 particles per box, the particle per box distribution has a completely different shape with a tail towards larger number of particles per box, consistent with particle clustering. Here also the weakness of only evaluating χ^2 is apparent, since both particle per spot distributions in Figure 4.2 **B** and **C** have a very different shape, but χ^2 takes a similar value. This is because χ^2 only reflects the mean square difference and does not take into account the shape of the distribution.

In practice it is not only relevant to discriminate between a clustered and random distribution of particles, but it is also important to obtain information on cluster content. We therefore used fluorescent spot intensity distributions to analyze both simulated and experimentally obtained fluorescent images. As already shown in the previous chapter these intensity distributions can indeed reveal domain content. Now the spot intensity distributions are also compared to simulations using a random particle distribution in order to assess the degree of true clustering.

The spot intensity distributions are obtained through analysis of the simulated fluorescence images by a custom written LabView analysis program (see Chapter 3). Briefly, a spot is defined using a circle with radius r, where r is chosen such that the spot diameter corresponds to the imaging resolution. By adding all pixel intensities and dividing by the total number of pixels in the spot we obtain an average spot intensity. The average spot intensity (I_{av}) is directly related to the number of particles in the spot (N) by taking into account the

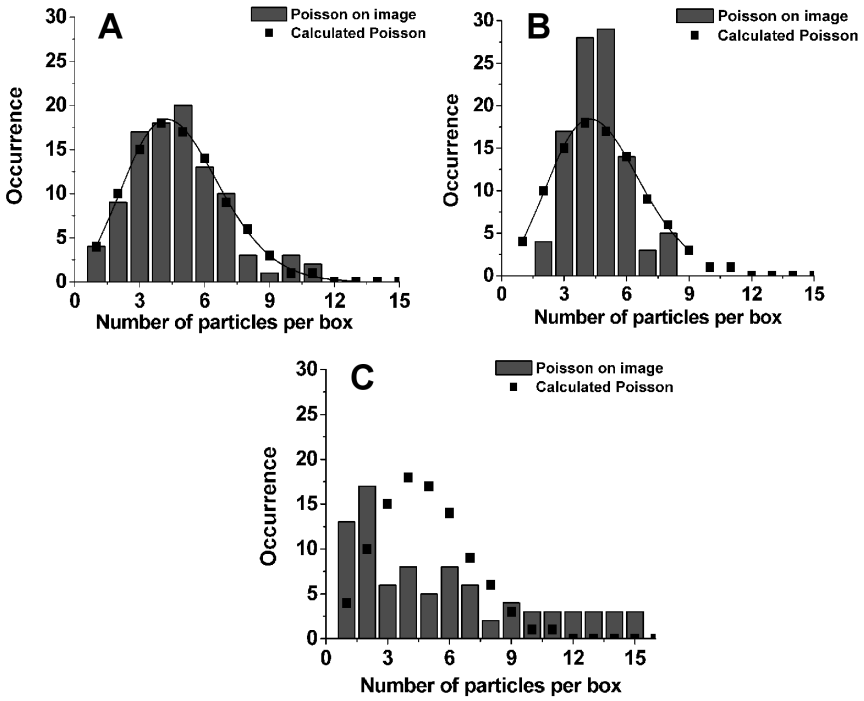

Figure 4.2: Poisson distribution describes correctly random organization in point pattern images. (**A**) Particles per box (bars) as obtained for a 5x5 μm^2 selection from the the image in Figure 4.1 **B** (D = 20 particles/μm^2 and R = 20 nm) using a box size of 25x25 pixels (480 nm). The difference with the calculated Poisson distribution (line) using $\lambda = 4.77$ results in $\chi^2 = 2.38$. (**B**) The particles per box (bars) as obtained for a 5 μm^2 selection from the image in Figure 4.1 **F** (D = 20 particles/μm^2 and R = 350). The difference with the calculated Poisson (line) results in $\chi^2 = 47$. In (**C**) the effect of real clustering on the particles per box distribution is demonstrated. Simulation settings: 70% clusters with $C = 4 \pm 2$, D = 20 particles/μm^2, box size is 480 nm. The difference with the calculated Poisson distribution for non-clustering (line) results in $\chi^2 = 45$.

intensity obtained for an individual particle. Fluorescent spot intensity distributions were deduced after analyzing selected areas of 5x5 μm^2 (256x256 pixels) from the simulated images shown in Figure 4.1. For the 100 nm and 350 nm resolution settings, a spot with respectively a 3 or 10 pixel radius was used, corresponding to a spot FWHM of 120 and 390 nm and an area of 0.01 and 0.12 μm^2 respectively. Using these spots all intensity features in the image were selected. In very large patches we locate multiple spots. This analysis resulted in the in-

tensity distributions (occurrence vs. particles per fluorescent spot) as shown in Figure 4.3. To calculate the Poisson distribution for the different simulations, λ is needed for each particle density and imaging resolution combination. For the spot areas of respectively 0.01 μm^2 or 0.12 μm^2 we obtain λ of 0.2 and 2.4 respectively by multiplying with the particle density. From Figure 4.3 **A** and **B** it is immediately clear that the intensity distribution obtained from simulated images with randomly distributed particles differ from the calculated Poisson distributions. These results indicate that a Poisson distribution based on particle density and imaging resolution does not describe the spot intensity distributions obtained from the simulated fluorescent images. This difference is due to the analysis method where we specifically select the bright areas, whereas Poisson gives the chance of finding 1,2,. particles per sampling area at a random position in the image.

On the other hand, from the intensity distributions it is clear that a limited spatial resolution combined with a high packing density, can be misinterpreted as clustering. In Figure 4.3 **B** the spot distribution peaks at 4 particles per spot, while in fact particles were randomly distributed as monomers. This example demonstrates the importance of comparing experimentally obtained fluorescent spot intensity distributions with random particle distributions at relevant particle densities and imaging resolution. To illustrate the effect of aggregation on the fluorescent spot intensity distribution, Figure 4.3 **C** shows the distribution obtained after analysis of a simulated image containing real clusters. The simulated image was obtained using similar settings as for Figure 4.1 **B**, that is $D =$ 20 particles/μm^2 and $R = 20$ nm, but where we assigned 70 % of the particles to clusters containing 4 ± 2 particles. The clustered particle distribution clearly deviates from the fluorescent spot distribution for randomly distributed monomers in Figure 4.3 **A**.

4.3 Comparing experimental data with computer simulations

In the previous chapter we showed the intensity distribution of CTxB, fluorescently labeled with Alexa-647, as obtained on THP1 cells in solution and measured with NSOM. Furthermore, we could also identify individual fluorescent CTxB molecules on the glass surface next to the cell area. Here we will compare the experimental intensity distribution of CTxB both on glass and on THP1 cells with spot intensity distributions obtained from simulated fluorescence images to draw conclusions on the degree of randomness and clustering. The particle den-

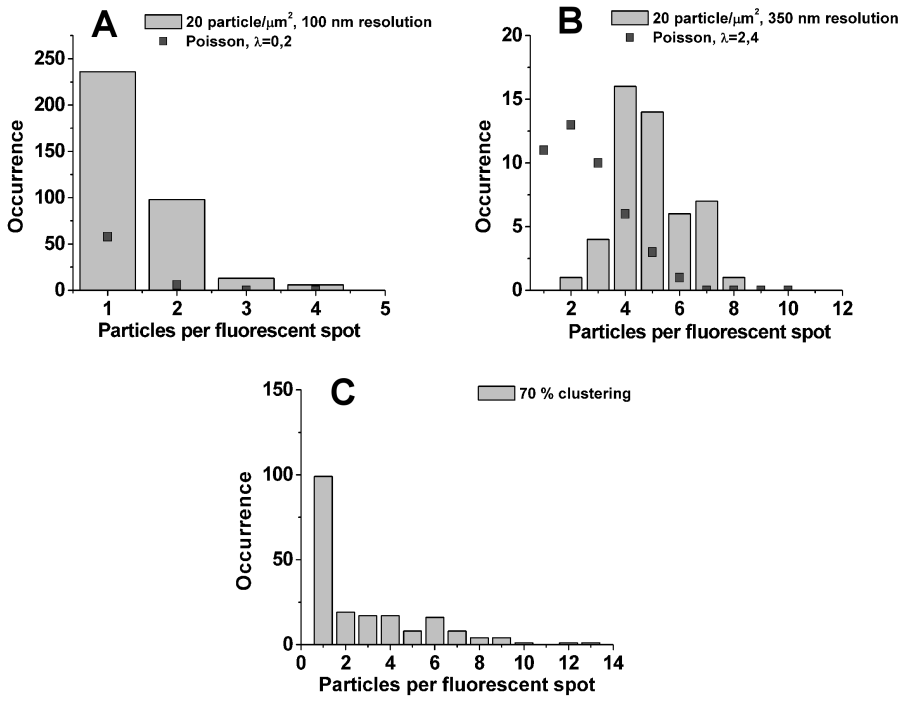

Figure 4.3: Particle per fluorescent spot distribution and Poisson distribution for simulated fluorescence images at packing density of $D = 20$ particle/μm^2. The resolution in the simulated images was 100 nm for (**A**) and (**C**) and 350 nm for (**B**). The values of λ to calculate the corresponding Poisson distribution are respectively 0.2 and 2.4 for the distributions in (**A**) and (**B**). The corresponding value for the Poisson distribution is indicated by the squares. In (**C**) the fluorescent spot intensity distribution obtained from a simulation with 70% clusters containing 4±2 particles is shown.

sity on glass is estimated by dividing the total background subtracted intensity by the average intensity of an individual CTxB molecule. This yields the number of CTxB molecules present in the imaging area of 5x5 μm^2 and thus the particle density. The experimentally obtained CTxB density on glass was $\sim$ 10 CTxB/μm^2. Using this particle density in combination with an imaging resolution of 100 nm results in the simulated fluorescence image shown in Figure 4.4 **A**. Although the particle density in the simulation corresponds to the particle density derived from the experiments, the simulation does not appear to reproduce the intensity differences found in the experimentally obtained images, as the one shown in Figure 4.4 **C**. On the other hand, in the previous chapter it was also shown that the

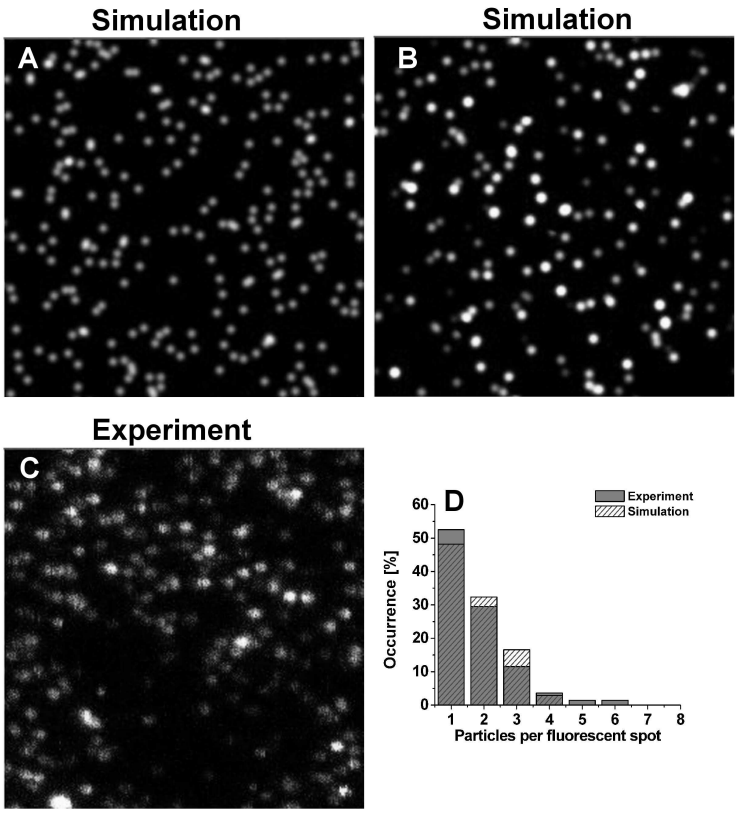

Figure 4.4: Simulated and experimentally obtained fluorescent images of CTxB distribution on glass reveal a random particle distribution. Simulation settings for (**A**) are: A = 5x5 μm^2, P_l = 256 pixels, I = 1000 counts and I_d = 0 counts, D = 10 particles/μm^2 and R = 100 nm. The simulated image in (**B**) is obtained with similar settings except for I_d which is set to 1000 counts. The experimentally obtained fluorescence image of CTxB-Alexa647 molecules on glass (**C**) is obtained with a NSOM probe with an aperture size of $\sim$ 100 nm and the image area is 5x5 μm^2 with 256 pixels per line. The spot intensity distributions corresponding to image (**B**) and (**C**) are shown in (**D**).

fluorescent spot intensity distribution of individual CTxB molecules peaked at 16 kCounts/s, with $\pm$ 14 kCounts/s variety in CTxB spot intensity. This variation is most probably related to a distribution of chromophores actually labeling the CTxB molecule. In fact in the previous chapter we derived a chromophore labeling efficiency of 9 $\pm$ 9. To incorporate this variability in the simulations a standard deviation (I_d =1000 counts), equal to the average particle intensity was

used. The outcome of this simulation is shown in Figure 4.4 **B**. Indeed, both images (Figure 4.4 **B** and **C**) are now very similar. The distributions quantifying the apparent number of particles per spot in the simulation and experiment are shown in Figure 4.4 **D**. Here the relative number of particles per spot is obtained by dividing average spot intensity by the average intensity of a single CTxB. The brightness distributions of the simulated image and the experimental obtained image agree exceedingly well with each other, except from a small deviation on the occurrence of larger numbers of particles per spot. This might be due to a mild aggregation during the experiments. It is clear that indeed most CTxB molecules are randomly distributed on the glass as anticipated. Importantly, the variety in spot intensity has been a crucial parameter to take into account in order to correctly reproduce the experimentally obtained fluorescence image.

Now we turn to the CTxB on THP1 cells. Are the intensity variations the product of a random particle distribution imaged at an unfavorable particle density and resolution combination? Do our observations reveal true clustering? To simulate fluorescence images of randomly distributed CTxB molecules on THP1 cells the only unknown parameter is the particle density on the cell. This density can be estimated by comparing the total intensity in the cell area with the total intensity on the glass. The difference is roughly a factor of 10, indicating that the particle density on the cell surface is a factor of 10 higher. Therefore a particle density of 100 CTxB/μm^2 has been used in the simulation. The obtained simulated fluorescence image is shown in Figure 4.5 **A**, while a typical NSOM measurement is shown in Figure 4.5 **B**. Surprisingly, both images appear rather similar suggesting that the particles are randomly distributed. Both the distributions quantifying the apparent number of particles per spot in simulation and experiment are shown in Figure 4.5 **C**. Here the number of particles per spot is again obtained by dividing average spot intensity by the average intensity of a single CTxB. From Figure 4.5 **C** it is clear that the intensity distribution obtained from the experimental data is largely shifted towards more particles per spot. Furthermore, the distribution has very few occurrences for low number of particles per spot, indicating that all CTxB molecules are incorporated in small clusters. On average these clusters appear to contain ~ 9 particles. Furthermore, the size distribution can be fitted to a Poisson distribution (λ=8.7, χ^2=5), indicating that the content of the clusters is random. The measured distribution can be reproduced using a simulation with 100% clustering and an average number of particles per cluster of 6 ± 6. This indicates that the CTxB on THP1 cells contain on average 6 CTxB molecules.

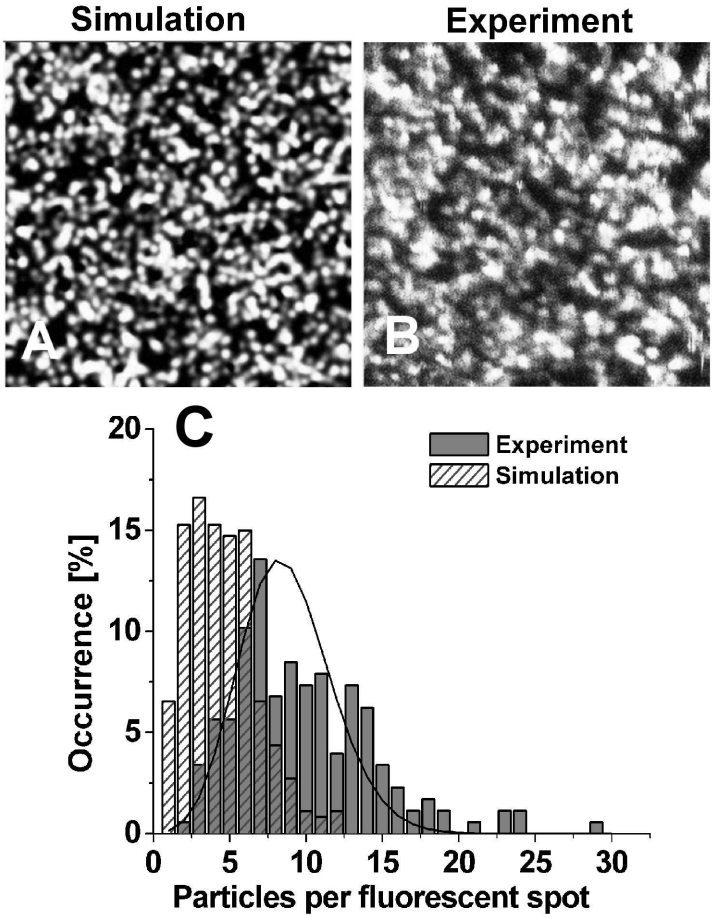

Figure 4.5: Simulated and experimentally obtained fluorescent images of CTxB on a THP1 cell reveal true clustering. Simulation settings for (**A**) are: A = 5x5 μm^2, P_l = 256 pixels, I = 1000 counts and I_d = 1000 counts, D = 100 particles/μm^2 and R = 100 nm. The experimentally obtained fluorescence image of CTxB-Alexa647 molecules on THP1 (**B**) is obtained with an NSOM probe with an aperture size of $\sim$ 100 nm. Image area is 5x5 μm^2 with 256 pixels per line. The spot intensity distributions corresponding to image (**A**) and (**B**) are shown in (**C**).

4.4 Discussion

Insight in aggregation of plasma membrane components is important in order to understand cell function. Fluorescent spot intensity analysis can reveal information on the aggregation state of proteins and lipids, but especially for small aggregates, this information should be thoroughly investigated due to the finite optical resolution used in most fluorescence-based experiments. Since a fluorescence image is always the result of the convolution between the fluorophore and the excitation profile of the illumination source, a high particle density in combination with an unfavorable imaging resolution can erroneously indicate particle clustering. Indeed, in crowded samples several particles might be present within the excitation volume, without real association between the particles. In literature several papers can be found where clustering is identified on the basis of fluorescence differences in confocal images [38, 133, 134]. However, similar images can in principle also originate from randomly distributed individual particles. Therefore true clustering can only be determined from fluorescence images after careful comparison to simulations of random particle distributions at the same particle density.

We have generated fluorescence images with random particle organization, for which experimental parameters, like particle density and imaging resolution have been used as input. Point pattern images generated in this manner are perfectly described by the Poisson distribution, validating the randomness of the simulation. However, the distribution deviates from Poisson as the apparent particle size (as a result of the finite imaging resolution) approaches the box size used to obtain the Poisson distribution. Therefore, point pattern analysis methods as often used for TEM images are less suited for fluorescence images in which particles have a finite size due to the convolution with the excitation source. We and others [91, 120] commonly use fluorescent spot intensity distributions derived from the fluorescent images to enquire on the stoichiometry of the observed spots after relating their intensity to those of individual molecules. However, we have demonstrated in this chapter that fluorescent spot intensity distributions can not be directly compared to a Poisson distribution, since the first is obtained by exclusively selecting the bright areas in the image while the latter assumes each area to be selected at random. Therefore, to assess the degree of true clustering, the experimentally obtained fluorescent spot intensity distributions need to be compared with distributions from simulations using random particle positions and with particle density and resolution settings as dictated by the experiment. Even if individual spots can no longer be discriminated, true clustering does definitely result in a larger number of particles per spot as compared to a random particle distribution. Information regarding clustering can also be obtained via FRET

experiments [42, 128]. However no information on surface organization and/or stoichiometry of associated proteins can be obtained using FRET. The added value of NSOM is that separate individual clusters can be detected in densely packed membranes allowing quantification of cluster content [91]. This can only be achieved using a high resolution technique since at particle densities exceeding 10 particles/ μm^2 confocal resolution is not sufficient to resolve individual particles. Since the expression level of most proteins exceeds this density the use of NSOM is necessary to retrieve information on cluster content.

There are several experimental requirements to perform the analysis described in this chapter. First, it is important to know the average intensity of individual fluorescent particles, the standard deviation in this intensity, and the density of fluorescent particles in the cell membrane. Therefore the imaging system needs to be sensitive enough to discriminate individual particles. For biological applications the fluorescent particles should be as small as possible to minimize labeling artifacts. If fluorescent antibodies or fluorescent proteins are used, single molecule detection sensitivity is required to discriminate individual particles. Another important issue is the dynamic range of the detector since it is crucial to have ample sensitivity to detect both individual particles and the intense fluorescent signals from heavily packed cell membranes without overloading the detector. Furthermore, to correctly relate brightness to the number of particles it is also crucial to work with a detector that has a linear response to the signal over the whole range.

During our analysis we have assumed a linear dependence between fluorescence intensity and number of fluorophores in the excitation volume. In reality the absolute accuracy with which the spot intensity can be related to the number of fluorophores drops with increasing spot intensity, due to photon statistics. Moreover, in heavily packed systems quenching between the individual fluorophores can occur, leading to an underestimation of the total number of particles and the number of particles in a fluorescent spot. Since the simulated particle density is based on the observed cell intensity and therefore the apparent number of fluorescent particles in the experiment, the effect of quenching on the apparent clustering is reduced. However, since especially the fluorophores attached to particles in a cluster are sensitive to quenching it might lead to an underestimation of the extent of clustering. On the other hand, the variability in the fluorescence of individual CTxB might also result from quenching between the close packed Alexa647 fluorophores labeling the CTxB molecules. Since we take this variability into account in the simulations, together with the small size of the clusters one could also argue that effects of quenching play a minor role. Another issue we did not take into account during our simulations is the 3D shape of the membrane.

Ruffles and/or membrane folding increase the effective membrane area, resulting in return in an overestimation of the particle density used in our simulations. Since this yields higher particle per spot values in our simulations we probably overestimate the contribution of apparent clustering.

As a whole, the most remarkable finding in this chapter is that the large majority of CTxB molecules are incorporated in small clusters containing on average 6 CTxB per cluster. Assuming a similar CTxB to GM1 ratio as in the previous chapter this indicates that the underlying GM1 domains contain on average at least 30 GM1 lipids. Moreover the content or number of CTxB molecules binding to these clusters appears to be random. This provides direct evidence that lipid raft precursors with nanometer dimensions do indeed exist in the plasma membrane of cells. Our results are fully in line with recent findings of Sharma and co-workers and Plowman and co-workers who found similar nanodomains of GPI-anchored proteins in cell membranes using respectively FRET and TEM [6, 113].

4.5 Conclusion

In this chapter we demonstrated that experimentally obtained fluorescence images can be compared to simulated images of randomly distributed particles at densities related to experimental conditions. Important parameters for the simulation are particle density, imaging resolution and the standard deviation in the average intensity expected for a single particle. These parameters can be experimentally determined using a fluorescence microscope equipped with single molecule detection sensitivity. Using the intensity distribution of CTxB randomly organized on the glass cover slip, the variety in spot intensity could be estimated in order to correctly reproduce the experimentally obtained fluorescence image. The spot intensity distribution for CTxB on the cell was clearly shifted towards higher particles per spot with respect to the random particle simulation. Furthermore, the distribution had very few occurrences for low number of particles per spot, indicating that most CTxB molecules are incorporated in small clusters. The corrected average cluster size is 6 CTxB per cluster and the shape of the measured intensity distribution indicates a random distribution of cluster sizes.

This provides direct evidence that nanometer sized lipid domains (lipid raft pre-cursors) indeed exist in the plasma membrane of cells. The strength of our method relies on the combination of high resolution microscopy with computer simulations to unequivocally assess the nano-scale spatial organization of components at the cell surface. Comparison of fluorescent spot intensity distributions obtained from simulations to experimentally obtained distributions will further unravel protein organization in different cell types, which is the topic of the following chapter.

Chapter 5

Nanoscale compartmentalization of the cell membrane

How are proteins organized in the cell plasma membrane? An important question since receptor clustering into micro-domains is acknowledged as an important mechanism to regulate cellular functions. Here we have applied near-field scanning optical microscopy (NSOM) on cells in liquid to map the organization of different protein receptors on two different cell types with a spatial resolution better than 100 nm. Experiments were combined with simulations using experimentally obtained parameters, i.e. receptor density and fluorescence intensity, to assess the degree of clustering. From two non raft markers investigated, the transferrin receptor CD71 appears randomly organized on THP1 cells (monocytic cell line), while CD46 forms nano-domains on immature dendritic cells (imDC). Remarkably, we also found that the GPI anchored protein CD55, a commonly used raft marker, does not cluster on both imDC and THP1 cells, but rather organizes in a random fashion. These results demonstrate that classification as 'lipid raft associated' does not give a priori information on surface arrangement, i.e. lipid raft partitioning does not necessarily imply clustering and clustering is not per se maintained by lipid rafts. Furthermore we have mapped the organization of the C-type lectin DC-SIGN on imDC and the integrin LFA-1 on THP1 cells. Our results on cells in liquid confirm clustering of these proteins at the nanometer scale, consistent with previous TEM experiments on dried cells. Our findings favor a model where not lipid raft partitioning but other mechanisms like protein-protein interactions or the cytoskeleton determine the distribution of proteins as either monomers or small clusters.

5.1 Introduction

In the previous chapter we have shown that simulations of random protein organization, based on experimentally obtained density, resolution and single particle fluorescence intensity can be used to discriminate true clustering from random surface organization. Indeed, we revealed true nano-clustering of the lipid GM1 on the cell membrane of THP-1 cells. Besides lipids, proteins form an important constituent of the plasma membrane. Several proteins have been shown to organize into supramolecular clusters or microdomains [2, 3], influencing and regulating cellular functions [15]. The direct visualization of small domains, accommodating only a few proteins is not possible using conventional microscopy techniques, since at high protein packing densities most of the cell surface appears to be uniformly covered due to the limited optical resolution. To directly visualize smaller nanometer sized clusters, researchers have relied on immuno gold labeling in combination with transmission electron microscopy. These studies have revealed nanometer sized domains for several proteins, for example DC-SIGN on imDC [59], IL-2 receptor α-subunit on T cells [133], Ras on inner plasma membrane sheets [78], LAT on mast cell membrane sheets [135] and hemagglutinin on fibroblasts [77]. In the previous chapters we already demonstrated that near-field scanning optical microscopy (NSOM) breaks the diffraction limit of light and allows the direct observation of nanometer sized protein and lipid domains. In contrast to TEM, NSOM in liquid conditions can be applied to intact cells in liquid preserving the cell membrane architecture. Here we combine distributions obtained from high resolution optical imaging on intact cells in liquid with computational modeling of fluorescent spot intensity distributions to investigate protein organization and compartmentalization of the cell membrane at the nanometer level.

We have focussed on the organization of DC-SIGN, CD46 and CD55 on imDC and CD71, CD55 and LFA-1 on THP-1 cells (a monocytic cell line). The relevance of these proteins in the context of our research is their potential partitioning into lipid platforms like lipid rafts. Indeed, lipid rafts are thought to act as platforms where specific membrane proteins can segregate [23] facilitating protein domain formation. DC-SIGN (CD209) is a C-type lectin specifically expressed by DCs. Using TEM and NSOM on dried cells, we have demonstrated that DC-SIGN is organized in microdomains on imDC. Furthermore, we have also shown that these microdomains enhance the virus binding capacity of imDC. Based on several well-established raft analysis techniques, it appears that DC-SIGN mostly resides in lipid rafts [59]. CD46, or membrane co-factor, is a transmembrane protein, recently identified as a cellular attachment receptor for most group B adenoviruses [136] and it is a non-raft associated protein on imDCs [137]. To the

best of our knowledge, virtually nothing is known on the spatial organization of CD46. CD55, or decay-accelerating factor, is a GPI-anchored protein, commonly used as a marker for lipid rafts [138]. Although the surface organization of CD55 has not been reported yet, other GPI-anchored proteins like Thy-1 were observed to be mainly distributed as monomers or small clusters (binding 2-10 gold beads) using TEM [45]. Using FRET, 20-40 % of GPI anchored protein appeared to be organized in clusters containing upto 4 proteins whereas the rest was distributed as monomers [6]. Similar results have been obtained in another FRET study on the GPI-anchored protein 5' nucleotidase on MDCK cells [139]. CD71 or transferrin receptor, is commonly recognized as a non-raft marker [63]. Its surface organization has been investigated using confocal microscopy and 300 nm sized domains on human T cells have been reported [133]. LFA-1 is a leukocyte specific integrin, for which we recently demonstrated an organization in nanometric domains on monocytes using TEM on whole mount cells [76]. Co-patching experiments using confocal fluorescence microscopy revealed that LFA-1 heavily co-localizes with GM-1 on monocytes, indicating LFA-1 partitioning into lipid rafts [76].

In this chapter we demonstrate different levels of surface organization for this group of proteins. Proteins are either organized as monomers or in small domains containing a handful of proteins and below 100 nm in size. This small scale organization might precede the formation of larger protein domains upon ligand binding. Moreover the spatial organization of proteins appears to be independent on their classification to partition in lipid rafts by well established biochemical methods. This suggests that other mechanisms, like protein-protein interactions or interactions with the cytoskeleton play a role in the formation and/or sustenance of protein domains.

5.2 Materials and Methods

5.2.1 Sample preparation for fluorescence microscopy

Monocytes were obtained from buffy coats of healthy individuals and were purified using Ficoll density centrifugation. ImDCs were obtained as reported elsewhere [66]. In brief, DCs were cultured from monocytes in presence of IL-4 and GM-CSF (500 and 800 U/ml, respectively) for six days to obtain imDCs.

For NSOM/confocal microscopy, cells were stretched on poly-l-lysine coated coverslips for 45 minutes at 37^{o}C and fixed using 1% PFA in PBS for 20 minutes at room temperature, followed by two PBS washing steps and blocking for 1 hour. The proteins of interest were then labeled at room temperature with

either 10 μg/ml anti-DC-SIGN antibody, anti-CD55 antibody or anti-CD46 antibody. Secondary staining was performed with Alexa 488-conjugated goat anti-mouse IgG. Finally the samples were washed three times with PBS. Wet samples were stored in PBS containing 1% PFA until use. The THP1 cells were cultured in RPMI 1640 dutch modification medium supplemented with 10% Fetal Calf Serum and antibiotic-antimycotic from Gibco. After a similar procedure as for imDC the proteins of interest are labeled with either 10μg/ml anti-LFA1 (TS2/4) antibody, anti-CD55 antibody or anti-CD71 (transferrin receptor) antibody. Secondary staining was performed with Alexa488-conjugated goat anti-mouse IgG and stored similar to imDC samples. Isotype specific controls were always included.

5.2.2 Confocal and near-field fluorescence microscopy

For the experiments described in this chapter we used a home built confocal/NSOM microscope optimized for single molecule detection. All experiments were performed in liquid, using the diving bell concept for NSOM inspection as described in Chapter 2. The proteins of interest are labeled via an Alexa-488 conjugated antibody (see Sample preparation) and are excited using the 488nm line of an argon/krypton-ion laser (CW, Spectra-Physics). In confocal mode, circularly polarized excitation light is reflected by a dichrioc mirror (Omega Optical Inc.) and focused onto the sample using an oil immersion objective (60x, 1.4 NA or 100x, 1.3 NA). In the NSOM mode, the sample is excited via an aperture type fiber probe. The emitted fluorescence is collected and spectrally separated from the excitation light using appropriate longpass filters (Omega Optical Inc.) and detected using a photon counting avalanche photodiode (APD, SPMC-100,EG&G, Quebec).

5.2.3 Electron microscopy

Electron microscopy images obtained for DC-SIGN and CD55 on imDC and LFA-1 on monocytes are used as a comparison to our near-field fluorescence images. ImDCs or monocytes were allowed to spread on glass coverslips covered by a thin layer of fibronectin or poly-l-lysine coated formvar for 1 h at 37^o C, washed to remove unbound cells and immediately fixed with 1% paraformaldehyde (PFA) for 15 minutes. After two washing steps with phosphate buffered saline (PBS) and a subsequent incubation (60 minutes at room temperature) with I-buffer (PBS, 0.1% glycine, 1% bovine serum albumin (BSA), and 0.25 % gelatin) to reduce aspecific background, the specimens were incubated for 30 min with the primary antibodies (mAb AZN-D1 for DC-SIGN [66]), TS2/4 for LFA-1

and 143-30 for CD55 (CLB)) in the I-buffer on ice, rinsed in PBS, and fixed in 1% PFA and 0.1% gluteraldehyde for 15 min. After two washing steps with PBS and a block in I-buffer, the samples were incubated with rabbit anti-mouse IgG (to detect mAb) for 30 minutes on ice. A final incubation with 10-nm-diameter gold-labeled protein A (to detect polyclonal antibodies) was performed, followed by a final fixation in 1% gluteraldehyde in phosphate buffer for 20 minutes at room temperature. The specimens were dehydrated by sequential passage through 30, 50, 70, 90 % and absolute ethanol. Next, the ethanol was substituted by liquid CO_2, and the samples were critical point dried. The formvar films were transferred from the glass onto copper grids, and the specimens were observed in a transmission electron microscope (model 1010; JEOL), operating at 60-90kV. Gold particles were detected on the periphery and thinner parts of cells, where a good contrast could be achieved. Since imDCs and monocytes spread extensively on the support, the membrane area available for analysis represented up to 60-70% of the whole cell surface.

5.2.4 Image analysis

To obtain fluorescence brightness distributions, fluorescence images are analyzed using a custom-written program based on LabView (National Instruments, TX). The number of molecules in each fluorescent spot is related to the brightness. The brightness is determined by adding all background subtracted photons within the full width at half maximum (FWHM) of the peak intensity and normalized with respect to excitation intensity. The distributions of number of particles per spot have been obtained in a slightly different manner. Here the simulated and experimentally obtained fluorescence images are processed using the same custom written LabView analysis program described in Chapter 3. Briefly, here a spot is defined using a circle with radius r, where r is chosen such that the spot diameter corresponds to the imaging resolution. Fixed values of r are needed in order to make a direct comparison between simulations and experiments possible, but since most fluorescent spots were limited in size by the NSOM probe diameter the fixed value for r yields similar results as the brightness analysis. By adding all pixel intensities and dividing by the total number of pixels in the spot we obtain an average fluorescent spot intensity. The number of particles in the spot (N) can be directly related to the average fluorescent spot intensity (I_{av}) by using the intensity obtained for an individual particle. For TEM the digital images were processed by custom written software based on LabView. The distribution pattern of DC-SIGN, CD55 and LFA-1 (i.e.: the degree of clustering) was analyzed by counting the number of gold particles found on the plasma membrane in a

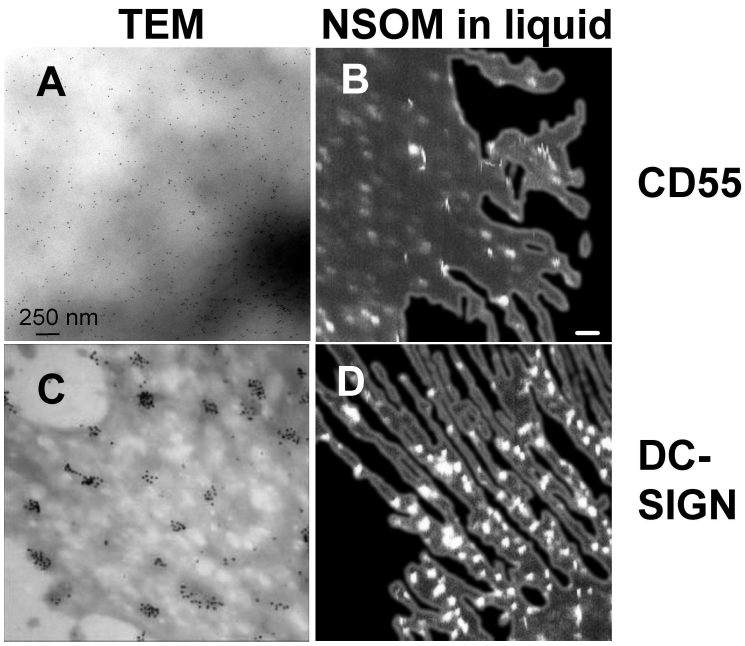

Figure 5.1: High resolution imaging of protein distribution on imDC with TEM and NSOM. (**A** and **C**) TEM images of the distribution of CD55 and DC-SIGN labeled using 10 nm gold particles. (**B** and **D**) Near-field optical fluorescence images of imDCs in liquid showing the distribution of CD55 and DC-SIGN, respectively fluorescently labeled via Alexa488 conjugated antibodies. Excitation with a 488 nm laser line using a probe of $\sim$ 100 nm in diameter and scalebar is 500 nm. For direct comparison of the fluorescent images, the intensities are normalized with respect to scan speed and excitation conditions. The topography information was used to plot only fluorescence information corresponding to the cell area.

semi-automatic fashion. Subsequently, coordinates were assigned to the observed beads and interparticle distance statistics were obtained using a nearest neighbor distance algorithm. Clusters were defined when gold particles were less than a set distance apart from a neighboring particle.

5.3 Results

5.3.1 Protein organization on imDC

Previous studies on dried imDCs using both TEM and NSOM revealed an organization of DC-SIGN in microdomains [59, 91]. To date these high resolution studies could only be performed on dried samples, where drying procedures are likely to influence the apparent surface distribution. Using the divingbell NSOM these studies can be extended to cells in liquid and it is therefore important to investigate the organization of DC-SIGN on imDC in liquid. Besides DC-SIGN, the surface organization of CD55 and CD46 has been also investigated. From biochemical experiments it is known that these proteins partition in different membrane environments, most probably influencing their surface organization. In Figure 5.1 **A** and **C**, TEM images mapping the surface organization of CD55 and DC-SIGN on dried imDC are shown. The corresponding near-field fluorescence images of CD55 and DC-SIGN on imDCs in liquid are presented in Figure 5.1 **B** and **D**. In here, the simultaneously obtained topographic information is used to show specifically fluorescence information corresponding to the cell surface. From the NSOM images it is clear that the fluorescent spots in the DC-SIGN image appear much brighter than those spots in the CD55 image indicating a higher local concentration of DC-SIGN as compared to CD55. Comparison with TEM in Figure 5.1 **A** and **C** indeed confirms that DC-SIGN is organized into small domains, while the CD55 distribution is more homogeneous over the imDC surface. Strikingly, both proteins are associated to lipid rafts, while their surface organization appears to be totally different.

To analyze the data in a more quantitative manner we processed the images using a custom-written analysis program based on LabView. For NSOM images, the number of molecules in each fluorescent spot is related to its brightness. This brightness is determined by adding all background subtracted photons within the full width at half maximum (FWHM) of the peak intensity and normalized with respect to excitation intensity. The resulting distributions for CD55 and DC-SIGN are shown in Figure 5.2 **A** and **C**. Both the brightness distribution for CD55 and DC-SIGN peak around 15 kCounts. However, in contrast to CD55, the DC-SIGN distribution has a long tail extending up to 170 kCounts per spot, clearly reflecting a difference in surface organization between both proteins and again indicating DC-SIGN clustering.

The surface distribution of the non raftmarker CD46 was investigated on imDC using NSOM in liquid in a similar manner. A representative NSOM fluorescence image of CD46 on an imDC is shown in Figure 5.3 **A**, together with the fluorescence intensity distribution shown in Figure 5.3 **B**. The bright spots

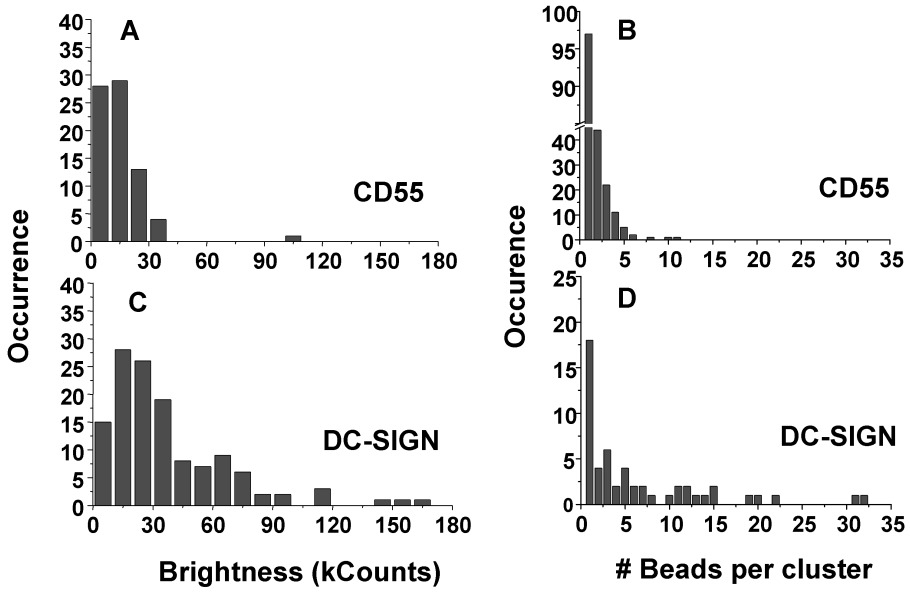

Figure 5.2: Quantitative representation of NSOM and TEM images. (**A** and **C**) Intensity distribution derived from near-field optical fluorescence images of imDCs in liquid, for CD55 and DC-SIGN respectively. (**B** and **D**) Distribution of number of gold beads per cluster for respectively CD55 and DC-SIGN. Clusters were defined when gold particles were < 70 nm apart from a neighboring particle.

suggest a high local concentration of CD46. Indeed, the width of the CD46 distribution is very similar to that obtained for DC-SIGN confirming that CD46 is also organized in small domains. Remarkably, while CD46 being a non-raft associated protein shows a clustered type of surface distribution, CD55, a raft associated protein is mainly present as a monomer.

In the case of the TEM images the number of gold particles per cluster was determined by direct counting. A cluster was defined when gold particles were < 70 nm apart from a neighboring particle. The results are presented in histograms in Figure 5.2 **B** and **D** for CD55 and DC-SIGN respectively. In total, 260 gold particles were counted, both from CD55 and DC-SIGN TEM images. A large fraction (36%) of the gold labeled CD55 particles are distributed as individuals on the surface. In contrast, the DC-SIGN histogram is much broader with the majority of particles being located in clusters containing multiple beads, while only 7% of the gold particles appear as individuals. The distributions obtained with both NSOM and TEM are remarkably similar in shape, indicating

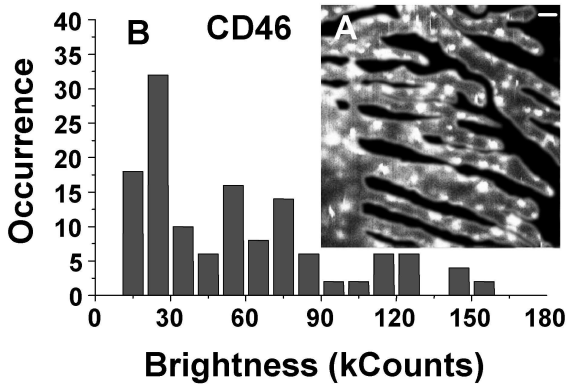

Figure 5.3: Surface distribution of CD46 on imDC imaged using near-field fluorescence in (**A**), together with the corresponding intensity distribution in (**B**).

that complementary information is obtained in both cases. However, NSOM allows similar level of quantitative analysis on cells in liquid in contrast to TEM which is only capable of imaging in dry conditions.

5.3.2 Computational predictions to contrast experimental data on imDC

In the previous chapter it was already demonstrated that a high protein packing density in combination with a finite spatial resolution can result in apparent clustering. Therefore, to discriminate apparent from true clustering we compare the fluorescent spot intensity distributions obtained from NSOM images of CD55, DC-SIGN and CD46 on imDC to distributions obtained from simulations of randomly distributed particles at the experimentally obtained particle densities. As already mentioned in the Materials and Methods section, the total particle density on the surface can be retrieved by relating the total intensity of each spot to the intensity of each particle, which in our case corresponds to an individual fluorescent antibody. The intensity of a single particle is obtained using the single antibodies on the glass coverslip beside the cell surface. The intensity of a single particle can vary due to excitation conditions in combination with differences in labeling efficiencies of Alexa dyes binding to the secondary antibodies. The standard deviation in intensity is obtained from the width in the intensity distribution for the single antibodies. Thus, for CD55, DC-SIGN and CD46 we found intensities of respectively 25±10 kCounts/s, 3.7±0.6 kCounts/s

and 8±2 kCounts/s. The density of particles on the cell surface is then obtained from the NSOM images by adding all spot intensities and dividing by the average particle intensity and surface area. This results in particle densities for CD55, DC-SIGN and CD46 of respectively 3±1 particles/μm^2, 14±4 particles/μm^2 and 13±3 particles/μm^2. The simulated images have a similar size and number of pixels per images as the experimental obtained images. Since for all experiments the size of the NSOM probe was approximately 100 nm, we take this value as the spatial resolution used in the simulations. All images were analyzed in a similar fashion as described in the Materials and Methods section. The intensity distribution was converted to a particle per spot distribution using the average intensity of a single particle. In Figure 5.4 the particle per spot distributions for both experiment and simulation are presented for the three different proteins. From Figure 5.4 it is immediately clear that the organization of DC-SIGN and CD46 can not be described using a random particle distribution. Assuming a one-to-one labeling ratio, about 75% of the DC-SIGN is organized in clusters accommodating 3 to 12 DC-SIGN proteins. For CD46, 55% of the molecules are organized in clusters accommodating a similar amount of proteins. In contrast, the CD55 distribution can be well described using a random particle distribution indicating that most of the CD55 proteins are distributed as single entities. The slight deviation from the simulated random distribution suggests that about 15% of the molecules are present in small clusters containing 4 proteins at most. On the other hand these clusters might not be significant since the uncertainty in particle density is $\sim$ 35 %.

5.3.3 Mapping protein organization on THP1 cells

We also investigated the surface distribution of three different proteins on the membrane of THP1, a cell line closely related to human monocytes, the precursors of imDC. Two of the proteins the GPI-anchor CD55 and the integrin LFA-1, have been shown to be associated to lipid rafts on monocytes [76]. The other investigated protein is the non raft associated transferrin receptor CD71. Prior to high resolution NSOM imaging, cells were first inspected using confocal microscopy. Representative images for each protein are presented in Figure 5.5. Interestingly from the confocal images (the most left column) it is immediately clear that LFA-1 expression is larger with respect to CD55 and CD71 expression on THP1 cells. The confocal zoom-in in Figure 5.5 **B** demonstrates clustering of LFA-1 since well defined intense spots can be discriminated. A further zoom in using NSOM Figure 5.5 **C** enhances the resolution to $\sim$ 100 nm where most of the domains are now spatially separated. Some spots appear to be slightly elongated

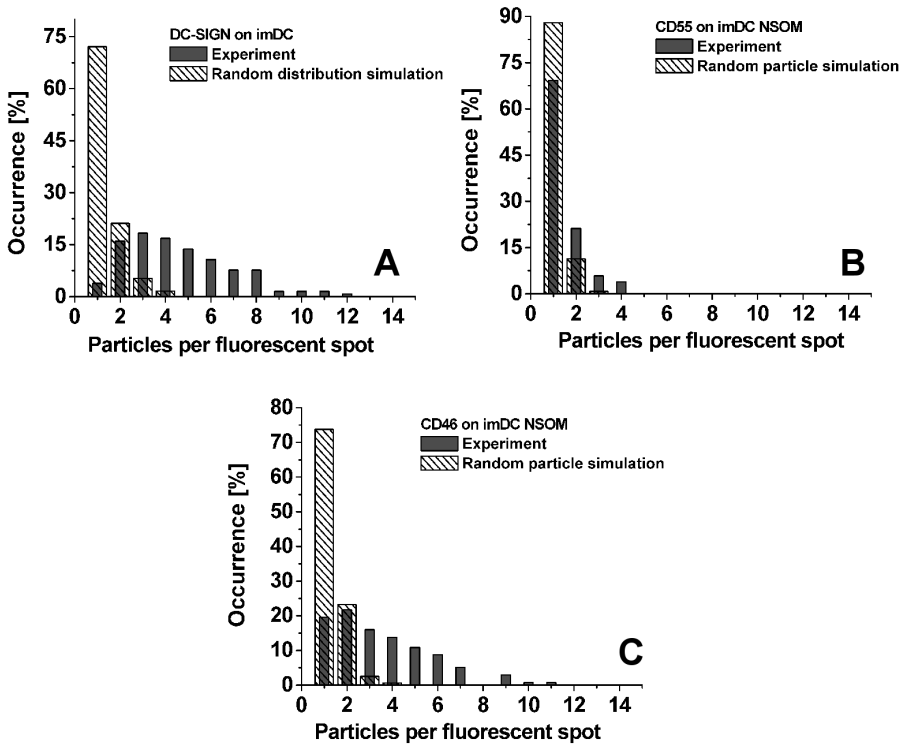

Figure 5.4: Simulations reveal true clustering of DC-SIGN and CD46 on the surface of imDC while CD55 is mainly distributed as monomers. Quantitative representation of the number of fluorescent antibodies present per spot in the measured (gray bars) and the simulated (striped bars) fluorescence images for DC-SIGN (**A**), CD55 (**B**) and CD46 (**C**). The relative occurrence on the y-axis is obtained through the total number of spots retrieved from the images. Relating the spot intensities to the intensity of the individual antibodies yielded the number of particles per spot.

along the vertical direction due to weak tip sample interactions. For CD55 both confocal and NSOM images (Figure 5.5 **E** and **F**) reveal similar detail, indicating that indeed this protein is expressed at lower density. In fact, individual spots are already discriminated by confocal despite the lower spatial resolution ($\sim$ 240 nm). For CD71 the confocal zoom-in is shown in Figure 5.5 **H**. Based on the differences in intensity in the confocal images, the expression level of CD71 is about a factor 3 higher than that of CD55. This explains the more crowded image in Figure 5.5 **H** where hardly any individual spot can be discriminated. Benefiting from the superior resolution of NSOM clear individual spots can resolved in

Figure 5.5 **I**. The intensity of the individual CD71 spots is comparable to those of CD55, indicating that both proteins are probably distributed as monomers. Altogether, these images are a first indication that LFA-1 is organized in small domains whereas CD55 and CD71 are distributed as single entities on THP1 cells.

5.3.4 Computational predictions to contrast experimental data on THP1

To assess the degree of true clustering we compare the experimental results for protein distribution on THP1 cells with simulations in a similar manner as for the imDC. For the NSOM images of CD55 and CD71 the intensity of an individual antibody is obtained from the distribution of individual fluorescent spots beside the cells on the glass coverslip. This results in 2.4±0.8 kCounts/s for CD55 and 4±1 kCount/s for CD71. Using the total fluorescent spot intensity on the cell and dividing through cell area and single particle intensity yields a particle density of 3±1 particles/μm^2 for CD55 and a particle density of 9±2 particles/μm^2 for CD71. For the NSOM LFA-1 images we hardly find any single particle on the glass, probably due to the low excitation intensity used in these experiments.

In the previous chapter we demonstrated that the true aggregation state of a protein can be also retrieved from confocal images as long as the intensity of the individual particles is known. We determine the brightness of an individual antibody from the distribution of individual fluorescent spots on the glass in the confocal image yielding an intensity of 45±26 kCounts/s. Relating this value to the total LFA-1 intensity, this results in a particle density of 17±10 particles/μm^2. For all experiments the size of the NSOM probe was approximately 100 nm, dictating the resolution settings used in the simulations for the NSOM images. For the simulations of the confocal images the resolution is set to 240 nm. All images were analyzed in a similar fashion as described in the materials and methods section. The intensity distribution was converted to a particle per spot distribution using the average intensity of a single particle. In Figure 5.6 the particle per spot distributions for both experiment and simulation are presented for the three different proteins. From Figure 5.6 **A** it is immediately clear that the organization of LFA-1 can not be described using a random particle distribution. The experimental distribution is clearly right shifted with respect to the distribution for random organization. Thus the number of LFA-1 proteins in a fluorescent spot is higher than expected based on random distribution and therefore the shifted distribution is indicating clustering of LFA-1 on the THP1 cells. Subtracting the overlap with the random particle simulation from the experimentally obtained

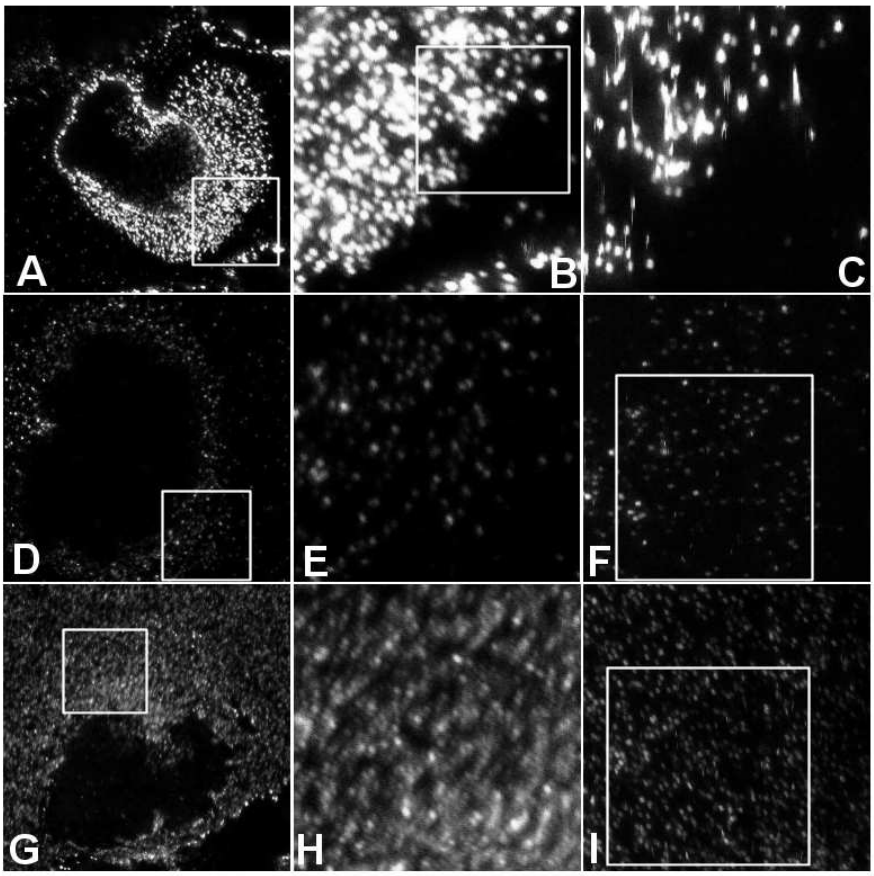

Figure 5.5: High resolution near-field images in liquid, of the surface organization of LFA-1, CD55 and CD71 on THP1. (**A**, **D** and **G**) Representative 40x40 μm^2 confocal fluorescence images show the distribution of LFA-1, CD55 and CD71 on THP1, respectively. The confocal fluorescence images are obtained with 488 nm laser excitation and imaging resolution is diffraction limited at $\sim$ 240 nm. Areas of interest indicated by the white boxes are further inspected by confocal microscopy in (**B**, **E** and **H**). The NSOM images in (**C**, **F** and **I**) are obtained after excitation using an NSOM probe of $\sim$ 100 nm diameter. The intensities are normalized with respect to scan speed and excitation conditions to allow direct visual comparison of the images. Image area is 5x5 μm^2 for LFA-1 and 10x10 μm^2 for CD55 and CD71. The image in **C** corresponds to the white box in (**B**), whereas the white boxes in (**F**) and (**I**) correspond to the images in (**E**) and (**H**).

distribution indicates that at least 60 % of the LFA-1 is clustered. If we assume a one-to-one labeling, clusters can accommodate up to 16 LFA-1 particles. However since in the confocal images not all domains can be visualized separately this number can be slightly overestimated. From the Figure 5.6 **B** and **C** it can be observed that most of the CD55 and CD71 are distributed as single entities. For CD55 35 % of the distribution can not be described using a random distribution of singles, indicating that this fraction is organized in small domains with a maximum of 4 CD55 molecules. A similar fraction of CD71 molecules is organized in small domains mainly containing CD71 dimers.

In relation to this apparent LFA-1 clustering we recently visualized the distribution of LFA1 on monocytes using TEM in combination with immunogold labeling. A typical TEM image together with domain size distribution is presented in Figure 5.7. Only 20 % of the gold particles were detected as single features, indicating that most of the LFA-1 population is present in clusters. Our observations indicate that clustering of LFA-1 is not limited to monocytes, but also occurring in cells that are closely related to monocytes like THP1.

5.4 Discussion

We have been able to directly map the nano-scale compartmentalization of the cell membrane in the most native situation by combining high resolution imaging on cells in liquid with simulations that use experimentally obtained parameters as input. Our high resolution NSOM fluorescence images reflect differences in the spatial distribution of proteins in the cell membrane at physiologically relevant packing densities. Based on the experimental fluorescent spot intensity distributions in combination with simulations for random particle distributions we have been able to determine the extent of true clustering and discriminate between proteins distributed mainly as monomers, like CD55 and CD71 and proteins present in small domains, like DC-SIGN, LFA1 and CD46. An alternative approach to discriminate clustering from random organization is a nearest neighbor distance (nnd) analysis, where nnd distributions for random particles at densities obtained from the experiment can be compared to nnd distributions obtained from measured images [77]. However, besides information on clustering we simultaneously derive cluster content, thus favoring a fluorescent spot intensity analysis over a nnd analysis.

Clustering of LFA1 on monocytes and DC-SIGN on imDCs has also been observed with TEM, but exact quantification of the number of proteins present in a domain is hardly possible using TEM, since the large size of the antibody-gold bead label gives rise to an uncertainty in the number of underlying proteins.

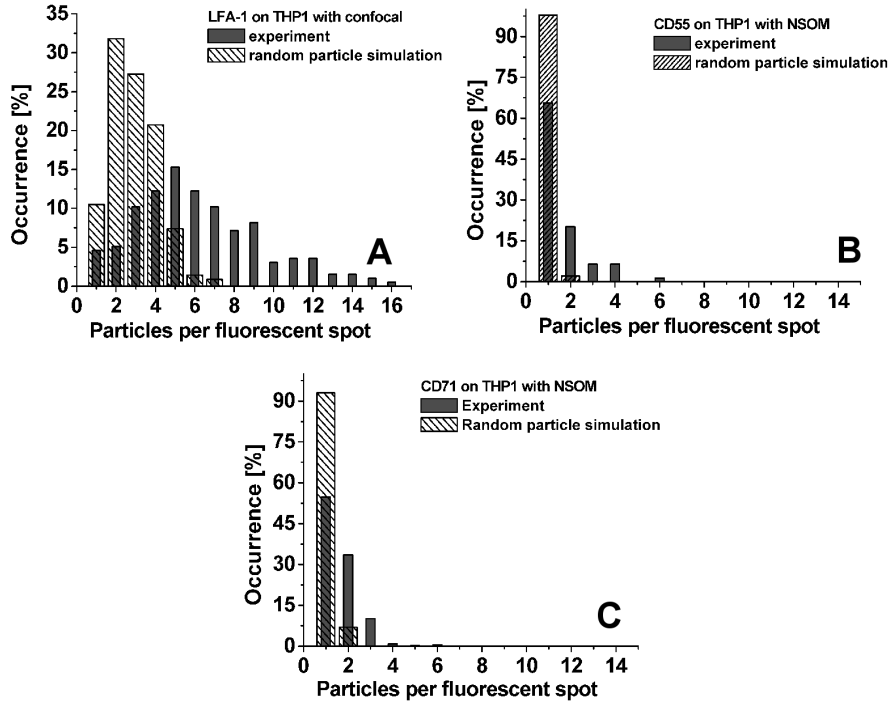

Figure 5.6: Simulations reveal true clustering of LFA-1 on the surface of THP1 while CD55 and CD71 are mainly distributed as single entities. Quantitative representation of the number of fluorescent antibodies present per spot in the measured (gray bars) and the simulated (striped bars) fluorescence images for LFA-1 (**A**), CD55 (**B**) and CD71 (**C**). The relative occurrence on the y-axis is obtained through the total number of spots retrieved from the images. Relating the spot intensities to the intensity of the individual antibodies yielded the number of particles per spot. The distributions for CD55 and CD71 are obtained from NSOM images, while the distribution in (**A**) is obtained from confocal images.

Besides, TEM at this high resolution is only applicable to dried samples, which potentially influences cluster sizes. We have demonstrated that NSOM can give insight in protein distribution at high resolution and in liquid conditions. Together with single molecule detection sensitivity, true domain content can be quantified, by counting the number of fluorescent molecules per domain, provided that the proteins are directly labeled to a fluorophore in a one-to-one ratio. Here, we have used fluorescently labeled secondary antibodies, which leads to an inherent uncertainty due to protein labeling efficiency and variation in number of

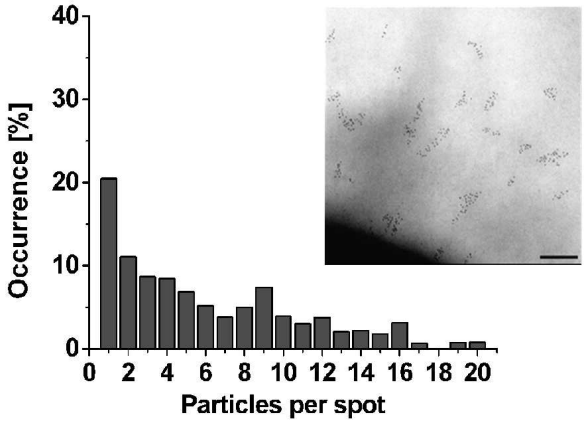

Figure 5.7: TEM images reveal LFA-1 domains on monocytes. The partitioning of gold labels in clusters of various content (i.e.: number of particles/cluster) was quantified. Clusters were defined when gold particles were less than 50 nm apart from a neighboring particle. The percentage of gold particles involved in the formation of a certain cluster size was calculated and the inset shows a representative TEM image. Scale bar is 200 nm. Image is a courtesy of A. Cambi, Nijmegen.

dyes per antibody. The experimental procedures described in this chapter can be readily applied on cells were the proteins are labeled via autofluorescent proteins. This ensures a one-to-one labeling efficiency, however the photophysical properties of most individual autofluorescent proteins (such as low quantum yield, blinking, fast photobleaching) will yield other experimental uncertainties [140]. If we compare the DC-SIGN clusters observed on imDC in liquid with those observed using NSOM on dried imDC [91] we find that on cells in liquid clusters are smaller size and with a lower domain content, suggesting that drying most probably alters domain content.

In relation to the biological function of protein clustering we discovered that on monocytes LFA-1 is organized in small domains that strongly bind to its ligand ICAM-1, while in contrast on DCs LFA-1 is not able to bind to ICAM and is randomly distributed on the cell surface [76]. This surface organization might explain differences in cell virus interactions, since HIV-1 particles bearing host-derived ICAM-1 are efficiently spread by monocytes but not by monocyte-derived DCs [141]. The DC-SIGN domains observed on imDC in liquid strengthen the observation of similar domains on dried imDC with NSOM [91] and TEM [59]. DC-SIGN is able to bind and internalize HIV-1 particles only when it is organized in sub-micron-sized domains and not when randomly distributed [59].

Remarkably, we have also observed domains of CD46, rather similar in shape and content to DC-SIGN and LFA-1. This might indicate a similar relation between domain formation and function for CD46, LFA-1 and DC-SIGN. In fact CD46 has recently been associated to the binding of group B adenoviruses [136], suggesting that protein clustering might be a common mechanism to facilitate virus binding.

CD55 and CD71 are mainly randomly distributed as individual molecules. For CD55 this distribution is consistent with several studies on GPI anchored proteins using diffraction limited microscopy, where no large scale structures have been observed [44]. By means of FRET it was demonstrated that 20-40% of GPI-anchored proteins forms clusters of only a few molecules, whereas the rest is present as monomer. Another FRET study in combination with ratio imaging showed that there was no detectable clustering of GPI-anchored proteins in T-cells [43]. Together these observations using NSOM and FRET indicate that GPI-anchored proteins are mainly distributed as monomers or very small clusters both in size and content. This is consistent with the view that biochemically defined lipid rafts are in fact shells of raft lipids surrounding individual raft proteins [37]. Similar nano-clusters were observed for H-ras and K-ras, where rather 30% of the raft protein exists in cholesterol-dependent nano-clusters, with 70% distributed as monomers [113]. Cluster content was estimated based on number of gold particles per domain and indicated that Ras domains contain at most 8 proteins and have a diameter of 6 nm. In contrast to our findings, CD71 has been observed to cluster in 300 nm sized domains by Vereb and coworkers [133], however the size of these clusters can be directly related to the optical resolution used in their experiments. Since the authors did not relate the brightness of their transferrin receptor clusters to the brightness of the individual Fab fragments used in these experiments, their results can also be interpreted as the diffraction limited imaging of individual transferrin receptors.

Interestingly, the classification of a protein as raft-associated does not give a priori information on its surface organization. Here we found that from the non-raft-associated proteins CD46 appeared in clusters on the membrane of imDC, whereas the raft associated protein CD55 was mainly organized randomly on both imDC and THP1. In this context other important observations are the membrane sub domains distinct from lipid rafts in Jurkat T-cells [38]. The observation of raft markers like Thy-1 and GM1 organizing in small clusters and in distinct membrane areas using TEM [45]. Furthermore, the clustering of raft associated HA was found to be mediated by protein self assembly rather than a partitioning to raft domains [77]. Together these results imply that other mechanisms like protein-protein interaction or arrangement via interactions with the cytoskeleton are responsible for protein aggregation. Interestingly on T-cells actin was needed

for the initial formation of CD2 clusters but not required for their maintenance [38]. For DC-SIGN preliminary observations suggest that releasing DC-SIGN molecules from the cortical actin cytoskeleton by cytochalasin D, results in an enhanced ligand binding, indicating enhanced clustering (unpublished data), and suggesting that the cytoskeleton prevents the formation of aggregates.

It is striking that the protein domains we observed on two different cell types are all well below 100 nm, indicating that a first hierarchial organization occurs at the nanometer scale. The formation of these small predefined clusters could precede, facilitate and accelerate the formation of larger functional structures. For LFA-1 we observed fast recruitment of microdomains to a DC-Jurkat T-cell interface, where larger macroclusters were formed [76].

So far we studied protein organization as such. In the next chapter we will investigate the association between proteins and lipid rafts using high resolution co-localization studies by NSOM in liquid.

5.5 Conclusion

Single molecule sensitive near-field scanning optical microscopy (NSOM) has been used to map on cells in liquid the organization of different protein receptors on two different cell types with a spatial resolution better than 100 nm. The true degree of clustering is assessed by comparing experiments with simulations using experimentally obtained parameters, i.e. receptor density and fluorescence intensity. We discovered that two non-raftmarkers show a completely different surface organization. The transferrin receptor CD71 appears randomly organized on THP1 cells (monocytic cell line) and CD46 forms nano-domains on imDC. Remarkably, the raft associated protein CD55 (a GPI anchored protein), appears non-clustered on both imDC and THP1 cells, but rather organizes in a random fashion. These results demonstrate that the actual membrane organization is not directly related to the classification of a protein as lipid raft associated, i.e. classification as raft marker does not imply clustering and proteins organized in clusters are not necessarily associated to lipid rafts. Therefore clustering is most likely due to other mechanisms like protein-protein interaction in combination with interactions with the cytoskeleton. We have also mapped the organization of the C-type lectin DC-SIGN on imDC and the integrin LFA-1 on THP1 cells. Our results on cells in liquid confirm clustering of these proteins at the nanometer scale, consistent with previous TEM experiments on dried cells. Since all experiments were performed on isolated cells, we hypothesize that the small scale clusters we observe, might precede, facilitate and accelerate the formation of larger functional structures.

Chapter 6

Lipid-protein association at the nanometer scale

Many cellular functions depend on associations between proteins and/or lipids in the cell membrane. Near-field scanning optical microscopy (NSOM) has been used to simultaneously investigate the nanometer scale spatial organization of different proteins and lipids on immature dendritic cells (imDC) and THP1 cell in solution. The extent of co-localization has been quantified using Pearsson's correlation coefficient and the results have been compared to confocal co-patching experiments. Significant association of different proteins (DC-SIGN and CD55 on imDC; and LFA-1 and CD71 on THP1) to the lipid raft marker GM1 has been observed using confocal co-patching. Strikingly, this spatial correlation has not been observed upon direct NSOM investigation, i.e., on fixed cells in solution with no co-patching. The potential nano-scale spatial proximity of these proteins to the raft marker GM1 has been also investigated using interparticle nearest neighbor distance (nnd) analysis. The resultant nnd distribution for CD71-GM1 is completely random consistent with the fact that CD71 is a non-raft associated protein. On the contrary, the nnd distributions of CD55-GM1 and LFA1-GM1 are significantly shifted to shorter distances compared to random organization. These results indicate a statistically relevant preference for LFA-1 and CD55 to be in close proximity to lipid rafts. Altogether, our findings favor a model in which both proteins and lipids are pre-organized into small separate nanoscale domains, where these nanodomains might function as cell membrane organizers that facilitate and accelerate the formation of larger functional domains.

6.1 Introduction

In the previous chapters we have separately studied the organization of lipids and proteins in the cell membrane at the nanometer scale. More interesting and biological relevant information can be inferred by investigating the association between different membrane components. Especially in the context of lipid rafts, the association of proteins to rafts is used to derive information on protein function in cellular process like, virus capture and cell-cell signaling.

Several methods can be used to investigate the association of different species within the membrane. The first operational criterion to define raft-association of proteins is their resistance to solubilization by detergents [23, 31] forming so called detergent resistant membranes (DRMs). These DRMs can be separated from the rest of the cell lysate by ultracentrifugation on a sucrose gradient after which the exact composition can be analyzed via immunoblotting. However DRM analysis is prone to artifacts since temperature changes and changes in detergent concentration significantly alter phase behavior and therefore DRM composition [33]. Despite the wide application of DRM analysis, it is well recognized that this method is not suited to obtain reliable information on the association between proteins and lipids in the cell membrane. To reveal information on association or co-localization, in principle all techniques already described in Chapter 4 could be used by introducing only slight modifications. For instance, in the case of transmission electron microscopy (TEM) in combination with immunogold labeling, different sized gold particles can be used to identify different species after which a bi-variate Ripley's K analysis reveals information on associations [142]. In the case of fluorescence microscopy, the association of multiple species can be investigated by labeling different membrane components with distinct fluorophores. In this context, the most commonly used fluorescence based techniques are confocal co-patching and fluorescence resonance energy transfer (FRET). Essentially co-patching relies on the formation of aggregates of membrane components, large enough to be visible with light microscopy, using secondary antibodies [36]. It is generally assumed that if the two species are organized in the same membrane phase, aggregation of one will force the other to follow, so co-localization with the raft marker after patching will be indicative for raft association [63]. The validity of this assumption has however been questioned by some groups. Furthermore, protein cross-linking itself can have a signaling function, resulting potentially in artificial protein redistribution [35]. FRET is widely used to detect molecular associations [62, 143], since the occurrence of FRET between donor and acceptor located on different lipids and/or proteins is evidence for their close proximity. Currently, the general consensus in the field is that different techniques have revealed different composition and size of lipid rafts, and there is still no single

technique that can probe the small size and dynamic nature of rafts simultaneously [39]. As a result, the composition and even the existence of lipid rafts remains under debate [29] and each technique to study raft composition has its own pitfalls.

In the previous chapters we already demonstrated that the diving bell NSOM concept is capable of imaging nanometer sized protein and lipid domains on cells in liquid, domains not visible with confocal microscopy due to the combination of high packing density and limited optical resolution. Here we use simultaneous dual color excitation and detection NSOM to perform co-localization studies. Because of the superior resolution of NSOM there is no need for co-patching membrane components to visualize domains, thus preventing artificial aggregation. An additional advantage of dual wavelength NSOM excitation is that the two beams share the same aperture and images are acquired pixel by pixel, so that the two fluorescence images are free from chromatic aberrations, in contrast to confocal microscopy [85].

Here we have performed high resolution co-localization experiments between CD55, CD46 and DC-SIGN to the lipid raft marker GM1 on imDC and CD55, CD71 and LFA-1 to GM1 on THP1 cell, both in liquid conditions. Our results show no specific association between any of these proteins to GM-1, in contrast to confocal experiments where co-localization after co-patching has been consistently observed for CD55 and DC-SIGN on imDC and CD71 and LFA-1 on THP1. These results indicate that co-patching is not suited to obtain reliable information on membrane organization and raft partitioning. Although no clear co-localization using NSOM was observed, detailed nearest neighbor distance analysis indicated a statistical relevant preference for LFA-1 and CD55 to be in the close proximity of lipid rafts. These results are consistent with a model in which both proteins and lipids are pre-organized into small separate nanoscale domains. A possible function for these nanodomains is a role in facilitating and accelerating the formation of larger functional domains by acting as cell membrane organizers.

6.2 Materials and Methods

6.2.1 Sample preparation

Monocytes were obtained from buffy coats (fraction of a centrifugated blood sample that contains most of the white blood cells) of healthy individuals and purified using Ficoll density centrifugation. ImDCs were obtained as reported elsewhere [66]. In brief, DCs were cultured from monocytes in presence of IL-4

and GM-CSF (500 and 800 U/ml, respectively) for six days to obtain imDCs.

For NSOM/confocal microscopy, cells were stretched on poly-l-lysine coated coverslips for 45 minutes at 37^oC. After blocking on ice with PBS (containing 3%BSA and 20mM Glycine) for 30 minutes at 4^oC, the cells were labeled with $10\mu g$/ml Alexa-647-CTxB also at 4^o C to minimize internalization of CTxB. After washing three times with PBS the cells were fixed using 1% PFA in PBS for 20 minutes at room temperature, followed by two PBS washing steps and again blocking for 1 hour. The proteins of interest were then labeled at room temperature with either $10\mu g$/ml anti-DC-SIGN antibody, anti-CD55 antibody or anti-CD46 antibody. Secondary staining was performed with Alexa 488-conjugated goat anti-mouse IgG. Finally the samples were washed three times with PBS. Wet samples were stored in PBS containing 1% PFA until use.

The THP1 cells were cultured in RPMI 1640 Dutch modification medium supplemented with 10% Fetal Calf Serum and antibiotic-antimycotic from Gibco. After a similar procedure to label with Alexa-647-CTxB as for imDC the proteins of interest are labeled with either $10\mu g$/ml anti-LFA1 (TS2/4) antibody, anti-CD55 antibody or anti-CD71 (transferrin receptor) antibody. Secondary staining was performed with Alexa488-conjugated goat anti-mouse IgG and stored similar to imDC samples. Isotype specific controls were always included.

To patch GM-1 for confocal experiments, CTxB was cross-linked using goat anti-CTxB and patching was induced by incubation at 12^oC for 1 hour, followed by fixation with 2% PFA. Cells were mounted (no stretching) onto poly-l-lysine coated coverslips.

6.2.2 Confocal and near-field fluorescence microscopy

Experiments on stretched cells were performed using a home built confocal/NSOM microscope optimized for single molecule detection. All experiments were performed in liquid, using the diving bell concept for NSOM inspection as described in Chapter 2. The molecules of interest are labeled with either Alexa-488 or Alexa-647 (see Sample preparation) and are excited using the 488 nm and 647 nm lines, respectively, of an argon/krypton-ion laser (CW, Spectra-Physics).

In confocal mode, circularly polarized excitation light is reflected by a dichrioc mirror (Omega Optical Inc.) and focused onto the sample using an oil immersion objective (60x, 1.4 NA). In the NSOM mode, the sample is excited via the fiber probe. The emitted fluorescence is collected and spectrally separated from the excitation light using appropriate longpass filters (Omega Optical Inc.) and detected using a photon counting avalanche photodiode (APD, SPMC-100, EG&G,

Quebec). Co-localization experiments on imDC were performed by exciting the sample simultaneously using the 488 nm and 647 nm lines of two argon/krypton-ion lasers (CW, Spectra-Physics). For THP1 cells the 647 argon/krypton laser was replaced with a 632 helium/neon laser. In confocal mode the two lines are spatially overlayed using a pinhole.

In NSOM mode, both laser lines are coupled into the fiber probe. The small aperture of the near-field probe ensures a perfect spatial overlay of the two different excitation wavelengths. As such, the technique is free of chromatic aberrations in contrast to conventional confocal microscopy. The fluorescence emission is collected by the 1.4 NA objective, passed through a 510 nm longpass filter to reduce autofluorescence from the NSOM fiber and spectrally separated using a 565 nm DRLP dichroic mirror (Omega Optical Inc). The emission is collected by two APDs after passing through additional filters, i.e. a 510-560 nm bandpass filter in the Alexa-488 channel and a 670 nm longpass in the Alexa-647 channel.

Confocal co-patch experiments were performed on a biorad MRC1024 Confocal Laser Scanning Microscope. Signals were collected sequentially to avoid bleed through.

6.2.3 Fluorescence recovery after photobleaching

The degree of protein and lipid mobility in the cell membrane after 1% PFA fixation was investigated using fluorescence recovery after photobleaching (FRAP). Experiments were performed on a Zeiss LSM 510, using a PlanApochromatic 63x 1.4 oil immersion DIC lens (Carl Zeiss GmbH, Jena, Germany) with the confocal pinhole completely open. Fixed THP1 cells were labeled following a similar procedure as for NSOM/confocal microscopy, using Alexa-647-CTxB to label GM1 and anti-LFA-1 (TS2/4) antibody to label LFA-1. Secondary staining was performed with Alexa488-conjugated goat anti-mouse IgG. Photobleaching of Alexa488 or Alexa647 was performed using repeated scans with the 488 nm or 633 nm laser line at full power in a square area of 3x3 μm^2. Pre- and post bleach images were monitored at low laser intensity. Fluorescence recoveries in the bleached region were quantitated using Zeiss LSM Image Browser version 3.2 (Carl Zeiss). Recovery curves were averaged over multiple cells for both LFA-1 and GM1 in fixed cells and GM1 in living THP1 cells.

6.2.4 Image analyses

Co-localization between the raft marker GM1 and the protein of interest was analyzed using a custom written analysis program in LabView. For a selected imaged area of the cell membrane the correlation between two labels (denoted

here as red and green) is calculated using the Pearssons correlation coefficient C, defined as

$$C = \frac{\sum_{i=1}^{n}\sum_{j=1}^{n}(R_{i,j} - \bar{R})(G_{i,j} - \bar{G})}{\sqrt{\sum_{i=1}^{n}\sum_{j=1}^{n}(R_{i,j} - \bar{R})^2(G_{i,j} - \bar{G})^2}}$$

where, $R_{i,j}$ and $G_{i,j}$ are the fluorescence intensities at pixel coordinates (i, j) for the red and green channel images respectively. The parameters $\bar{R}$ and $\bar{G}$ are the average intensity values for the total images R and G respectively. C can vary from -1 (anti-correlated), 0 (uncorrelated) to 1 (fully correlated). A routine to calculate the Manders coefficients [144] was implemented, using a scatter plot analysis, similar to the work of Costes et al. [145]. For the confocal co-patching data acquired using the commercial confocal microscope, background and unspecific labeling were corrected by adjusting the photo multiplier tube gain settings such that no signal is detected for the isotype control. For confocal and NSOM images obtained on the single molecule sensitive setup, background and crosstalk were corrected prior to image analysis.

To estimate the contribution of random co-localization for the NSOM images the correlation between two images with random particle positions at densities comparable to the experimental conditions has been calculated. In addition to the correlation coefficient C, we have also calculated inter image nearest neighbor distances, i.e. the shorter spatial separation between GM1 and the protein of interest. For both the GM1 (red) and the protein (green) images the (x, y) coordinates of each spot position are first stored. To obtain the inter image nearest neighbor distance, each (x, y) position in the 'red' image is then mapped on the 'green' image (or vice versa). The absolute (x, y) differences between the GM1 and protein spots are calculated and the smallest differences (x_m, y_m) are stored. The nearest neighbor distances are calculated as $\sqrt{x_m^2 + y_m^2}$ and converted to a frequency distribution histogram, reflecting the nearest neighbor distribution (nnd).

Since proximity beyond the imaging resolution is not measured using a correlation algorithm, we validate a potential proximity effect by comparing the experimental nnd to nnd obtained from simulated images. Therefore images with random particle positions are obtained using the program described in Chapter 4. In either the 'red' or the 'green' image the (x, y) coordinates of each spot are obtained from a random number generator. Proximity effects can be simulated by applying a shift over a mean distance in a random direction on each particle after which the shifted particle coordinates are stored. Using the particle coordinates, for either the images with random particle positions or the images with shifted particle positions the inter image nearest neighbor distance is calculated.

6.3 Results

6.3.1 Image analysis and simulations

Before analyzing cell images we first calculated the correlation coefficient for CTxB-Alexa647 on a glass coverslip labeled with anti-CTxB-Alexa488. The confocal image from this experiment is shown in Figure 6.1 **A**, together with the calculated correlation coefficient C=0.8. The deviation from 1 is readily explained by aspecific binding of anti-CTxB-Alexa488 to the glass coverslip, but a value of 0.8 is clearly indicative for co-localization. This result also indicates that full correlation should never be expected when investigating protein-lipid or protein-protein co-localization using antibody labeling. In contrast, the comparison of two simulated images with random particle positions yield a correlation value of zero although some yellow spots can be identified in the image in Figure 6.1 **B**. The influence of a random shift of 100 nm to each particle position in one of two originally identical images has also been investigated. The combination of two identical images results in $C = 1$ with the occurrence of only yellow spots as shown in Figure 6.1 **C**. On the other hand, the small random shift reduces the correlation to 0.4 as can be seen in Figure 6.1 **D**. Thus, the correlation between two images substantially decreases as a result of the random shift enforced on the particles in one of the images. This in fact could represent a situation in which the proteins are properly fixed, but lipids are still able to slightly diffuse. Can a nnd analysis reveal a proximity effect indicative of a prior association?

To illustrate how the nnd distribution changes after a random shift of each particle position we first obtain the inter image nnd distributions for two images with randomly distributed particles. Both images have a particle density of 20 particles per μm^2. The inter image nnd is shown in Figure 6.2 **A**. The mean ($\pm$ standard error of the mean) of this distribution reflects an average nnd of 113 $\pm$ 1 nm, in fact reflecting the used particle density since the nnd is related to $\sqrt{1/4D}$, where D is the particle density [146]. The same analysis performed for two identical images, i.e. C=1, yields zero for the mean value of the nnd. If in one of the images each particle position is shifted in a random direction over 0.1 $\pm$ 0.1 μm (the typical size of an NSOM probe) this results in the nnd distribution shown in Figure 6.2 **B**. The peak of this distribution is shifted towards lower nnd values as compared to the random situation, while the mean value is 76$\pm$1 nm. Thus even though particles were shifted, the initial association is still reflected by the nnd distribution. The relation between a random particle shift and the mean nnd value is investigated for two particle densities and the results are shown in Figure 6.2 **C**. Two identical images result in zero for both shift and mean nnd. For small particle position shifts, the shift distance is dominant over the

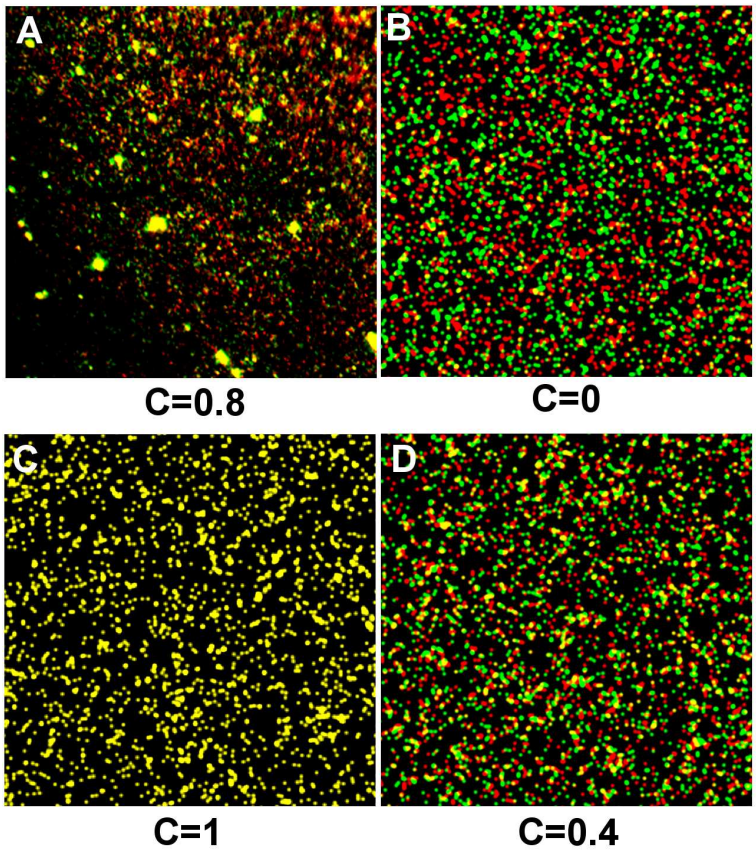

Figure 6.1: Co-localization imaging examples: from co-localization via random organization to mutual shifted images. (**A**) Co-localization in a confocal experiment where antibodies against CTxB-Alexa647 were labeled with Alexa-488.(**B**) Co-localization between two simulated images with random particle positions at particle density of 20 particles/μm^2. (**C**) Co-localization between two identical images at particle density of 20 particles/μm^2.(**D**) Image obtained using the image combination in (**C**) after shifting each particle position randomly over 100 $\pm$ 100 nm, on one of the images.

nnd expected on basis of the particle density. For larger shifts the mean nnd gradually converges to the nnd value corresponding to the particle density. In the same panel the correlation coefficient as function of particle position shift is shown. C=1 for two identical images and C gradually converges to 0.

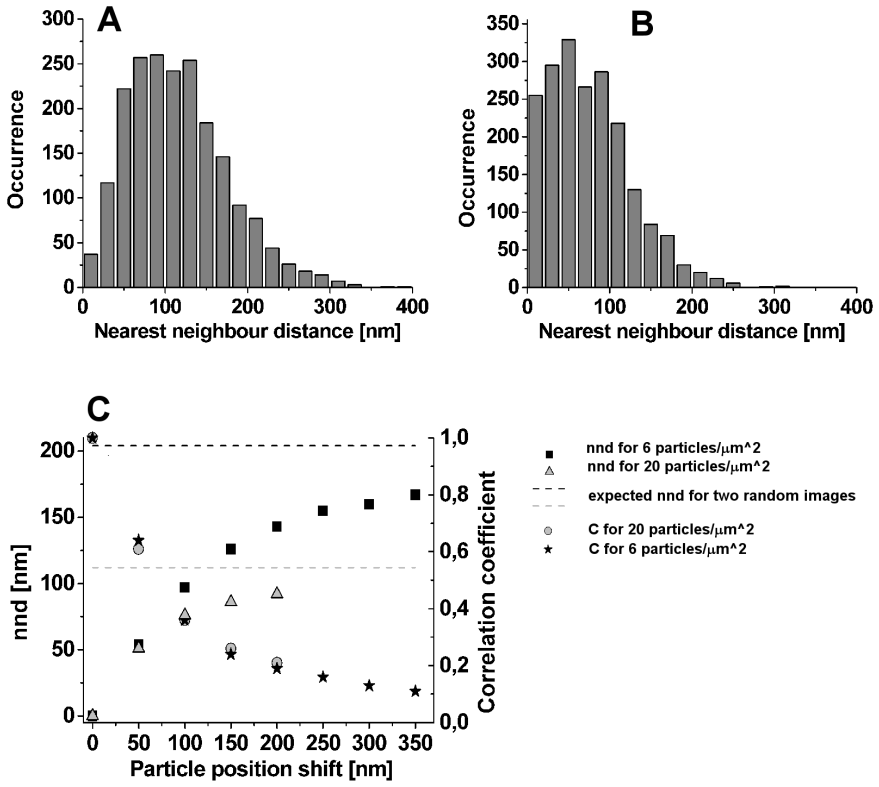

Figure 6.2: Nearest neighbor distance analysis reflects particle proximity. (**A**) nnd for two random images each with an image density of 20 particles/μm^2. (**B**) nnd of two identical images after shifting all particle positions in one image in a random direction over a mean distance of 100 $\pm$ 100 nm. (**C**) Mean inter image nearest neighbor distance as function of a random particle shift (mean shift value is standard deviation) for two different particle densities (6 particles/μm^2 and 20 particles/μm^2). Expected mean values for the nnd based on particle density (straight lines) and mean nnd values for simulated images (squares and triangles). Correlation coefficient as function of random particle shift (circles and stars).

6.3.2 Confocal co-patching and co-localization

In the previous chapters it has been mentioned that CD55 and DC-SIGN resided in lipid rafts in imDCs. These findings are based on DRM extraction and confocal co-patching experiments [59]. Here we analyze the data obtained using confocal co-patching in a quantitative manner by calculating the correlation coefficient for the signal from the lipid raft channel, visualized via GM1, with respect to the signal from the protein channel. In addition to these two raft markers we also analyzed confocal co-patch data for the non raft marker CD46 [59] and the transmembrane protein LFA-1. In Figure 6.3 **A** domains in the GM1 staining can be identified, indicating that the patching was indeed successful. From a first visual inspection of the confocal images it is already clear that CD46 and LFA-1 do not partition in lipid rafts, whereas CD55 appears fully associated and DC-SIGN partially associated. Quantitative analysis, calculating C confirm that indeed CD46 and LFA-1 are not raft associated. In contrast to the visual impression, quantitative analysis reveals that both DC-SIGN and CD55 show a similar degree of raft association as shown in 6.3 **B**.

The association of CD71 and LFA-1 to lipid rafts has been investigated in a similar manner for THP1 cells. Surprisingly, upon first visual inspection, both CD71 (a non-raft marker) and LFA1 appear associated to GM1 in a similar degree as shown in Figure 6.4 **A**. LFA-1 shows a comparable degree of association on monocytes, to which the THP1 cell line is closely related. Quantitative analysis, calculating C confirms that indeed CD71 and LFA-1 are raft associated on THP1 cells and that LFA-1 shows a similar degree of raft association on monocytes as shown in 6.3 **B**. All co-patch experiments were performed on cells in suspension. We also tried to co-patch proteins and lipids on cells stretched on PLL coated coverslips, but patching was less successful for these samples, probably caused by a decreased mobility due to firm adherence to the coverslip (results not shown).

6.3.3 Degree of protein and lipid mobility after fixation

For our high resolution NSOM experiments we have chosen a mild PFA fixation of the cells. In this we expect to preserve the membrane architecture in the most native way. However, a mild fixation might not be sufficient to fix all membrane components, in particular the smaller lipids. To investigate the degree of mobility of GM1 and LFA-1 after 1% PFA fixation, we used confocal FRAP. In these experiments, the mobility of either LFA1 or GM1 was registered, by monitoring the fluorescence of the antibody or CTxB labels using low-intensity laser excitation. A 3x3 μm^2 area was first photobleached using high-laser power

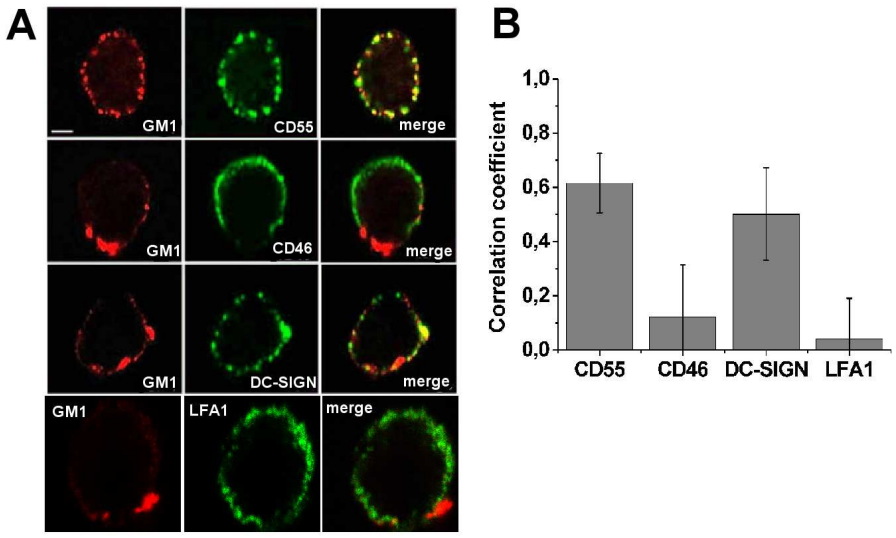

Figure 6.3: Quantitative co-localization analysis of protein-raft association on imDCs. (**A**) Confocal microscopy analysis of co-patching of DC-SIGN, CD46, CD55 and LFA-1 to GM1. Cells were stained as described in Materials and Methods and co-patching was induced by adding secondary antibody, after which the imDC were fixed. Merged images are shown in the right panel. Results are representative of multiple cells. (Scale bar = 5 μm). (**B**) The bar graph shows C calculated for the different proteins. Results are the average of multiple cells, n=7;6;11;9 for respectively CD55;CD46;DC-SIGN;LFA-1.

and the diffusive exchange of bleached species with nearby unbleached species was then followed. A representative THP1 cell before and after bleaching is shown in Figure 6.5 **A** and **B** respectively.

Recovery into the bleached area can be described using the mobile fraction (M_f) [147], which reports on the fraction of fluorescent molecules that are able to recover into the bleached area over the time course of the experiment. For GM1 and LFA-1 the recovery is examined both 15 minutes and 1 day after fixation, together with the recovery of GM1 in live THP1 cells as shown in Figure 6.5 **C** and **D**. The corresponding M_f values for GM1 are 0.17 for PFA fixation and 0.42 for live cells. For LFA-1 we find a M_f of 0.07 after fixation. For LFA-1 the proteins were expected to be totally immobile so the slight mobile fraction found here is probably the result of focal drift, also indicated by the slight linear slope in the recovery curve. The mobile fraction of GM1 in living THP1 cells is lower than reported in literature [5] using similar labeling procedures. The lower mobility might be explained by GM1 associated to immobile caveolae or reduced

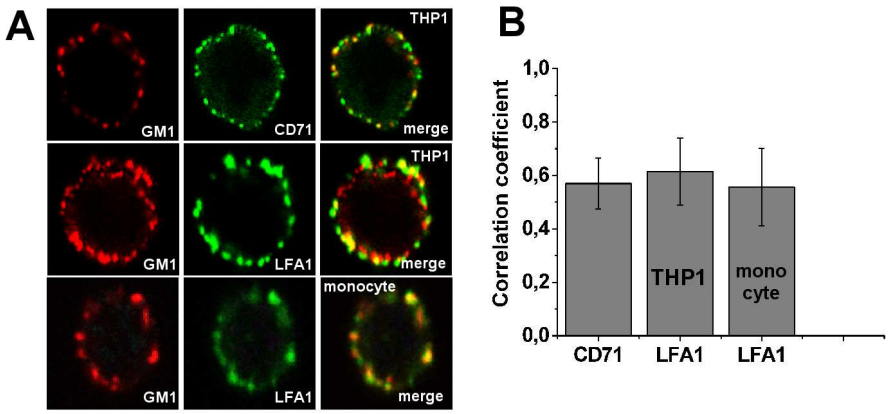

Figure 6.4: Quantitative co-localization analysis of protein-raft association on THP1 cells and monocytes. (**A**) Confocal microscopy analysis of co-patching of CD71 and LFA-1 to GM1 on THP1 and LFA-1 to GM1 on monocytes. Cells were stained as described in Materials and Methods and co-patching was induced by adding secondary antibody, after which the THP1 cells or monocytes were fixed. Merged images are shown in the right panel. Results are representative of multiple cells. (Scale bar = 5 μm). (**B**) The bar graph shows C calculated for the different proteins. Results are the average of multiple cells, n=30;42;21 for CD71 and LFA1 on THP1 and LFA-1 on monocytes, respectively.

membrane mobility due to interactions with the PLL coated glass coverslip. The mobile fraction of GM1 gets further reduced upon fixation. Assuming that the low LFA-1 mobility is indeed the result of focal drift, the overall mobile fraction of GM1 after fixation is then 0.10. Thus 1% PFA fixation is suitable to fully immobilize LFA1 while only 10% of the GM1 population remains mobile.

To get a first indication of the speed at which the mobile population diffuses, the diffusion coefficient is estimated. For simplicity the recovery curve is fitted using an empirical formula which agrees within 5% with the solution of the diffusion equation in one dimension for recovery into an interval of zero intensity given by [148]:

$$I_t = I_{final}\sqrt{1 - \frac{w^2}{w^2 + 4Dt\pi}},$$

where I_t is intensity as function of time, I_{final} is the intensity after recovery, w is the width of the bleaching area, i.e., 3 μm and D is the one-dimensional diffusion constant. If we use an I_{final} of 0.17 the corresponding value for D is 0.01 μm^2/s. This means that if 10% of the GM1 remains completely mobile ($D = 0.01$ μm^2/s), these lipids can easily diffuse over the entire membrane.

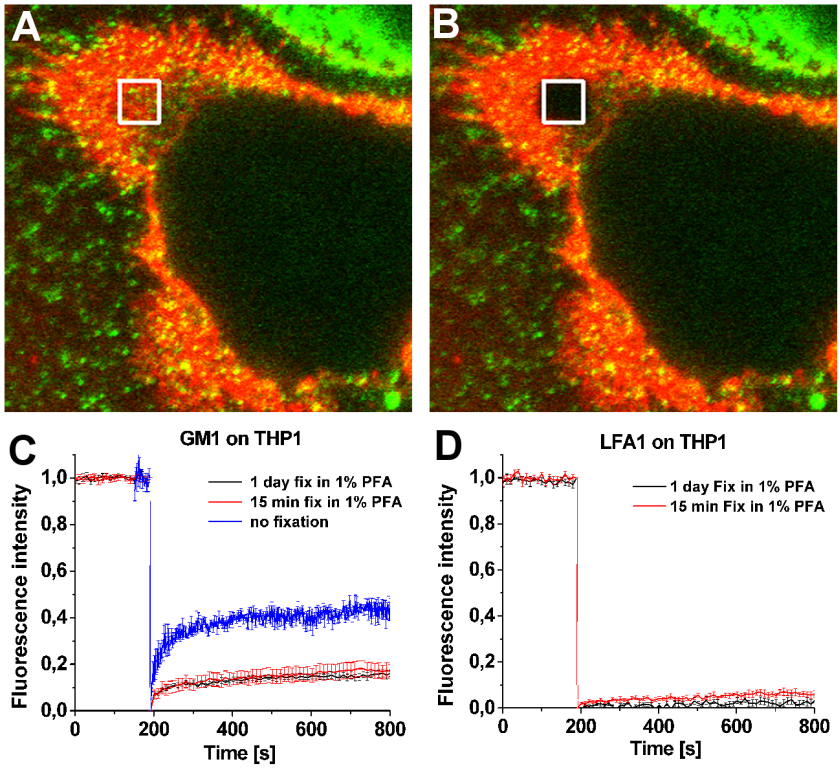

Figure 6.5: FRAP experiments to reveal lipid and protein mobility after fixation of THP1 cells. (**A**) and (**B**) Selected images before and after bleaching in a confocal FRAP experiment on THP1 where GM1 is labeled using CTxB-Alexa647 (red) and LFA-1 is labeled via an Alexa-488 antibody (green). Bleach box, 3x3 μm^2. (**C**) Recovery curves of GM1 on THP1: 1 day after fixation (black line), 15 minutes after fixation (red line), live cell on PLL (blue line).(**D**) Recovery curves of LFA-1 on THP1: 1 day after fixation (black line), 15 minutes after fixation (red line). Each curve shows the mean ± SD from seven to eight cells from two experiments.

6.3.4 Quantitative co-localization from NSOM images

As already demonstrated in the previous chapters, the superior spatial resolution of NSOM allows the direct visualization of protein and lipid domains on cell membranes at the nanometer scale. This provides the unique possibility to investigate the cell membrane directly, without inducing artificial aggregation by co-patching. For THP1 cells in liquid the association of the GPI-anchor CD55, transferrin receptor CD71 and the integrin LFA-1 to GM1 has been investigated. Prior to high resolution NSOM imaging, cells were first inspected using dual color confocal microscopy. Representative images for each protein are presented in Figure 6.6. Interestingly from the confocal images (left and middle columns) LFA-1 appears to be fully associated to GM1, while CD71 and CD55 show considerable co-localization, as evidenced by the yellow features in the images. From the NSOM images (most right column) it is immediately clear that we indeed resolve both lipid and protein domains simultaneously. Strikingly, in the NSOM images most yellow spots have disappeared. This indicates that most of the apparent co-localization in the confocal images is in fact the result of the limited confocal spatial resolution, probably in combination with internalized CTxB not excited by the small illumination depth of NSOM excitation. To quantify the co-localization in the NSOM images we again use a similar analysis as for the confocal co-patch data. Relevant cell areas are selected, background and crosstalk (typically 5% from green to red channel) are corrected and C is calculated. The results for the different proteins are presented in Figure 6.7. These quantitative results clearly demonstrate the lack of correlation between any of the proteins and GM1 in sharp contrast with the results obtained with confocal co-patching on THP1 where both CD71 and LFA-1 exhibited significant co-localization with GM1. Similar NSOM experiments were performed on imDC in liquid, investigating the co-localization of DC-SIGN, CD55 and CD46 to GM1. This resulted in C values of -0.01$\pm$0.09 for DC-SIGN, -0.01$\pm$0.06 for CD55 and 0.02$\pm$0.08 for CD46, thus revealing similar discrepancy with the confocal co-patch results.

6.3.5 Protein-raft spatial proximity inferred from nearest neighbor distance analysis

Clearly, high resolution co-localization studies show no association between lipid and protein organization at the nanometer scale. These results are rather surprising since both CD55 and LFA-1 are reported to partition in lipid rafts [58, 76, 149]. To further investigate the tendency for those proteins to reside in lipid rafts, we have also retrieved their mutual spatial proximity by performing inter-image nnd analysis according to the approach indicated in section 6.3.1. A physical separa-

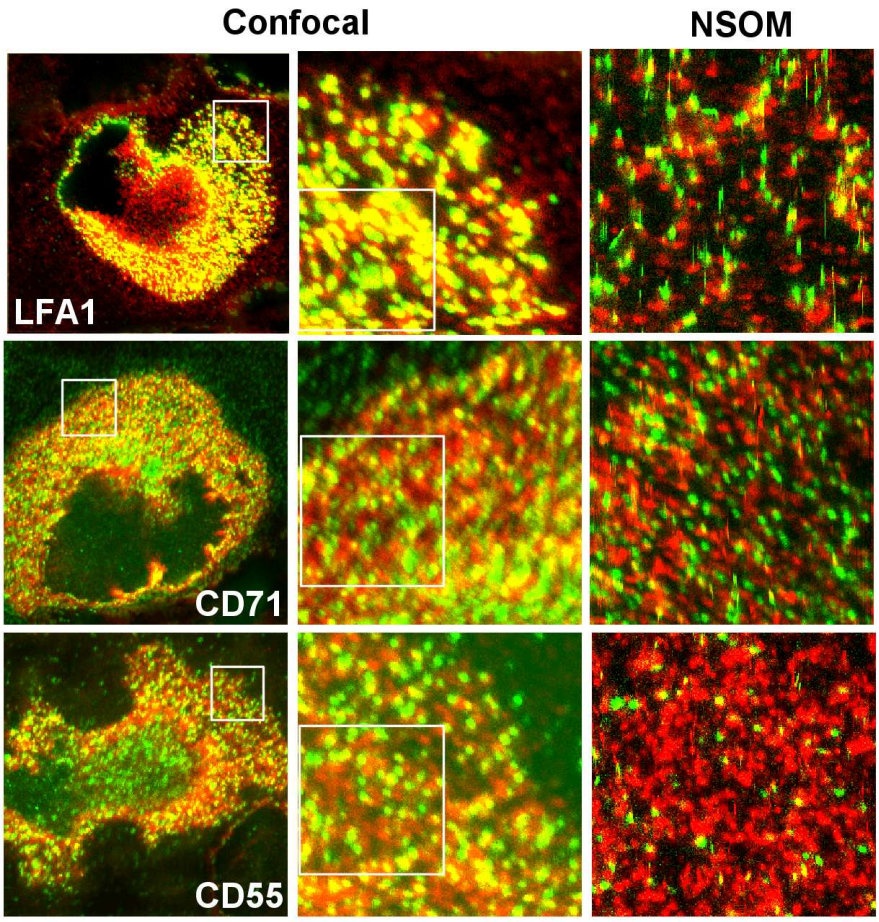

Figure 6.6: High resolution near-field imaging in liquid to investigate association of LFA-1, CD71 and CD55 to GM1 on THP1 in liquid. (left column) Representative 40x40 μm^2 confocal fluorescence images show a merge of GM1 (red) and the proteins LFA-1, CD71 and CD55 (green) signal. Areas of interest indicated by the white boxes are further inspected by confocal microscopy in middle column. The NSOM images (right column) are obtained after NSOM excitation using a probe of $\sim$ 100 nm diameter. Image areas are 5x5 μm^2.

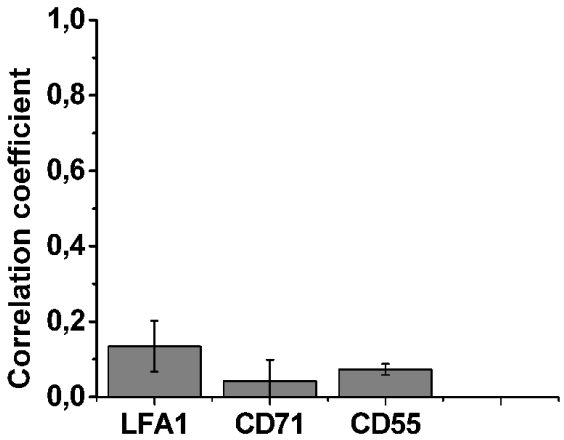

Figure 6.7: Quantitative co-localization analysis using NSOM on THP1 in liquid. Each bar gives the average correlation ($C \pm$ SD) calculated for LFA-1, CD71 and CD55 to GM1. Results are the average for several areas selected on multiple cells.

tion between the raft marker and the specific protein shorter than that expected for a random distribution of both components will be indicative of their affinity or predisposition to be associated. At the same time, the analysis will also serve to assess the potential effect of lipid mobility after mild fixation of the membrane using PFA. In fact, it is known that some mobility of the small lipids in the cell membrane can still persist after PFA fixation (E. Gratton, personal communication). This mobility could then affect the overall association between the lipid marker and the protein of interest, resulting in a lower correlation coefficient during our measurements.

The inter image nnd analysis has been performed for LFA-1, CD71 and CD55 to GM1 on THP1 cells. All fluorescent spot positions are manually identified in the fluorescence images and the (x, y) positions are stored to calculate the nearest neighbor distances. For each protein this results in an nnd frequency distribution as shown in Figure 6.8. These experimental distributions are compared with nnd distributions obtained from images with simulated fluorescent spots placed at random positions. For the simulations the density of fluorescent spots is obtained after dividing the number of fluorescent spots in the experimental images by the cell area. For each protein, the frequency distribution resulting from this simulation is combined with the experimental nnd frequency distribution as shown in Figure 6.8. For the nnd obtained from both experiment and simulations the mean nnd ($\pm$ standard error of the mean) can be calculated. The expected mean

protein	Experiment [nm]	Simulation [nm]	Theory [nm]
LFA-1	155±7	197±3	199
CD55	156±9	185±4	184
CD71	231±7	227±2	226

Table 6.1: Mean inter image nearest neighbor distance values for protein to GM1 distances. The tabulated values are mean±standard error of the mean. The column theory contains the nnd values that are calculated from experimentally obtained spot densities.

nnd can also be directly calculated based on the spot densities obtained from the experiment. The resulting mean nnd values are shown in Table 6.1. Clearly the experimental and simulated nnd distributions for CD71 fully overlap, resulting in similar values for the mean nnd. This indicates that CD71 is randomly organized with respect to GM-1 and demonstrates no-association consistent with the fact that CD71 is a non-raft marker. In contrast, the results on LFA-1 and CD55 show a statistically significant shift (∼40 nm for LFA-1 and ∼30 nm for CD55) to shorter nnd values, a clear indication of their tendency to be associated.

6.4 Discussion

In this chapter we have investigated in a quantitative manner the co-localization between proteins and lipids on different cell types using two different fluorescence methods: standard co-patching and high resolution NSOM in liquid conditions. The results using confocal co-patching indicate that both the GPI-anchored protein CD55 and the C-type lectin DC-SIGN on imDCs are partially associated to lipid rafts, while CD46 was found to partition in the non-raft fraction. These results are consistent with previous published results where CD55 was found to partition in rafts whereas CD46 was excluded from the raft fraction [59]. In the same paper DC-SIGN was demonstrated to be partially associated to lipid rafts, by using TEM and DRM extraction complementary to confocal microscopy. In this chapter, we obtained co-localization data for THP1 cells in a similar manner. Here quantitative analysis of confocal co-patching data revealed raft partitioning for the transferrin receptor CD71 and the integrin LFA-1. Especially the raft partitioning of CD71 is striking, since this protein is commonly used as a marker that is excluded from lipid rafts [63, 64]. In remarkable contrast to these results, direct investigation using high resolution NSOM revealed no or very low co-localization ($C \sim 0$) for all proteins both on imDC and THP1 cells.

Others have observed a similar lack of co-localization between GPI-anchored proteins and GM-1 using high resolution TEM studies [45], where the GPI an-

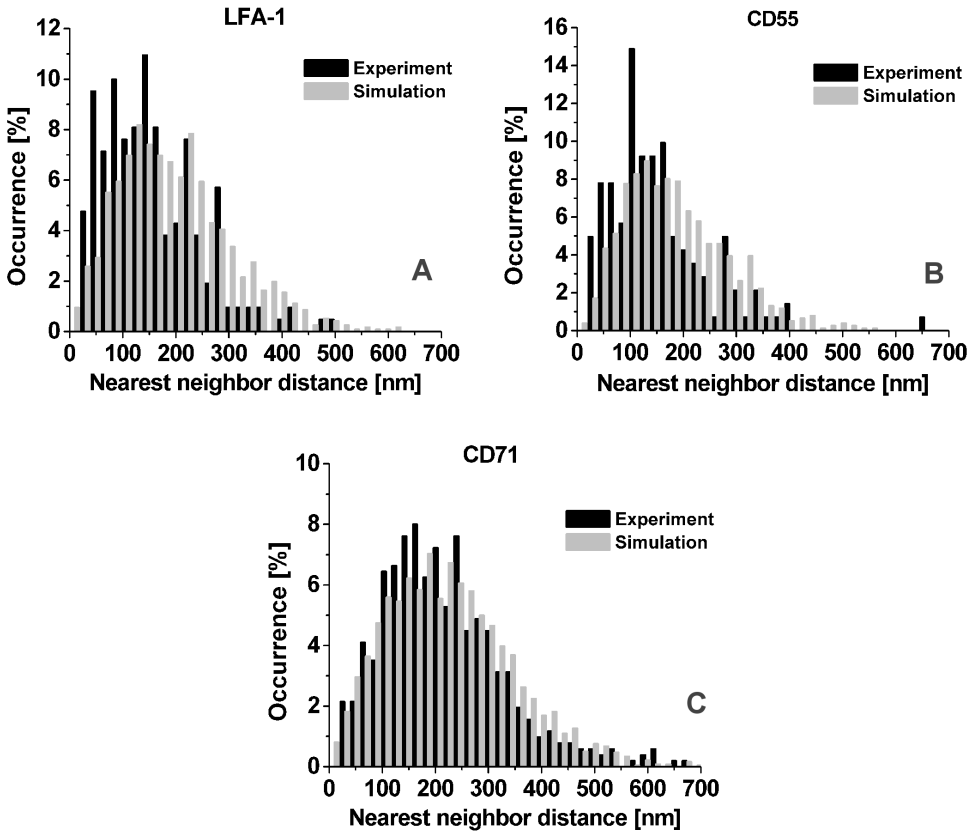

Figure 6.8: Nearest neighbor distance analysis: experimental results compared to simulations. Each plot contains an nnd frequency distribution obtained from experimental data (red bars) and a distribution obtained from simulations (grey bars), LFA-1:GM1 in (**A**), CD55:GM1 in (**B**), CD71:GM1 in (**C**). Simulations use experimentally obtained fluorescent spot densities for both proteins and lipids as input.

chored protein Thy1 is rarely co-localized with GM1. Together with our NSOM results this clearly proves that recovery of two raft markers in the light-density fractions does not predict their co-distribution in cell membranes.

The differences between confocal co-patching and NSOM results remain rather intriguing. Given the small domain sizes and high packing density, the superior lateral resolution of NSOM in combination with a penetration depth of $\sim$100 nm is the key ingredient to obtain direct insight in membrane organization. In contrast, using confocal microscopy the lateral resolution is at best limited by diffraction

and the axial resolution is ∼600 nm. As demonstrated in the previous chapters NSOM therefore allows the direct visualization of lipid and protein domains at physiological relevant densities, information not accessible with confocal microscopy due to the high packing density of proteins and lipids. The inter image nnd that we found are well below the confocal resolution. In combination with the high packing densities NSOM is therefore crucial to determine the true correlation of proteins and lipids positions.

When using a confocal microscope to study the association between lipids and proteins, co-patching is needed to form domains that are visible at confocal resolution. However, the use of patching will enhance the possibility of signaling, resulting in a redistribution of membrane components [35, 150]. Since both lipid and proteins domains are small, upon patching artificial co-clustering might occur if lipid and proteins are in close proximity. Co-patching is not required in NSOM experiments, thus patching artifacts are absent in NSOM images. An interesting experiment would be to use NSOM to investigate the co-localization on stretched cells using antibody patching to assess the extent of patching induced association. However, on stretched cells patching has not been successful (results not shown), probably due to the reduced mobility of membrane components through cell adherence to the PLL coated coverslip.

Another difference between both experiments is that for NSOM experiments well stretched cells have been used, while for confocal patching studies the cells were only mildly adhering to the glass substrate. As a result, the membrane fraction from which fluorescence is detected in confocal is larger than the membrane fraction illuminated with the near-field probe on well stretched cells. Especially in combination with a high expression level of proteins and a dense lipid packing, this could cause artificial high co-localization coefficients when performing confocal experiments.

An additional source for artifacts when using confocal microscopy is the effect of surface topology in combination with a high packing density. This could give rise to a staining pattern resembling full co-localization after patching. This effect has been reported by Bacia and co-workers [40]. From confocal images authors identified significant co-localization between two markers (DiI and GM1), but FCS experiments revealed completely different mobility, indicating that the markers did not participate in the same environment. The advantage of NSOM is that besides fluorescence information, simultaneously the cell topography is obtained. Any potential artifact can be excluded if correlation between topography and fluorescence signal is absent.

Finally, an alternative possibility for the lack of co-localization might be lipid diffusion after fixation. If proteins are properly fixed, but lipids remain mobile,

real associations will vanish over time. The higher the imaging resolution the faster the co-localization between lipids and proteins will be lost. In fact the inter-image nnd analysis revealed a significant shift to lower values for both CD55 and LFA-1, indicating that these proteins could have been initially associated to lipid rafts. Assuming an initial correlation between GM1 lipids and protein position of 1, we calculate that a random shift of the lipids over ~ 250 nm (see Figure 6.1 **C**) would be sufficient to obtain nnd values similar to those obtained for LFA-1 and CD55. Since experiments were performed several days after fixation, this would indicate a very low diffusion coefficient. However, using FRAP we determined that only 10% of the lipids remain mobile with a diffusion speed of 0.01 $\mu m^2/s$. There are 2 times more GM1 spots as LFA-1 spots and 3.5 times more GM1 spots as CD55 spots. Suppose the mobile GM1 fraction of 10% was fully associated to either LFA-1 or CD55. If there are 350 GM1 spots, 35 of these spots are associated to LFA-1 or CD55. Indicating that 20% of the LFA-1 and 35% of the CD55 spots fully coincide with GM1. This would result in a correlation coefficient before fixation of 0.2 or 0.35 for LFA-1 and CD55 respectively, in contrast to the high co-localization found using co-patching (C=0.62 for LFA-1). Clearly, this small mobile fraction is not able to explain the low C values found in our experiments, even if one assumes that this fraction was initially fully associated to CD55 or LFA-1. This indicates that the true association to rafts is in fact very small. Nevertheless, one has to be aware that confocal FRAP is not capable of monitoring sub diffraction limit displacements.

Despite the lack of association between GM1 and CD55 or LFA-1, we have measured a significant shift of the inter image nnd to lower values for both LFA-1 and CD55. These results strongly suggest a pre-disposition of these proteins to be in the close proximity to the lipids. Our hypothesis for the possible role of the lipid-protein proximity is that the lipid domains are needed to stabilize larger domains or contain additional proteins, which upon activation might be needed to form functional complexes. The proximity can facilitate and accelerate complex formation. This might explain the vast amount of functions related to lipid rafts [24–28] while in fact the underlying processes are protein mediated. For example there is accumulating evidence that many integrin associated processes are activated through interaction between integrins and other proteins in the cell membrane [151]. On the other hand, it could well be that since most functional protein-raft associations are derived from experiments based on either DRM assays or confocal co-patching experiments, in fact no real associations i.e., direct protein-lipid interactions are present, but observed co-partitioning is rather the result of a similar proximity effect.

A point of concern is that steric hindrance of the antibody labelling effects the

co-localization results we observed. Since the primary and secondary antibodies can occupy a $\sim$ 20 nm radius area [113] around the protein, CTxB binding to lipids in the direct vicinity of the proteins could be prevented. For transmembrane proteins this issue can be solved in future experiments by labeling the cytoplasmic tail of the protein via GFP.

6.5 Conclusion

In this chapter we have shown that high resolution near-field scanning optical microscopy is perfectly suited to perform chromatic aberration free co-localization studies on cells in liquid conditions. The high spatial resolution of NSOM enables the direct and simultaneous visualization of lipid and protein domains. To determine the extent of co-localization between lipids and proteins we calculated Pearssons's correlation coefficient for both confocal and NSOM images. Interestingly, co-localization observed using confocal co-patching could not be reproduced upon direct NSOM investigation.

To assess the influence of lipid mobility on the NSOM co-localization results, FRAP experiments were performed on fixed THP1 cells revealing a small mobile fraction of GM1 ($\sim$10%). However this fraction is not sufficient to explain the differences in co-localization between confocal co-patching and NSOM observed in our experiments on imDC and THP1. These high resolution NSOM experiments provide clear evidence that lipid-protein associations based on confocal co-patching experiments are in fact artificial. The potential nano-scale spatial proximity of CD71,CD55 and LFA-1 to the raft marker GM1 was investigated using inter particle nearest neighbor distance (nnd) analysis. The CD71 spot positions are not related to the GM1 spot positions, consistent with the fact that CD71 is a non-raft associated protein. In contrast, the nnd distributions of CD55-GM1 and LFA-1-GM1 are significantly shifted to shorter distances compared to random organization. These results indicate a statistical relevant preference for LFA-1 and CD55 to be in the close neighborhood of lipid rafts. Altogether, our results are consistent with a model where both proteins and lipids are pre-organized into small separate nanoscale domains. The functional role of these nanodomains might the facilitation and acceleration of the formation of larger functional domains.

Chapter 7

General discussion and outlook

This thesis described the implementation of a diving bell concept to allow high resolution NSOM imaging in liquid conditions. Using this technique it was for the first time possible to visualize nanometer sized lipid and protein domains on both immature dendritic cells and THP1 cells in liquid. In this chapter the future of NSOM imaging will be discussed as well as the implications of our results for the current picture of cell membrane organization.

7.1 NSOM technology

At present NSOM is a unique technique that works in liquid conditions and provides an imaging resolution of 100 nm or better over the whole visible spectrum. As demonstrated in this thesis high resolution information concerning protein and lipid organization in cell membranes of different cell types can be reproducibly obtained. In this section the general applicability of NSOM will be discussed together with possible improvements and future applications.

NSOM resolution is dependent on both probe-sample distance and probe size, thus high resolution information can only be obtained from objects that are placed directly below the probe aperture. In a biological context this limits the application of NSOM to individual cell membranes or cell components that are isolated from their environment like nuclear membranes [88] or isolated chromosomes [152]. For imaging cell membranes, the more stretched and less flexible the membrane, the less demanding the sample is for the feedback system that regulates probe-sample distance. Therefore, the ideal cell for NSOM imaging is well stretched in combination with a relatively stiff membrane. Obviously, fixed cells membranes are less flexible than membranes of living cells. For liver endothelial cells a ratio of 50 in the elastic modulus between fixed and living cells has been

reported [153]. The tuning fork feedback system in combination with the diving bell provides enough sensitivity to measure on such soft cells and is therefore compatible with live cell imaging. The most critical part in live cell imaging will probably be a stable temperature control at 37 ^{o}C, since small fluctuations in temperature will influence the tuning fork force feedback mechanism. To this end we recommend the use of an objective heater in combination with a sample heater to minimize temperature gradients.

Since NSOM is a scanning probe technique it is inherently slow, being less suitable to monitor surface dynamics of membrane complexes. On the other hand, its excellent depth resolution should allow for the monitoring of exo-and endocytosis processes with high speed and sensitivity. Similarly, the technique could be used in a fluorescence correlation spectroscopy (FCS) configuration, where the nanometric excitation volume (1000 times smaller than for confocal microscopy) allows to probe slow diffusion not accessible with confocal FCS [40].

NSOM requires highly trained operators and due to its complex operation the technique is not suited for extensive cell screening. The best solution is therefore to use NSOM in combination with other techniques. Ideally after an initial high throughput screening using flow cytometry, cells are characterized in more detail using confocal fluorescence microscopy to assess the variability within the cell population and finally a chosen subset of the population can be investigated in detail with the NSOM. Though the emphasis of most research projects is on working with living cells, one should realize that investigating fixed membranes at high resolution can still reveal dynamic information. Samples can be fixed at different stages during development, thus providing snap-shots of the real dynamic picture. For example a snap-shot that reveals protein domains on the cell membrane in fact maps the entire process of formation, existence and degradation of domains at the moment of fixation. With extensive data analysis in combination with computer simulations such 'dynamic' information can still be extracted from still images.

Since the resolution of NSOM is dependent on the aperture size of the probe, the smaller the aperture the better the imaging resolution. The aperture probes used in this thesis were produced via fibre pulling and subsequent metal coating. The smallest apertures that could be obtained where $\sim$ 70 nm in diameter. The throughput of smaller apertures is generally too low to efficiently excite the sample. Imaging resolution can be further enhanced if a strongly confined optical field is created at the end of a sharp probe. In this context a metal nano-antenna placed on the endface of a conventional aperture probe has recently demonstrated single molecule detection with 10 nm resolution [154]. Use of these nano-antenna tips in our liquid NSOM appears a promising approach to resolve the internal

lipid or protein domain structure.

Another promising technique that is capable to obtain an imaging resolution well below the diffraction limit of light is stimulated emission depletion (STED) microscopy [155]. This technique requires a precise control over the spatial and temporal position of two picosecond laser pulses and a STED experiment is therefore still expensive and hard to reproduce especially when working with cells. Recently a new form of STED using reversible photoswitchable proteins was demonstrated for low intensity saturating conditions [156]. This might reduce the phototoxic effects, currently hampering application of STED to image living cells.

7.2 Membrane microdomains

In this section we briefly summarize our findings concerning lipid and protein domains in the cell plasma membrane obtained using NSOM with single molecules sensitivity in liquid conditions and discuss the implications for membrane microdomain research.

GM1 lipids organize in domains with sizes around 10-40 nm. On THP1 cells these domains contain on average 20-30 lipids, indicated by the binding of 5 to 6 CTxB molecules. If the overall GM1 content in the membrane is decreased, GM1 content in the lipid raft domains decreases as well as the total number of domains. Furthermore the surface organization of different proteins, with or without association to lipid rafts has been investigated. The results demonstrate that classification as lipid raft associated does not give a priori information on surface arrangement, i.e. lipid raft partitioning does not necessarily imply clustering and clustering is not *per se* maintained by lipid rafts. Direct correlation of lipid and protein organization by means of co-localization analysis revealed that the spatial correlation, as observed using confocal co-patching, can not be reproduced using direct NSOM investigation. A nearest neighbor distance (nnd) analysis however indicates a statistically relevant preference for some proteins (LFA-1 and CD55 on THP1 cells) to be in the close neighborhood of lipid rafts.

Several models have currently been proposed in literature by different groups. Mayor and co-workers propose that large scale rafts are actively induced from small lipid-protein assemblies [44], based on the observation of small GPI clusters using FRET. Kenworthy and co-workers [5] discussed the possibility of stable, immobile rafts; stable mobile rafts; dynamic partitioning or no rafts. Since fluorescent recovery after photobleaching (FRAP) experiments revealed that raft association is not the major determinant of protein diffusional mobility, the first two models were excluded. Our observations also exclude these models due to

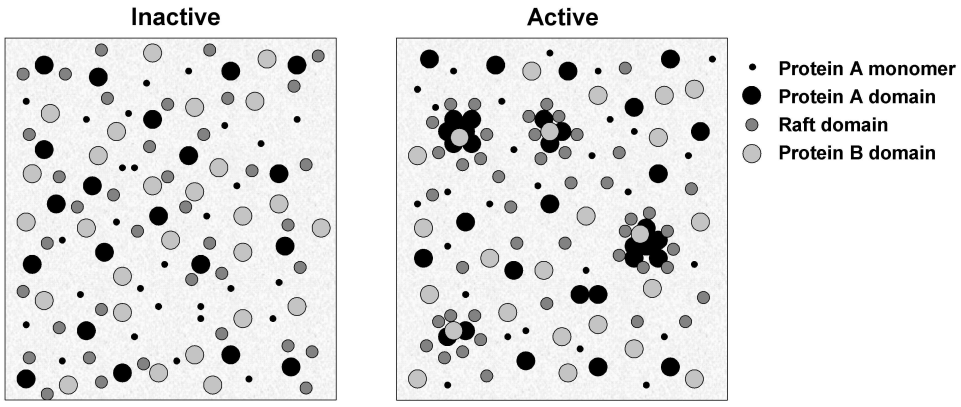

Figure 7.1: A model for cell membrane organization. In an inactive state small lipid and protein domains co-exist with monomers in the cell membrane. Upon activation larger protein domains are formed and stabilized by lipid rafts.

the lack of co-localization between GM1 domains and the proteins postulated to associate to these domains. The FRAP experiments presented in the Kenworthy paper were not sufficient to discriminate between a dynamic partitioning model and a model in which rafts are absent. In contrast we were able to directly visualize lipid and protein domains, suggesting that lipid rafts do indeed exist in the cell plasma membrane. In contrast to the model proposed by Mayor we do not find a direct association of GPI and GM1. However, we do observe a proximity effect for CD55 (GPI family member) and LFA-1 to GM1 and therefor propose a model in which both proteins and lipids are pre-organized into small separate nanoscale domains, where these nanodomains might function as cell membrane organizers that facilitate and accelerate the formation of larger functional domains. This model is illustrated in Figure 7.1. In this context it would be interesting to investigate if these nanodomains are involved in the formation of larger complexes upon cell stimulation and activation.

Still our results do not prove that lipid rafts are truly needed as organizers for protein complexes. In fact, lipid rafts in the form of GM1 rich domains are not the dominant factor in protein domain formation and maintenance for CD46 and DC-SIGN on imDC and LFA1 on THP1. Our results do reveal that the cell plasma membrane is far from homogeneous and that lipids and proteins organize into small nanometer sized domains. In general the biological function of these small domains remains to be established. More specific, for DC-SIGN on imDCs domain formation enhances the efficiency to bind to viral particles [59].

For LFA-1, the LFA-1 mediated binding to ICAM-1 is completely lost during development of monocyte derived immature DCs. The lack of binding coincides with the exclusion of LFA-1 molecules from microdomains [76], suggesting that LFA-1 domains are needed for efficient ligand binding. For CD46, currently there has not been reported a direct relation between domain formation and cell function. There is accumulating evidence that many integrin associated processes are activated through interaction between integrins and other proteins in the cell membrane [151]. Lipid rafts could provide platforms for the recruitment of these functional complexes. On the other hand other membrane components like tetraspanins can perform a similar function.

For further experiments it is important to realize that neither detergent resistant membrane experiments nor confocal co-patching give reliable information concerning lipid raft association. If research is focussed on cell function, in our opinion it is more important and insightful to directly investigate protein-protein associations. Domain formation should be investigated as a separate mechanism without too much emphasis on the presence of lipid rafts. Along these lines the paper by Douglass and co-workers [38] recently demonstrated the importance of protein-protein interactions in creating microdomains and facilitating T-cell signalling. NSOM in liquid can in future experiments be used as an important tool to investigate protein-protein associations in densely populated cell membranes with superior spatial resolution.

Bibliography

[1] S. J. Singer and G. L. Nicolson, *The fluid mosaic model of the structure of cell membranes*, Science **175**, 720 (1972).

[2] K. Jacobson, E. Sheets, and R. Simson, *Revisiting the fluid mosaic model of membranes.*, Science **268**, 1441 (1995).

[3] F. R. Maxfield, *Plasma membrane microdomains.*, Curr Opin Cell Biol **14**, 483 (2002).

[4] M. Edidin, *Lipids on the frontier: a century of cell-membrane bilayers.*, Nat Rev Mol Cell Biol **4**, 414 (2003).

[5] A. K. Kenworthy, B. J. Nichols, C. L. Remmert, G. M. Hendrix, M. Kumar, J. Zimmerberg, and J. Lippincott-Schwartz, *Dynamics of putative raft-associated proteins at the cell surface.*, J Cell Biol **165**, 735 (2004).

[6] P. Sharma, R. Varma, R. Sarasij, R. Ira, K. Gousset, G. Krishnamoorthy, M. Rao, and S. Mayor, *Nanoscale organization of multiple GPI-anchored proteins in living cell membranes.*, Cell **116**, 577 (2004).

[7] B. Razani, S. E. Woodman, and M. P. Lisanti, *Caveolae: from cell biology to animal physiology.*, Pharmacol Rev **54**, 431 (2002).

[8] S. Charrin, S. Manié, M. Billard, L. Ashman, D. Gerlier, C. Boucheix, and E. Rubinstein, *Multiple levels of interactions within the tetraspanin web.*, Biochem Biophys Res Commun **304**, 107 (2003).

[9] S. Levy and T. Shoham, *The tetraspanin web modulates immune-signalling complexes.*, Nat Rev Immunol **5**, 136 (2005).

[10] C. Dietrich, B. Yang, T. Fujiwara, A. Kusumi, and K. Jacobson, *Relationship of lipid rafts to transient confinement zones detected by single particle tracking.*, Biophys. J. **82**, 274 (2002).

[11] C. Nakada, K. Ritchie, Y. Oba, M. Nakamura, Y. Hotta, R. Iino, R. S. Kasai, K. Yamaguchi, T. Fujiwara, and A. Kusumi, *Accumulation of anchored proteins forms membrane diffusion barriers during neuronal polarization.*, Nat Cell Biol **5**, 626 (2003).

[12] A. Kusumi, H. Ike, C. Nakada, K. Murase, and T. Fujiwara, *Single-molecule tracking of membrane molecules: plasma membrane compartmentalization*

and dynamic assembly of raft-philic signaling molecules., Semin Immunol **17**, 3 (2005).

[13] M. Edidin, *Lipid microdomains in cell surface membranes.*, Curr Opin Struct Biol **7**, 528 (1997).

[14] K. Jacobson and C. Dietrich, *Looking at lipid rafts?*, Trends Cell Biol **9**, 87 (1999).

[15] G. Vereb, J. Szollosi, J. Matko, P. Nagy, T. Farkas, L. Vigh, L. Matyus, T. A. Waldmann, and S. Damjanovich, *Dynamic, yet structured: The cell membrane three decades after the Singer-Nicolson model*, PNAS **100**, 8053 (2003).

[16] G. van Meer, *Lipid traffic in animal cells.*, Annu Rev Cell Biol **5**, 247 (1989).

[17] W. H. Binder, V. Barragan, and F. M. Menger, *Domains and rafts in lipid membranes.*, Angew Chem Int Ed Engl **42**, 5802 (2003).

[18] H. Ohvo-Rekilä, B. Ramstedt, P. Leppimäki, and J. P. Slotte, *Cholesterol interactions with phospholipids in membranes.*, Prog Lipid Res **41**, 66 (2002).

[19] J. Ipsen, G. Karlström, O. Mouritsen, H. Wennerström, and M. Zuckermann, *Phase equilibria in the phosphatidylcholine-cholesterol system.*, Biochim Biophys Acta **905**, 162 (1987).

[20] X. Li, M. Momsen, J. Smaby, H. Brockman, and R. Brown, *Cholesterol decreases the interfacial elasticity and detergent solubility of sphingomyelins.*, Biochemistry **40**, 5954 (2001).

[21] B. Ramstedt and J. P. Slotte, *Membrane properties of sphingomyelins.*, FEBS Lett **531**, 33 (2002).

[22] J. R. Silvius, *Partitioning of membrane molecules between raft and non-raft domains: Insights from model-membrane studies.*, Biochim Biophys Acta (2005).

[23] K. Simons and E. Ikonen, *Functional rafts in cell membranes.*, Nature **387**, 569 (1997).

[24] K. Simons and R. Ehehalt, *Cholesterol, lipid rafts, and disease.*, J Clin Invest **110**, 597 (2002).

[25] S. Manes, G. del Real, and C. Martínez-A, *Pathogens: raft hijackers.*, Nat. Rev. Immunol. **3**, 557 (2003).

[26] R. G. Parton and A. A. Richards, *Lipid rafts and caveolae as portals for endocytosis: new insights and common mechanisms.*, Traffic **4**, 724 (2003).

[27] C. Salaün, D. J. James, and L. H. Chamberlain, *Lipid rafts and the regulation of exocytosis.*, Traffic **5**, 255 (2004).

[28] J. B. Helms and C. Zurzolo, *Lipids as targeting signals: lipid rafts and*

intracellular trafficking., Traffic **5**, 247 (2004).

[29] S. Munro, *Lipid rafts: elusive or illusive?*, Cell **115**, 377 (2003).

[30] M. Edidin, *The state of lipid rafts: from model membranes to cells.*, Annu. Rev. Biophys. Biomol. Struct. **32**, 257 (2003).

[31] D. Brown and E. London, *Structure of detergent-resistant membrane domains: does phase separation occur in biological membranes?*, Biochem Biophys Res Commun **240**, 1 (1997).

[32] R. Schroeder, S. Ahmed, Y. Zhu, E. London, and D. Brown, *Cholesterol and sphingolipid enhance the Triton X-100 insolubility of glycosylphosphatidylinositol-anchored proteins by promoting the formation of detergent-insoluble ordered membrane domains.*, J Biol Chem **273**, 1150 (1998).

[33] S. Schuck, M. Honsho, K. Ekroos, A. Shevchenko, and K. Simons, *Resistance of cell membranes to different detergents.*, Proc Natl Acad Sci U S A **100**, 5795 (2003).

[34] M. Edidin, *Near-field scanning optical microscopy, a siren call to biology.*, Traffic **2**, 797 (2001).

[35] K. Simons and D. Toomre, *Lipid rafts and signal transduction.*, Nat. Rev. Mol. Cell Biol. **1**, 31 (2000).

[36] A. Fra, E. Williamson, K. Simons, and R. Parton, *Detergent-insoluble glycolipid microdomains in lymphocytes in the absence of caveolae.*, J. Biol. Chem. **269**, 30745 (1994).

[37] R. G. W. Anderson and K. Jacobson, *A role for lipid shells in targeting proteins to caveolae, rafts, and other lipid domains.*, Science **296**, 1821 (2002).

[38] A. D. Douglass and R. D. Vale, *Single-molecule microscopy reveals plasma membrane microdomains created by protein-protein networks that exclude or trap signaling molecules in T cells.*, Cell **121**, 937 (2005).

[39] B. C. Lagerholm, G. E. Weinreb, K. Jacobson, and N. L. Thompson, *Detecting microdomains in intact cell membranes.*, Annu Rev Phys Chem **56**, 309 (2005).

[40] K. Bacia, D. Scherfeld, N. Kahya, and P. Schwille, *Fluorescence correlation spectroscopy relates rafts in model and native membranes.*, Biophys. J. **87**, 1034 (2004).

[41] M. Saxton and K. Jacobson, *Single-particle tracking: applications to membrane dynamics.*, Annu Rev Biophys Biomol Struct **26**, 373 (1997).

[42] A. Kenworthy, *Imaging protein-protein interactions using fluorescence resonance energy transfer microscopy.*, Methods **24**, 289 (2001).

[43] O. O. Glebov and B. J. Nichols, *Lipid raft proteins have a random distri-*

bution during localized activation of the T-cell receptor., Nat Cell Biol **6**, 238 (2004).

[44] S. Mayor and M. Rao, *Rafts: scale-dependent, active lipid organization at the cell surface.*, Traffic **5**, 231 (2004).

[45] B. Wilson, S. Steinberg, K. Liederman, J. Pfeiffer, Z. Surviladze, J. Zhang, L. Samelson, L. Yang, P. Kotula, and J. Oliver, *Markers for detergent-resistant lipid rafts occupy distinct and dynamic domains in native membranes.*, Mol. Biol. Cell **15**, 2580 (2004).

[46] E. Betzig and R. J. Chichester, *Single molecules observed by near-field scanning optical microscopy*, Science **262**, 1422 (1993).

[47] T. Laurence and S. Weiss, *Analytical chemistry. How to detect weak pairs.*, Science **299**, 667 (2003).

[48] F. de Lange, A. Cambi, R. Huijbens, B. de Bakker, W. Rensen, M. Garcia-Parajo, N. van Hulst, and C. Figdor, *Cell biology beyond the diffraction limit: near-field scanning optical microscopy.*, J. Cell Sci. **114**, 4153 (2001).

[49] M. Garcia-Parajo, B. de Bakker, M. Koopman, A. Cambi, F. de Lange, C. Figdor, and N. van Hulst, *Near-field fluorescence microscopy and optical nanotool to study protein organization at the cell membrane*, Nanobiotechnology **1**, 113 (2005).

[50] M. Paesler and P. Moyer, *Near-field optics, theory, instrumentation and applications* (Wiley-Interscience, New York, 1996).

[51] P. Lambelet, M. Pfeffer, A. Sayah, and F. Marquis-Weible, *Reduction of tip-sample interaction forces for scanning near-field optical microscopy in a liquid environment*, Ultramicroscopy **71**, 117 (1998).

[52] R. Brunner, O. Hering, O. Marti, and O. Hollricher, *Piezoelectrical shear-force control on soft biological samples in aqueous solution*, Appl. Phys. Lett. **71**, 3628 (1997).

[53] W. H. J. Rensen, N. F. van Hulst, and S. B. Kammer, *Imaging soft samples in liquid with tuning fork based shear force microscopy*, Appl. Phys. Lett. **77**, 1557 (2000).

[54] L. F. Lee, R. D. Schaller, L. H. Haber, and R. J. Saykally, *High spatial resolution imaging with near-field scanning optical microscopy in liquids*, Anal. Chem. **73**, 5015 (2001).

[55] C. Höppener, D. Molenda, H. Fuchs, and A. Naber, *Scanning near-field optical microscopy of a cell membrane in liquid*, Journal of Microscopy **210**, 288 (2003).

[56] J. E. Shaw, R. F. Epand, R. M. Epand, Z. Li, R. Bittman, and C. M. Yip, *Correlated fluorescence-AFM microscopy of membrane domains: Structure of fluorescence probes determines lipid localization.*, Biophys J (2005).

[57] P. Burgos, C. Yuan, M. Viriot, and L. Johnston, *Two-color near-field fluorescence microscopy studies of microdomains ("Rafts") in model membranes*, Langmuir **19**, 8002 (2003).

[58] A. D. Stuart, H. E. Eustace, T. A. McKee, and T. D. K. Brown, *A novel cell entry pathway for a DAF-using human enterovirus is dependent on lipid rafts.*, J Virol **76**, 9307 (2002).

[59] A. Cambi, F. de Lange, N. van Maarseveen, M. Nijhuis, B. Joosten, E. van Dijk, B. de Bakker, J. Fransen, P. Bovee-Geurts, F. van Leeuwen, N. V. Hulst, and C. Figdor, *Microdomains of the C-type lectin DC-SIGN are portals for virus entry into dendritic cells.*, J. Cell Biol. **164**, 145 (2004).

[60] M. Vrljic, S. Nishimura, S. Brasselet, W. Moerner, and H. McConnell, *Translational diffusion of individual class II MHC membrane proteins in cells.*, Biophys J **83**, 2681 (2002).

[61] A. Pralle, P. Keller, E. Florin, K. Simons, and J. Hrber, *Sphingolipid-cholesterol rafts diffuse as small entities in the plasma membrane of mammalian cells.*, J Cell Biol **148**, 997 (2000).

[62] A. Kenworthy, N. Petranova, and M. Edidin, *High-resolution FRET microscopy of cholera toxin B-subunit and GPI-anchored proteins in cell plasma membranes.*, Mol Biol Cell **11**, 1645 (2000).

[63] T. Harder, P. Scheiffele, P. Verkade, and K. Simons, *Lipid domain structure of the plasma membrane revealed by patching of membrane components.*, J. Cell Biol. **141**, 929 (1998).

[64] B. Nichols, *GM1-containing lipid rafts are depleted within clathrin-coated pits.*, Curr Biol **13**, 686 (2003).

[65] J. Banchereau and R. Steinman, *Dendritic cells and the control of immunity.*, Nature **392**, 245 (1998).

[66] T. Geijtenbeek, R. Torensma, S. van Vliet, G. van Duijnhoven, G. Adema, Y. van Kooyk, and C. Figdor, *Identification of DC-SIGN, a novel dendritic cell-specific ICAM-3 receptor that supports primary immune responses.*, Cell **100**, 575 (2000a).

[67] T. Geijtenbeek, D. Krooshoop, D. Bleijs, S. van Vliet, G. van Duijnhoven, V. Grabovsky, R. Alon, C. Figdor, and Y. van Kooyk, *DC-SIGN-ICAM-2 interaction mediates dendritic cell trafficking*, Nat. Immunol. **1**, 353 (2000).

[68] C. V. Carman and T. A. Springer, *Integrin avidity regulation: are changes in affinity and conformation underemphasized?*, Curr Opin Cell Biol **15**, 547 (2003).

[69] M. Dustin and T. Springer, *T-cell receptor cross-linking transiently stimulates adhesiveness through LFA-1.*, Nature **341**, 619 (1989).

[70] A. Grakoui, S. Bromley, C. Sumen, M. Davis, A. Shaw, P. Allen, and M.

Dustin, *The immunological synapse: a molecular machine controlling T cell activation.*, Science **285**, 221 (1999).

[71] M. Lub, Y. van Kooyk, and C. Figdor, *Ins and outs of LFA-1.*, Immunol Today **16**, 479 (1995).

[72] Y. van Kooyk, P. van de Wiel-van Kemenade, P. Weder, T. Kuijpers, and C. Figdor, *Enhancement of LFA-1-mediated cell adhesion by triggering through CD2 or CD3 on T lymphocytes.*, Nature **342**, 811 (1989).

[73] M. Shimaoka, T. Xiao, J.-H. Liu, Y. Yang, Y. Dong, C.-D. Jun, A. McCormack, R. Zhang, A. Joachimiak, J. Takagi, J.-H. Wang, and T. A. Springer, *Structures of the alpha L I domain and its complex with ICAM-1 reveal a shape-shifting pathway for integrin regulation.*, Cell **112**, 99 (2003).

[74] Y. van Kooyk, S. van Vliet, and C. Figdor, *The actin cytoskeleton regulates LFA-1 ligand binding through avidity rather than affinity changes.*, J Biol Chem **274**, 26869 (1999).

[75] Y. van Kooyk, P. Weder, K. Heije, and C. Figdor, *Extracellular Ca2+ modulates leukocyte function-associated antigen-1 cell surface distribution on T lymphocytes and consequently affects cell adhesion.*, J Cell Biol **124**, 1061 (1994).

[76] A. Cambi, *Microdomains in the immune system control cell adhesion and pathogen uptake*, Ph.D. thesis, Radboud University Medical Centre, 2005.

[77] S. T. Hess, M. Kumar, A. Verma, J. Farrington, A. Kenworthy, and J. Zimmerberg, *Quantitative electron microscopy and fluorescence spectroscopy of the membrane distribution of influenza hemagglutinin.*, J Cell Biol **169**, 965 (2005).

[78] I. Prior, C. Muncke, R. Parton, and J. Hancock, *Direct visualization of Ras proteins in spatially distinct cell surface microdomains.*, J. Cell Biol. **160**, 165 (2003).

[79] D. J. Stephens and V. J. Allan, *Light microscopy techniques for live cell imaging*, Science **300**, 82 (2003).

[80] Y. Sako and T. Yanagida, *Single-molecule visualization in cell biology*, Nature Cell Biology **Suppl. S.**, SS1 (2003).

[81] G. Schütz, G. Kada, V. Pastushenko, and H. Schindler, *Properties of lipid microdomains in a muscle cell membrane visualized by single molecule microscopy.*, EMBO J **19**, 892 (2000).

[82] S. W. Hell, *Toward fluorescence nanoscopy*, Nature Biotechnology **21**, 1347 (2003).

[83] V. Westphal, C. M. Blanca, M. Dyba, L. Kastrup, and S. W. Hell, *Laser-diode-stimulated emission depletion microscopy*, Appl. Phys. Lett. **82**, 3125 (2003).

[84] M. Dyba, S. Jakobs, and S. W. Hell, *Immunofluorescence stimulated emission depletion microscopy.*, Nat Biotechnol **21**, 1303 (2003).

[85] T. Enderle, T. Ha, D. Ogletree, D. Chemla, C. Magowan, and S. Weiss, *Membrane specific mapping and colocalization of malarial and host skeletal proteins in the Plasmodium falciparum infected erythrocyte by dual-color near-field scanning optical microscopy.*, Proc. Natl. Acad. Sci. U S A **94**, 520 (1997).

[86] J. Hwang, L. Gheber, L. Margolis, and M. Edidin, *Domains in cell plasma membranes investigated by near-field scanning optical microscopy.*, Biophys. J. **74**, 2184 (1998).

[87] P. Nagy, L. Mátyus, A. Jenei, G. Panyi, S. Varga, J. Matkó, J. Szöllosi, R. Gáspár, T. Jovin, and S. Damjanovich, *Cell fusion experiments reveal distinctly different association characteristics of cell-surface receptors.*, J. Cell Sci. **114**, 4063 (2001).

[88] C. Höppener, J. Siebrasse, R. Peters, U. Kubitscheck, and A. Naber, *High-resolution near-field optical imaging of single nuclear pore complexes under physiological conditions.*, Biophys J **88**, 3681 (2005).

[89] A. Ianoul, M. Street, D. Grant, J. Pezacki, R. Taylor, and L. Johnston, *Near-field scanning fluorescence microscopy study of ion channel clusters in cardiac myocyte membranes.*, Biophys J **87**, 3525 (2004).

[90] A. Ianoul, D. Grant, Y. Rouleau, M. Bani-Yaghoub, L. Johnston, and J. Pezacki, *Imaging nanometer domains of beta-adrenergic receptor complexes on the surface of cardiac myocytes*, Nature Chemical Biology **1**, 196 (2005).

[91] B. I. de Bakker, *Single molecule detection on the cell membrane with near-field scanning optical microscopy*, Ph.D. thesis, University of Twente, 2004.

[92] H. Ris, *The cytoplasmic filament system in critical point-dried whole mounts and plastic-embedded sections.*, J Cell Biol **100**, 1474 (1985).

[93] K. Karrai and R. D. Grober, *Piezoelectric tip-sample distance control for near-field optical microscopes*, Appl. Phys. Lett. **66**, 1842 (1995).

[94] W. H. J. Rensen, N. F. van Hulst, A. G. T. Ruiter, and P. E. West, *Atomic steps with tuning-fork-based noncontact atomic force microscopy*, Appl. Phys. Lett. **75**, 1640 (1999).

[95] A. G. T. Ruiter, J. A. Veerman, K. O. van der Werf, and N. F. van Hulst, *Dynamic behavior of tuning fork shear-force feedback*, Appl. Phys. Lett. **71**, 28 (1997).

[96] A. G. T. Ruiter, K. O. van der Werf, J. A. Veerman, M. F. Garcia-Parajo, W. H. J. Rensen, and N. F. van Hulst, *Tuning fork shear-force feedback*, Ultramicroscopy **71**, 149 (1998).

[97] J. Tamayo, A. D. L. Humphris, and M. J. Miles, *Piconewton regime dy-*

namic force microscopy in liquid, Appl. Phys. Lett. **77**, 582 (2000).

[98] T. Geijtenbeek, D. Kwon, R. Torensma, S. van Vliet, G. van Duijnhoven, J. Middel, I. Cornelissen, H. Nottet, V. KewalRamani, D. Littman, C. Figdor, and Y. van Kooyk, *DC-SIGN, a dendritic cell-specific HIV-1-binding protein that enhances trans-infection of T cells.*, Cell **100**, 587 (2000b).

[99] M. Dykstra, A.C., H. Sohn, S.T., and S. Pierce, *Location is everything: lipid rafts and immune cell signaling.*, Annu Rev Immunol **21**, 457 (2003).

[100] C. Dietrich, Z. Volovyk, M. Levi, N. Thompson, and K. Jacobson, *Partitioning of Thy-1, GM1, and cross-linked phospholipid analogs into lipid rafts reconstituted in supported model membrane monolayers.*, Proc Natl Acad Sci U S A **98**, 10642 (2001).

[101] D. Brown and J. Rose, *Sorting of GPI-anchored proteins to glycolipid-enriched membrane subdomains during transport to the apical cell surface.*, Cell **68**, 533 (1992).

[102] H. Heerklotz, *Triton promotes domain formation in lipid raft mixtures.*, Biophys. J. **83**, 2693 (2002).

[103] P. H. M. Lommerse, H. Spaink, and T. Schmidt, *In vivo plasma membrane organization: results of biophysical approaches.*, Biochim Biophys Acta **1664**, 119 (2004).

[104] T. Fujiwara, K. Ritchie, H. Murakoshi, K. Jacobson, and A. Kusumi, *Phospholipids undergo hop diffusion in compartmentalized cell membrane.*, J Cell Biol **157**, 1071 (2002).

[105] E. Sheets, G. Lee, R. Simson, and K. Jacobson, *Transient confinement of a glycosylphosphatidylinositol-anchored protein in the plasma membrane.*, Biochemistry **36**, 12449 (1997).

[106] P. H. M. Lommerse, G. A. Blab, L. Cognet, G. S. Harms, B. E. Snaar-Jagalska, H. P. Spaink, and T. Schmidt, *Single-molecule imaging of the H-ras membrane-anchor reveals domains in the cytoplasmic leaflet of the cell membrane.*, Biophys J **86**, 609 (2004).

[107] M. Koopman, A. Cambi, B. de Bakker, B. Joosten, C. Figdor, N. van Hulst, and M. Garcia-Parajo, *Near-field scanning optical microscopy in liquid for high resolution single molecule detection on dendritic cells.*, FEBS Lett. **573**, 6 (2004).

[108] P. Fishman, *Role of membrane gangliosides in the binding and action of bacterial toxins.*, J Membr Biol **69**, 85 (1982).

[109] A. Aman, S. Fraser, E. Merritt, C. Rodigherio, M. Kenny, M. Ahn, W. Hol, N. Williams, W. Lencer, and T. Hirst, *A mutant cholera toxin B subunit that binds GM1- ganglioside but lacks immunomodulatory or toxic activity.*, Proc Natl Acad Sci U S A **98**, 8536 (2001).

[110] P. Nagy, G. Vereb, Z. Sebestyén, G. Horváth, S. J. Lockett, S. Damjanovich, J. W. Park, T. M. Jovin, and J. Szllosi, *Lipid rafts and the local density of ErbB proteins influence the biological role of homo- and heteroassociations of ErbB2.*, J Cell Sci **115**, 4251 (2002).

[111] C. E. Miller, J. Majewski, R. Faller, S. Satija, and T. L. Kuhl, *Cholera toxin assault on lipid monolayers containing ganglioside GM(1)*, Biophys. J. **86**, 3700 (2004).

[112] R. G. Zhang, M. L. Westbrook, E. M. Westbrook, D. L. Scott, Z. Otwinowski, P. R. Maulik, R. A. Reed, and G. G. Shipley, *The 2.4 angstrom crystal-structure of cholera-toxin-b subunit pentamer - choleragenoid*, J. Mol. Biol. **251**, 550 (1995).

[113] S. J. Plowman, C. Muncke, R. G. Parton, and J. F. Hancock, *H-ras, K-ras, and inner plasma membrane raft proteins operate in nanoclusters with differential dependence on the actin cytoskeleton.*, Proc Natl Acad Sci U S A **102**, 15500 (2005).

[114] T. Wang and J. Silvius, *Different sphingolipids show differential partitioning into sphingolipid/cholesterol-rich domains in lipid bilayers.*, Biophys J **79**, 1478 (2000).

[115] D. Brown and E. London, *Structure and function of sphingolipid- and cholesterol-rich membrane rafts.*, J Biol Chem **275**, 17221 (2000).

[116] Y. van Kooyk and C. Figdor, *Avidity regulation of integrins: the driving force in leukocyte adhesion.*, Curr Opin Cell Biol **12**, 542 (2000).

[117] F. E. McCann, K. Suhling, L. M. Carlin, K. Eleme, S. B. Taner, K. Yanagi, B. Vanherberghen, P. M. W. French, and D. M. Davis, *Imaging immune surveillance by T cells and NK cells.*, Immunol Rev **189**, 179 (2002).

[118] O. Destaing, F. Saltel, J.-C. Géminard, P. Jurdic, and F. Bard, *Podosomes display actin turnover and dynamic self-organization in osteoclasts expressing actin-green fluorescent protein.*, Mol Biol Cell **14**, 407 (2003).

[119] B. D. Ripley, *Modelling Spatial Patterns*, J. Roy. Stat. Soc. **B39**, 172 (1977).

[120] I. Morrison, C. Anderson, G. Georgiou, G. Stevenson, and R. Cherry, *Analysis of receptor clustering on cell surfaces by imaging fluorescent particles.*, Biophys J **67**, 1280 (1994).

[121] R. Cherry, K. Wilson, K. Triantafilou, P. O'Toole, I. Morrison, P. Smith, and N. Fernndez, *Detection of dimers of dimers of human leukocyte antigen (HLA)-DR on the surface of living cells by single-particle fluorescence imaging.*, J Cell Biol **140**, 71 (1998).

[122] D. Gross and W. Webb, *Molecular counting of low-density lipoprotein particles as individuals and small clusters on cell surfaces.*, Biophys J **49**, 901 (1986).

[123] R. Ghosh and W. Webb, *Automated detection and tracking of individual and clustered cell surface low density lipoprotein receptor molecules.*, Biophys J **66**, 1301 (1994).

[124] N. Petersen, P. Höddelius, P. Wiseman, O. Seger, and K. Magnusson, *Quantitation of membrane receptor distributions by image correlation spectroscopy: concept and application.*, Biophys J **65**, 1135 (1993).

[125] P. Wiseman, P. Höddelius, N. Petersen, and K. Magnusson, *Aggregation of PDGF-beta receptors in human skin fibroblasts: characterization by image correlation spectroscopy (ICS).*, FEBS Lett **401**, 43 (1997).

[126] P. Wiseman and N. Petersen, *Image correlation spectroscopy. II. Optimization for ultrasensitive detection of preexisting platelet-derived growth factor-beta receptor oligomers on intact cells.*, Biophys J **76**, 963 (1999).

[127] A. Nohe and N. O. Petersen, *Analyzing protein-protein interactions in cell membranes.*, Bioessays **26**, 196 (2004).

[128] H. Wallrabe, M. Elangovan, A. Burchard, A. Periasamy, and M. Barroso, *Confocal FRET microscopy to measure clustering of ligand-receptor complexes in endocytic membranes.*, Biophys J **85**, 559 (2003).

[129] T. Schmidt, G. J. Schutz, H. J. Gruber, and H. Schindler, *Local stoichiometries determined by counting individual molecules*, Anal. Chem. **68**, 4397 (1996).

[130] Y. Chen, J. Müller, P. So, and E. Gratton, *The photon counting histogram in fluorescence fluctuation spectroscopy.*, Biophys J **77**, 553 (1999).

[131] J. Müller, Y. Chen, and E. Gratton, *Resolving heterogeneity on the single molecular level with the photon-counting histogram.*, Biophys J **78**, 474 (2000).

[132] Y. Chen, L.-N. Wei, and J. D. Müller, *Probing protein oligomerization in living cells with fluorescence fluctuation spectroscopy.*, Proc Natl Acad Sci U S A **100**, 15492 (2003).

[133] G. Vereb, J. Matko, G. Vamosi, S. M. Ibrahim, E. Magyar, S. Varga, J. Szolossi, A. Jenei, R. J. Gaspar, T. A. Waldmann, and S. Damjanovich, *Cholesterol-dependent clustering of IL-2R alpha and its colocalization with HLA and CD48 on T lymphoma cells suggest their functional association with lipid rafts*, PNAS **97**, 6013 (2000).

[134] M. Faure, D. F. Barber, S. M. Takahashi, T. Jin, and E. O. Long, *Spontaneous clustering and tyrosine phosphorylation of NK cell inhibitory receptor induced by ligand binding.*, J Immunol **170**, 6107 (2003).

[135] B. Wilson, J. Pfeiffer, Z. Surviladze, E. Gaudet, and J. Oliver, *High resolution mapping of mast cell membranes reveals primary and secondary domains of Fc(epsilon)RI and LAT.*, J Cell Biol **154**, 645 (2001).

[136] A. Gaggar, D. M. Shayakhmetov, and A. Lieber, *CD46 is a cellular receptor for group B adenoviruses.*, Nat. Med. **9**, 1408 (2003).

[137] P. O. Vidalain, O. Azocar, C. Servet-Delprat, C. Rabourdin-Combe, D. Gerlier, and S. Manié, *CD40 signaling in human dendritic cells is initiated within membrane rafts.*, EMBO J **19**, 3304 (2000).

[138] R. Varma and S. Mayor, *GPI-anchored proteins are organized in submicron domains at the cell surface.*, Nature **394**, 798 (1998).

[139] A. Kenworthy and M. Edidin, *100 A using imaging fluorescence resonance energy transfer.*, J Cell Biol **142**, 69 (1998).

[140] G. Harms, L. Cognet, P. Lommerse, G. Blab, and T. Schmidt, *Autofluorescent proteins in single-molecule research: applications to live cell imaging microscopy.*, Biophys J **80**, 2396 (2001).

[141] S. Bounou, J.-F. Giguere, R. Cantin, C. Gilbert, M. Imbeault, G. Martin, and M. J. Tremblay, *The importance of virus-associated host ICAM-1 in human immunodeficiency virus type 1 dissemination depends on the cellular context.*, FASEB J **18**, 1294 (2004).

[142] J. F. Hancock and I. A. Prior, *Electron microscopic imaging of Ras signaling domains.*, Methods **37**, 165 (2005).

[143] J. Matko and M. Edidin, *Energy transfer methods for detecting molecular clusters on cell surfaces.*, Methods Enzymol **278**, 444 (1997).

[144] E. Manders, F. Verbeek, and J. Aten, *Measurement of colocalization of objects in dual-color confocal images*, J. Microscopy **169**, 375 (1993).

[145] S. V. Costes, D. Daelemans, E. H. Cho, Z. Dobbin, G. Pavlakis, and S. Lockett, *Automatic and quantitative measurement of protein-protein colocalization in live cells.*, Biophys J **86**, 3993 (2004).

[146] P. Clark and F. Evans, *Distance to nearest neighbor as a measure of spatial relationships in populations*, Ecology **35**, 445 (1954).

[147] N. Cole, C. Smith, N. Sciaky, M. Terasaki, M. Edidin, and J. Lippincott-Schwartz, *Diffusional mobility of Golgi proteins in membranes of living cells.*, Science **273**, 797 (1996).

[148] J. Ellenberg, E. Siggia, J. Moreira, C. Smith, J. Presley, H. Worman, and J. Lippincott-Schwartz, *Nuclear membrane dynamics and reassembly in living cells: targeting of an inner nuclear membrane protein in interphase and mitosis.*, J Cell Biol **138**, 1193 (1997).

[149] K. Krauss and P. Altevogt, *Integrin leukocyte function-associated antigen-1-mediated cell binding can be activated by clustering of membrane rafts.*, J Biol Chem **274**, 36921 (1999).

[150] A. Kusumi, I. Koyama-Honda, and K. Suzuki, *Molecular dynamics and interactions for creation of stimulation-induced stabilized rafts from small*

unstable steady-state rafts., Traffic **5**, 213 (2004).

[151] E. J. Brown, *Integrin-associated proteins.*, Curr Opin Cell Biol **14**, 603 (2002).

[152] N. van Hulst, M. Garcia-Parajo, M. Moers, J. Veerman, and A. Ruiter, *Near-field fluorescence imaging of genetic material: toward the molecular limit.*, J Struct Biol **119**, 222 (1997).

[153] F. Braet, C. Rotsch, E. Wisse, and M. Radmacher, *Comparison of fixed and living liver endothelial cells by atomic force microscopy*, Appl. Phys. A-materials Science & Processing **66**, S575 (1998).

[154] H. G. Frey, S. Witt, K. Felderer, and R. Guckenberger, *High-resolution imaging of single fluorescent molecules with the optical near-field of a metal tip*, Phys. Rev. Lett. **93**, (2004).

[155] T. Klar, S. Jakobs, M. Dyba, A. Egner, and S. Hell, *Fluorescence microscopy with diffraction resolution barrier broken by stimulated emission.*, Proc Natl Acad Sci U S A **97**, 8206 (2000).

[156] M. Hofmann, C. Eggeling, S. Jakobs, and S. W. Hell, *Breaking the diffraction barrier in fluorescence microscopy at low light intensities by using reversibly photoswitchable proteins.*, Proc Natl Acad Sci U S A **102**, 17565 (2005).

Summary

The cell plasma membrane of eukaryotic cells is a lipid bi-layer that separates the cell cytosol from the extracellular environment. The composition and organization of proteins and lipids within this bi-layer have a direct impact on many cellular processes, since they form the senses of the cell. Technological advances, like high resolution microscopy together with the possibility to address different membrane components via specific labeling now allows researchers to investigate cell membrane organization in detail.

It is well recognized that clustering of cell surface receptors into microdomains fulfills an important role in regulating cellular functions. Unfortunately, the domains are often too small to be resolved with conventional optical microscopy. Near-field scanning optical microscopy (NSOM) is a relatively new technique that combines ultra high optical resolution, down to 70 nm, with single molecule detection sensitivity. As such, the technique holds great potential for direct visualization of domains at the cell surface. Yet, NSOM operation under liquid condition is far from trivial. In Chapter 2 of this thesis we have shown that the performance of NSOM can be extended to measurements in liquid environments. We have presented a reliable and easy-to-use system, with a perfect analogy to a diving bell, to perform tuning fork-based near-field scanning optical microscopy on soft cells in liquid. The principle of the diving bell system is to allow vibration of the tuning fork in air, while the NSOM probe is immersed in solution. In this way Q factors of 200 and higher in liquid are routinely obtained. The force feedback is reliable and stable over hours requiring minimum adjustment of the set-point during imaging. With this system, tip-sample interaction forces are kept below 350 pN enabling imaging of soft cells in buffer solution. For the first time, individual fluorescent molecules on the membrane of cells in solution were imaged with a spatial resolution of 100 nm. As such, liquid-NSOM is capable to reveal cell membrane organization in detail, while working in conditions that allow live cell imaging.

In Chapter 3 we have used the liquid-NSOM to investigate the existence and composition of a highly debated type of membrane domain, the so called lipid rafts. These lipid rafts (domains within the membrane enriched in cholesterol and glycosphingolipids) are believed to play a key role in many membrane related processes like immune cell signaling and viral entry. Their existence is rather controversial, since evidence for the presence of lipid rafts in native cell membranes can only be obtained via indirect methods. In Chapter 3 we demonstrated the ability of NSOM to directly visualize lipid rafts, enriched in glycosphyngomyelin (GM1),

via fluorescently labeled cholera toxin (CTxB) both in immature dendritic cells (imDC) and human monocytes (THP1) under liquid conditions. Remarkably, on both cell types GM1 nano-domains appeared to be smaller than 100 nm in size. Furthermore, exploiting single molecule detection we quantified the GM1 content of each individual domain. On both cell types, most domains only bind 1 to 6 CTxB molecules, while on THP1 cells, up to 25 CTxB molecules per domain were identified. These results are consistent with the most recent picture of functional raft pre-cursors as nanoscale entities containing only a few molecules.

This small size of the domains in combination with a high packing density adds an extra challenge to the analysis of domain content. In fact, at high packing densities, two or more particles that have no association can coincide within the same excitation volume resulting in brighter fluorescent spots and apparent clustering. The higher the density and the lower the imaging resolution, the more apparent clustering will result. Although NSOM provides superior spatial resolution, individual fluorophores within a nanometer-sized domain cannot be directly resolved. As a consequence, domain content still needs to be quantified based on fluorescence intensity. In Chapter 4 we demonstrated that experimentally obtained fluorescence images can be compared to simulated images of randomly distributed particles at densities related to experimental conditions in order to assess the degree of true clustering. We have used these simulations to investigate the degree of true clustering of the lipid raft marker GM1 labeled with CTxB on the membrane of THP1 cells in solution. The combination of high resolution optical microscopy and computer simulations has allowed us to unequivocally demonstrate nano-scale clustering of GM1, providing evidence that nanometer sized lipid domains (lipid raft pre-cursors) indeed exist in the cell plasma membrane.

We have also applied NSOM on cells in liquid to map the organization of different protein receptors on two different cell types with a spatial resolution better than 100 nm. The experiments described in Chapter 5 were combined with simulations using experimentally obtained parameters, i.e. receptor density and fluorescence intensity, to assess the degree of clustering. From two non raft markers investigated, the transferrin receptor CD71 appears randomly organized on THP1 cells, while CD46 forms nano-domains on imDC. Remarkably, we also found that the GPI anchored protein CD55, a commonly used raft marker, does not cluster on both imDC and THP1 cells, but rather organizes in a random fashion. These results demonstrate that classification as 'lipid raft associated' does not give a priori information on surface arrangement, i.e. lipid raft partitioning does not necessarily implies clustering and clustering is not *per se* maintained by lipid rafts. Furthermore we have mapped the organization of the C-type lectin

DC-SIGN on imDC and the integrin LFA-1 on THP1 cells. Our results on cells in liquid confirm clustering of these proteins at the nanometer scale, consistent with previous TEM experiments on dried cells. Our findings favor a model where not lipid raft partitioning but other mechanisms like protein-protein interactions or the cytoskeleton determine the distribution of proteins as either monomers or small clusters.

Many cellular functions depend on associations between proteins and/or lipids in the cell membrane. In Chapter 6 we therefore used the high resolution of NSOM to simultaneously investigate the nanometer scale spatial organization of different proteins and lipids on imDC and THP1 cell in solution. The extent of co-localization has been quantified using Pearsson's correlation coefficient and the results have been compared to confocal co-patching experiments. Significant association of different proteins (DC-SIGN and CD55 on imDC; and LFA-1 and CD71 on THP1) to the lipid raft marker GM1 has been observed using confocal co-patching. Strikingly, this spatial correlation has not been observed upon direct NSOM investigation, i.e., on fixed cells in solution with no co-patching. The potential nano-scale spatial proximity of these proteins to the raft marker GM1 has been also investigated using interparticle nearest neighbor distance (nnd) analysis. The resultant nnd distribution for CD71-GM1 is completely random consistent with the fact that CD71 is a non-raft associated protein. On the contrary, the nnd distributions of CD55-GM1 and LFA1-GM1 are significantly shifted to shorter distances as to compared to random organization. These results indicate a statistically relevant preference for LFA-1 and CD55 to be in close proximity to lipid rafts. Altogether, our findings favor a model in which both proteins and lipids are pre-organized into small separate nanoscale domains, where these nanodomains might function as cell membrane organizers that facilitate and accelerate the formation of larger functional domains.

This thesis described the implementation of a diving bell concept to allow high resolution NSOM imaging in liquid conditions. Using this technique it was for the first time possible to visualize nanometer sized lipid and protein domains on both immature dendritic cells and THP1 cells in liquid. In chapter 7 the future of NSOM imaging will is discussed as well as the implications of our results for the current picture of cell membrane organization.

Samenvatting

Het celmembraan van eukaryotische cellen bestaat uit een dubbele lipidelaag, die het interne milieu van de cel afschermt van de omgeving. De samenstelling en organisatie van eiwitten en lipiden in het celmembraan heeft een directe invloed op een groot aantal cellulaire processen. Technologische innovaties, zoals de ontwikkeling van hoge resolutie microscopie in combinatie met de mogelijkheid om lipiden en eiwitten fluorescerend te markeren, maken het nu mogelijk om de organisatie van het celmembraan tot in detail te onderzoeken.

Op dit moment is het algemeen geaccepteerd dat het clusteren van receptoren in microdomeinen een belangrijke rol speelt in de regulatie van cellulaire processen. Helaas zijn de domeinen over het algemeen te klein om zichtbaar te zijn onder een standaard lichtmicroscoop. Er is gelukkig een relatief nieuwe techniek, de zogenaamde nabije veld scannende optische microscoop (NSOM), die het mogelijk maakt om met zichtbaar licht een optische resolutie van 70 nm te behalen. Bovendien is een dergelijke microscoop gevoelig genoeg om de fluorescentie van individuele moleculen te detecteren. Deze eigenschappen maken de NSOM in principe zeer geschikt om domeinen op celmembranen te onderzoeken. Het is tot nu toe echter zeer moeilijk gebleken om de microscoop in vloeistof te laten werken. Wij laten in Hoofdstuk 2 zien dat de NSOM wel degelijk in vloeistof gebruikt kan worden. Om dit te bereiken gebruiken we een betrouwbaar en eenvoudig systeem, in feite gelijk aan een kleine duikklok, waarmee NSOM metingen gedaan kunnen worden op zachte cellen in vloeistof. Het idee achter de duikklok is dat de stemvork, die nodig is om de NSOM tip dicht bij het cel oppervlak in de buurt te houden, in lucht blijft trillen. De NSOM tip zelf is wel ondergedompeld in vloeistof. Dit maakt het mogelijk om de gevoeligheid van de stemvork te behouden, waarbij kwaliteits-factoren van 200 en hoger in vloeistof eenvoudig zijn te verkrijgen. Hierdoor zijn de krachtinteracties tussen de NSOM tip en de cel zwak en is het mogelijk om op het zachte oppervlak van cellen in buffer oplossing te meten. Het is voor het eerst dat individuele fluorescerende moleculen op een celmembraan in vloeistof zichtbaar gemaakt worden met een resolutie die beter is dan 100 nm. Dit werk laat daarom zien dat de vloeistof-NSOM geschikt is om gedetailleerde informatie over membraan organisatie te krijgen, terwijl de omstandigheden waarin gewerkt wordt geschikt zijn om aan levende cellen te meten.

In Hoofdstuk 3 gebruiken we de NSOM om de aanwezigheid en samenstelling te onderzoeken van een controversieel membraan domein, de zogenaamde ‘lipid rafts’, vaak voorgesteld als eilanden van vet. Deze ‘lipid rafts’ bevatten veel

cholesterol en glycosphingolipiden. Men denkt dat 'rafts' een belangrijke rol spelen in veel membraan gerelateerde processen, zoals signalering in ons immuunsysteem en het binnen dringen van virussen. Het bestaan van deze 'lipid rafts' is behoorlijk controversieel, omdat het bewijs voor hun bestaan in echte cel membranen alleen via indirecte methoden kan worden verkregen. Hier laten we zien dat de NSOM zeer geschikt is om 'lipid rafts' direct zichtbaar te maken. Dit wordt gedaan door de raft lipide glycosphingomyelin (GM1) fluorescerend te kleuren met behulp van cholera toxine (CTxB). We bekijken de verdeling van GM1 in zowel immature dendritische cellen (imDC) als in monocyten (THP1) in vloeistof condities. De meeste door ons gevonden GM1 domeinen zijn kleiner dan 100 nm. Door gebruik te maken van de gevoeligheid van de microscoop kunnen we het aantal GM1 moleculen in een domein direct bepalen. Op beide celtypen binden de meeste domeinen slechts aan 1 tot 6 CTxB moleculen, maar op THP1 cellen zijn domeinen waargenomen die tot 25 CTxB moleculen binden. Deze resultaten bevestigen het vermoeden dat er in het celmembraan veteilanden zijn die zeer klein zijn en maar enkele moleculen bevatten. Mogelijk zijn dit de voorlopers van functionele rafts.

De geringe domein grootte in combinatie met de hoge domein dichtheid maakt de analyse van de domein samenstelling extra gecompliceerd. Het is namelijk zo dat bij hoge dichtheden, twee of meer deeltjes, die eigenlijk geen relatie met elkaar hebben toch samen in hetzelfde excitatie volume kunnen voorkomen. De meer intense fluorescentie spots die hierdoor zichtbaar zijn wekken de indruk van cluster vorming. Hoe hoger de dichtheid en lager de resolutie, des te sterker is het effect van deze schijnbare clustering. Hoewel de resolutie van NSOM veel beter is dan de resolutie van conventionele lichtmicroscopen is het nog steeds niet mogelijk om individuele fluoroforen binnen een domein te onderscheiden. Hierdoor is de enige manier om de samenstelling van een domein te kwantificeren gebaseerd op het bepalen van de fluorescentie intensiteit van een domein. In Hoofdstuk 4 laten we zien dat gemeten fluorescentie plaatjes vergeleken kunnen worden met gesimuleerde plaatjes waarin de deeltjes willekeurig verdeeld zijn met een dichtheid die overeenkomt met de experimentele situatie. Door deze vergelijking is het mogelijk om de werkelijke mate van clustering uit de intensiteits plaatjes te bepalen. We hebben deze simulaties gebruikt om de werkelijke mate van clustering te bepalen van de raft lipide GM1, gemarkeerd met CTxB op THP1 cellen. De combinatie van hoge resolutie microscopie en simulaties heeft het mogelijk gemaakt om onomstotelijk vast te stellen dat GM1 clustert in domeinen met nanometer dimensie. Deze resultaten zijn het bewijs dat nanometer schaal domeinen (lipid raft voorlopers) werkelijk bestaan in een cel membraan.

De NSOM is ook gebruikt om de organisatie van verschillende receptoren

op cellen in vloeistof te bestuderen met een resolutie beter dan 100 nm. De experimenten die in Hoofdstuk 5 beschreven worden zijn direct vergeleken met simulaties waarbij gebruikt gemaakt is van experimenteel vastgestelde parameters zoals receptor dichtheid en fluorescentie intensiteit. Op deze manier is het mogelijk de werkelijke mate van clustering te bepalen. Voor de transferrine receptor CD71 en CD46 (beide eiwitten komen niet voor in raft domeinen) vinden we dat CD71 op THP1 willekeurig is georganiseerd, terwijl CD46 op imDC in domeinen voorkomt. Tot onze verbazing komt het GPI-anker CD55 (een eiwit dat geassocieerd is met rafts) juist niet voor in domeinen maar is willekeurig verdeeld over het membraan oppervlak zowel op THP1 als imDC. Deze resultaten laten duidelijk zien dat het kenmerken van een eiwit als geassocieerd met 'lipid raft', niet op voorhand informatie geeft over de verdeling in het celmembraan. Kortom, associatie met een raft domein betekent niet dat een eiwit clustert en clustering wordt niet perse gereguleerd door 'lipid rafts'. We hebben vervolgens ook gekeken naar de organisatie van de C-type lectine DC-SIGN op imDC en de integrine LFA-1 op THP1 cellen. Onze NSOM metingen op cellen in vloeistof bevestigen dat deze eiwitten clusteren in domeinen met nanometer dimensies, iets dat al eerder gezien is in TEM experimenten op droge cellen. Deze bevindingen zijn in overeenstemming met een model waarin de verdeling van eiwitten als monomeren of kleine clusters vooral wordt beïnvloed door eiwit-eiwit interacties of interactie met het cytoskelet en niet door associatie met 'lipid rafts'.

Veel celfuncties hangen af van de associatie tussen eiwitten en/of lipiden. In Hoofdstuk 6 onderzoeken we eiwit-lipide associaties door met de hoge resolutie van NSOM de ruimtelijke verdeling van zowel lipiden als eiwitten in het celmembraan te bekijken op imDC en THP1 cellen in vloeistof. De mate van co-lokalisatie is gekwantificeerd met behulp van Pearssons's correlatie coëfficiënt en de resultaten van de NSOM experimenten worden vergeleken met resultaten van confocale 'co-patch' experimenten. Er is een significante mate van associatie tussen verschillende eiwitten (DC-SIGN and CD55 op imDC; LFA-1 en CD71 op THP1) en de raft lipide GM1 als we gebruik maken van co-patching met confocale microscopie. Verrassend genoeg verdwijnt deze correlatie op het moment dat we de cellen in vloeistof onderzoeken met de NSOM zonder gebruik te maken van co-patching. De mogelijkheid dat er in plaats van directe associatie sprake is van voorkeur voor deze eiwitten om in de nabijheid van GM1 domeinen te organiseren is onderzocht met behulp van 'nearest neighbor distance (nnd)' analyse. De nnd distributie voor CD71:GM1 is volledig willekeurig en in overeenstemming met het feit dat CD71 een eiwit is dat niet met rafts wordt geassocieerd. Echter, de nnd verdelingen voor CD55:GM1 en LFA-1:GM1 zijn significant opgeschoven richting kortere afstanden in vergelijking met willekeurige organisatie. Deze resultaten

duiden erop dat LFA-1 en CD55 dichter in de buurt zitten van GM1 dan op basis van een willekeurige verdeling verwacht mag worden. Bekijken we alle resultaten tesamen dan is een model waarbij de eiwitten en lipiden georganiseerd zijn in kleine aparte nanoschaal domeinen het best toepasbaar. Deze nanodomeinen zijn mogelijk het eerste organisatie niveau in het celmembraan, die vervolgens de vorming van grotere functionele domeinen faciliteren en versnellen .

Dit proefschrift beschrijft de implementatie van een duikklok concept dat het mogelijk maakt om hoge resolutie NSOM metingen te gebruiken in vloeistof omstandigheden. Door deze techniek te gebruiken was het voor het eerst mogelijk om lipide en eiwit domeinen zichtbaar te maken op zowel imDC als THP1 in vloeistof. Tot slot bespreken we in Hoofdstuk 7 de toekomst van NSOM evenals de gevolgen die onze resultaten hebben voor het bestaande model dat de organisatie van het cel membraan beschrijft.

Dankwoord

Met het schrijven van dit dankwoord lijkt er dan echt een einde te komen aan mijn verblijf van nu al ruim 10 jaar aan de UT. Meer dan de helft van deze jaren heb ik besteed aan zowel afstudeerwerk als promotieonderzoek in de groep Optische Technieken met Niek van Hulst als hoogleraar en Maria García-Parajó als mijn dagelijkse begeleider. Beide ben ik dank verschuldigd, Niek voor zijn kritische blik vanaf de zijlijn en Maria voor de vele opbeurende gesprekken als het weer eens niet wilde lukken met het NSOMmen. Jullie hebben me alle kansen gegeven om me als wetenschapper te ontwikkelen. Al snel mocht ik mijn eerste praatje geven op een internationale conferentie en ook de eerste publicatie met mijzelf als 'corresponding author' volgde in rap tempo. Toen jullie eind 2004 aankondigden om de UT te verlaten en naar Barcelona te vertrekken was het voor mij wel even slikken, maar uiteindelijk is alles toch op z'n pootjes terecht gekomen. Ik wens jullie allebei veel succes met het opzetten van jullie nieuwe laboratoria op het ICFO en het PCB.

Het leuke van mijn promotie onderzoek heb ik altijd de combinatie van biologie en natuurkunde gevonden. Ik stel het dan ook erg op prijs dat Carl Figdor, hoogleraar tumorimmunologie, een van mijn promotoren is. Carl, het is bijzonder inspirerend om met jou te discussiëren want je bruist altijd van de ideeën! Om succesvol te kunnen samenwerken is enige afstemming nodig en ik denk dat we hier bijzonder goed in geslaagd zijn. Alessandra en Ben, jullie waren geweldig. Vele ideeën, metingen, samples, telefoontjes, emails, powerpoints en originfiles zijn uitgewisseld, kortom alle ingrediënten voor een zeer vruchtbare samenwerking. Daarbij wist ik altijd de juiste tijdstippen (taart) te vinden om langs te komen in Nijmegen om ook gezellig bij te kletsen. Andere (ex)TILers die ik wil bedanken zijn lange Frank (te lang voor de NSOM), Frank, Suzanne, Chris (unfortunately we never got results for the TRPM7 with NSOM) en Karlijn (de sample express).

In Enschede zijn er ook veel mensen die direct of indirect een steentje hebben bijgedragen aan de inhoud van dit boekwerk. Om te beginnen natuurlijk Erik. Ik heb vanaf mijn afstuderen tot aan je eigen promotie begin 2005 met je samengewerkt. Heerlijk je kritische vragen tijdens de werkbespreking, discussies over alles en nog wat en je enorme hulp bij de analyse van een groot deel van mijn data door je supersnelle (en ondoorgrondelijke) programmeerwerk in LabView. Ik hoop dat je als paranimf net zo'n steun bent als je tijdens een groot deel van mijn promotie bent geweest. Jeroen, ook jij hebt vooral op het laatst veel geholpen met lastminute programmeerwerk vanuit het Spaanse, waardoor ik de resultaten

in Hoofdstuk 4 in korte tijd heb kunnen opschrijven. Frans, bedankt voor alle FIB sessies, want zonder FIB geen NSOM tip. Verder wil ik ook Bärbel bedanken voor de bouw van een groot deel van de bioNSOM. Ik hoop dat het je goed doet dat het apparaat dat je hebt gebouwd zoveel gebruikt is. Dan zijn er natuurlijk nog veel meer mensen die ik nog wil noemen zoals, Nancy (we hebben toch een paar activiteiten weten te organiseren), Jacob (hoe zullen we onze loopbaan plannen), Robert (wat zeg je daar nu weer, moet ik al reageren.. en natuurlijk paranimf), Gert-Jan (veel succes met je Barcelona avontuur, die levende cellen komen nog wel), Klaas (de duikklok werkt echt), Hans (BAK troubleshooter), Kobus (elke slide heeft een boodschap), Herman (tja de eerste kennismaking blijft NFO7), Gabriel (Barcelona tour guide), Jordi (writing of a test thesis) en natuurlijk alle ander mensen die bij Optische Technieken de sfeer hebben bepaald.

Natuurlijk blijft er naast het promoveren nog genoeg tijd over voor andere leuke dingen. Vooral de eerste paar jaar van mijn promotie heb ik me meestal op donderdagavonden erg vermaakt bij DRV Hippocampus. Ik blijf toch van mening dat paardrijden echt een sport is. Alle Hippoers bij deze bedankt voor de vele gezellige avonden. NIMFen bedankt voor de vele gesprekken, ik hoop dat we nog vaak bij elkaar kunnen komen om van elkaar te leren.

Dan blijven de laatste paar regels in een dankwoord meestal over voor familie en vrienden. Jullie directe aandeel in mijn promotie is beperkt en dat vind ik eigenlijk wel prima. Zo blijven er tenminste genoeg andere dingen over om over te praten. Iedereen bedankt voor de sauna bezoekjes, de etentjes, het skiën, motorrijden en zeilen. Laten we hier vooral mee doorgaan.

Marc de laatste regel is dan toch echt voor jou. Bedankt voor je rotsvaste vertrouwen in mijn kunnen. We gaan ervoor!

Marjolein Mutsaers-Koopman
Deventer, maart 2006

Publications

Publications related to the work described in this thesis:

- M. Koopman, B.I. de Bakker, M.F. Garcia-Parajo, and N.F. van Hulst, *Shear force imaging of soft samples in liquid using a diving bell concept*, Appl. Phys. Lett. **83**, 5083-5085 (2003)
- M. Koopman, A. Cambi, B.I. de Bakker, B. Joosten, C.G. Figdor, N.F. van Hulst, M.F. Garcia-Parajo, *Near-field scanning optical microscopy in liquid for high resolution single molecule detection on dendritic cells*, FEBS Lett. **573**, 6-10 (2004)
- M. Koopman, A. Cambi, B. Joosten, C.G. Figdor, N.F. van Hulst, M.F. Garcia-Parajo, *Lipid rafts unraveled using near-field scanning optical microscopy*, In preparation (Chapter 3 en 6)
- M. Koopman, A. Cambi, B. Joosten, J.P. Korterik, C.G. Figdor, N.F. van Hulst, M.F. Garcia-Parajo, *Clustering vs. random distribution: experiment and simulations*, In preparation (Chapter 4)
- M. Koopman, A. Cambi, B. Joosten, C.G. Figdor, N.F. van Hulst, M.F. Garcia-Parajo, *Nanoscale compartmentalization of the cell membrane*, In preparation (Chapter 5)
- M.F. Garcia-Parajo, B.I. de Bakker, M. Koopman, A. Cambi, F. de Lange, C.G. Figdor and N.F. van Hulst, *Near-field fluorescence microscopy an optical nanotool to study protein organization at the cell membrane*, NanoBiotechnology, **1**, 1551-1286 (2005)

Other publications:

- A. Cambi, B. Joosten, M. Koopman, F. de Lange, R. Torensma, J.A. Fransen, M.F. Garcia-Parajo, F.N. van Leeuwen and C.G. Figdor, *Organization of the integrin LFA-1 in nanoclusters regulates its activity*, Submitted to Mol. Bio. Cell.
- A. Cambi, M. Koopman, C.G. Figdor, *How C-type lectins detect pathogens*, Cell Microbiol. **7**, 481-488 (2005)

- G. Sanchez-Mosteiro, M. Koopman, E.M.H.P. van Dijk, J. Hernando, N.F. van Hulst and M.F. Garcia-Parajo, *Photon antibunching proves emission from a single subunit in the autofluorescent protein DsRed*, ChemPhysChem **5**, 1782-1785 (2004)
- M.F. Garcia-Parajo, M. Koopman, E.M.H.P. van Dijk, V. Subramaniam and N.F. van Hulst, *The nature of fluorescence emission in the red fluorescent protein DsRed, revealed by single-molecule detection* Proc. Natl. Acad. Sci. U S A **98**, 14392-14397 (2001)